REVIEW

Post-Process Treatments for Additive-Manufactured Metallic Structures: A Comprehensive Review

Jun Ge ⓘ, Selvum Pillay, and Haibin Ning

This review summarizes the recent research progress on the post-processing techniques to improve the as-built metallic structure fabricated by additive manufacturing. The comprehensive comparison reveals that hot isostatic pressing (HIP) is the only one of few that can eliminate the internal porosity ($< 0.01\%$) with high efficiency and availability. Traditional heat treatments (HTs) are still the best approach to improve or alter the microstructure for the overall bulk properties. Various surface post-processes are presented that are more flexible and cost-effective than common machining and polishing. Laser-based techniques are the most popular treatment for surface modification to induce compressive stress, remove the surface pores, reduce the surface roughness, or apply coatings for functionality. Other mechanical methods like shot peening (SP), laser shock peening (LSP), ultrasonic nanocrystal surface modification (UNSM), and abrasive-based treatments facilitate plastic deformation to impact surface beneficially for hardness, fatigue, or corrosion resistance. In addition, impact-type surface treatments (SP, LSP, and UNSM) are more effective on enhancing the mechanical properties due to greater energy imparted to the surface than abrasive-type treatments. Electrochemical polishing is capable to achieve the best surface smoothness ($R_a < 0.1$ μm), while friction stir processing shows the best effectiveness on homogenize the structure without significant grain growth at nanoscale. Advanced but costly surface techniques are only suitable to satisfy specific requirement and application of high value metallic component. By optimizing the process parameters and adopting in situ tools, the as-built structure can be enhanced with minimized necessity for post-processing. Overall, a complete solution of post-treatment includes HIP, HTs, surface modification, and/or special process.
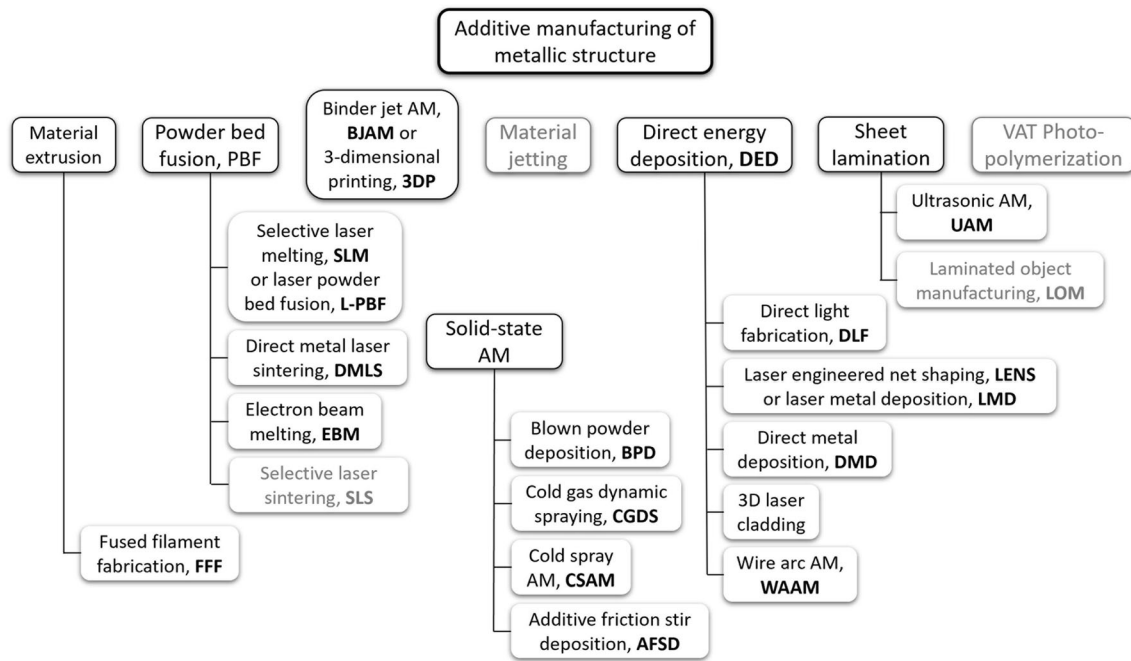
1. Introduction

Additive manufacturing (AM), as a disruptive technology, provides one revolutionary approach to build metal component that allows for precise control of the as-built structure in a layer-wise manner. The properties and performance of the as-build part depend on every solidified layer formed through ultra-fast and intensified (up to $\sim 10^5$ K/s) cyclic heat/cool process (Ref 1, 2). By manipulating the grain size, grain morphology, phase composition, crystal orientation as well as interlayer bonding, contrary to conventional processes like casting and forging, AM-built metallic part can be created at the nanoscale according to the process-structure–property relationship. The overall equipment effectiveness (OEE), which in modern manufacturing requires to be greater than 70% with scrap rates of less than 1000 ppm, can be achieved by AM with appropriate process optimization.

1.1 AM Processes and Classification

The current AM techniques and concepts are commonly classified through several aspects. Figure 1 shows a schematic view of AM concepts and techniques according to ISO/ASTM 52,900 standard and literature (Ref 3). Based on material feeding, they can be categorized as powder bed systems, powder feed systems, wire feed systems, and sheet lamination systems. On the other hand, the metal-based materials can be melted by different energy sources like laser, electron beam, or electric arc plasma (Ref 4). In powder bed AM, the melting phenomenon is carried out by the combination of the particle arrangement and the capillary-driven liquid phase penetration, in which the surface energies of the liquid and solid alloys and liquid–solid interfacial energies play important roles. Electron beam melting (EBM), selective laser melting (SLM), and binder jetting AM (BJAM) are all derivatives of powder bed fusion (PBF) concept (Ref 5). Laser-based printing can also be divided into three printing modes of laser sintering (LS), laser melting (LM), and laser cladding (Ref 6). Due to incomplete melted particle and inhomogeneous heating, sintered metal part requires subsequent post-sintering, infiltration, or heat treating to remove binder and achieve full dense. Parts built by LM require a high-power laser source and exhibit high internal stresses due to the high temperature gradient and dramatic thermal history. For instance, SLM, which is also called L-PBF or direct metal laser sintering (DMLS), melts the metal particles completely in the manner of partially remelting or resolidifying the previous solidified layer with rapid directional diffusion of energy through laser spot. High internal residual stresses,

Jun Ge, Selvum Pillay, and **Haibin Ning**, Department of Materials Science and Engineering, University of Alabama at Birmingham, Birmingham, AL 35294. Contact e-mail: ning@uab.edu.

Fig. 1 Major concepts and techniques for metallic additive manufacturing categorized based on ISO/ASTM 52,900

anisotropy in microstructure, and porosity always present with varying degree, distribution and morphology in the as-built structure (Ref 7). Annealing is generally applied to SLM parts to decrease the chemical segregation, alter the distribution of secondary phases, and reduce residual stresses. BJAM, also known as three-dimensional printing (3DP), uses an inkjet printing head to spray liquid binder into a layer of powder. After blending of the particulates or multi-species of oxide precursor for complex alloy like high entropy alloy (HEA) or medium entropy alloy (MEA) with binder and solvent, BJAM requires powder removal, curing, debinding, and sintering steps to achieve burnout of the binder and densification of the article (Ref 8-10). Similar to LS, post-sintering and infiltration are necessary to be adopted to eliminate pores, reduce residual stress and segregation, improve surface roughness, increase the ductility, and modify the chemical composition of the final part (Ref 11-13). EBM generally produces metal part with greater surface roughness than that of the laser-based techniques due to the limitations of thicker powder layers, coarser particles, and the faster scan speeds. Since it is conducted in vacuum and easy to reach high processing temperature, EBM can process alloys with high melting point or high affinity to oxygen and nitrogen with minimum degree of stress-relief treatment (Ref 14). Directed energy deposition (DED) includes laser engineered net shaping (LENS®), directed light fabrication (DLF), direct metal deposition, and 3D laser cladding. LENS, also known as laser metal deposition (LMD), is one of the derivatives of laser cladding technologies. It feeds single grade or multiple species of particles into the path of a laser beam at the focal point to create a molten pool on the substrate material, allowing the build to achieve a full or gradient composite. Alternatively, laser cladding can be used directly for surface treatment. For instance, laser surface modification (LSM) adopts LENS to modify granular structure of Ti6Al4V alloy thereby changing the hardness while creating a passive oxide layer that significantly enhances the wear resistance. Typical examples for

powder feed and wire feed technique are cold spray (CSAM) or blown powder deposition (BPD), and wire arc additive manufacturing (WAAM), respectively (Ref 15-17). WAAM, as a DED technique, uses an electric arc and a solid wire to build metallic part with a lower precision but a significant higher deposition rate than those in other systems. With controlled operating process and plasma flow, microplasma WAAM enables production of thin parts with total wall width (TWW) around millimeter scale. The wire feeding and droplet transfer are realized through the detection of the contact between the electrode wire tip and molten pool, as well as the activation of the servomotor to retract the wire (Ref 15). Post-WAAM heat treatments can be used by means of hot isostatic pressing (HIP), solution treatment, annealing, aging, and other thermal treatments (Ref 18). As solid-state AM, CSAM can be used to deposit temperature-sensitive and oxygen-sensitive materials to form functional and dissimilar components like metal matrix composites (MMCs), particle-reinforced MMCs, and HEAs since it operates with little heat effect on the spray materials. CSAM accelerates the particles through a pressurized and preheated propulsive gas that expands in the de Laval nozzle to reach a supersonic velocity. The printed CSAM part generally has a low level of ductility or plasticity since each deposited layer is formed under the severe plastic deformation of each single particle during impaction on the substrate material. Similarly, cold gas dynamic spraying (CGDS), a solid-state thermal spray process, can apply for direct deposition of metal-based materials and also used for coatings and repairs (Ref 19, 20). CGDS is not limited on the tray size and is able to print at a deposition rate that is an order of magnitude larger than the current fastest PBF AM technology. The disadvantage of CGDS is the significant level of porosity in the as-print sample, which requires a significant amount of post-processing. Sheet lamination processes typically bond thin sheets of metallic foils by brazing, diffusion bonding, laser welding, resistance welding, or ultrasonic seam welding. One

typical example is ultrasonic additive manufacturing (UAM) system. UAM does not fully melt the metal but works at a much lower temperature (0.3–0.5 of the melting point). This advantage allows UAM to minimize the defects that are associated with high temperature exposure in melting and solidification. UAM is capable of fabricating component with sophisticated geometries and joining dissimilar metals (Ref 21, 22). Additive friction stir deposition (AFSD) is another solid-state sheet lamination approach for fabrication of metals and MMCs using wire or powder feeding and it is capable of large-scale printing without vacuum chamber or powder bed (Ref 23, 24). The peak temperature in AFSD-built parts normally ranges from 60 to 90% of the melting point. As a result, the as-built structure exhibits little defects, such as porosity, hot cracking, chemical segregation, inclusion agglomeration, or high residual stresses. Therefore, similar to UAM, the AFSD-built part is at a minimum requirement for thermal post-treatment. The resultant microstructure is featured with refined and equiaxed grains as well as isotropic texture formed during dynamic recrystallization in the heat-affected zone (HAZ). The inhomogeneity caused by cyclic reheating in grain structure and composition at interlayer regions can be corrected partly through post-processing treatments. In addition, bulk metallic glasses (BGM) and HEA can be printed through 3D-ink extrusion or fused filament fabrication (FFF) like thermoplastics, which can also be heat-treated to improve the mechanical properties (Ref 13, 25).

Post-processing treatment adjusts the structure and enhances the properties of the as-built metallic part from the abovementioned techniques to meet various standards, for example, the minimum ultimate tensile strength requirements specified by the ASME code (Ref 26). It improves the final density, minimizes the porosity, eliminates the internal and surface defects like lack of fusion, improves the surface finish/geometrical tolerance, and reduces the anisotropy as well as residual stress in the printed structure (Ref 27). Different AM techniques exhibit unique characteristics and thus suit for different single or combination of post-processing treatments. In summary, post-treatments for AM metallic part are focused on improving properties, such as resistance to corrosion and fatigue, of the printed structures to enhance their sustainability and performance in structural and stress-bearing applications (Ref 28, 29).

1.2 Defects in AM-Produced Metal Part

Although AM techniques show certain advantages over conventional fabrication processes, such as casting and forging, the finished structures may suffer from undesired characteristics and defects, which lead to reduced properties and performance (Ref 30-32). Metal parts processed with PBF typically show lower fatigue resistance. For example, the fatigue performance of SLM Ti6Al4V alloy is 75% lower than wrought material due to defects (Ref 33). Common defects include porosity (gas entrapment and lack of fusion), high surface roughness (partially melted particle, balling, etc.), interlayer delamination, high residual stress, and compositional inhomogeneity (Ref 34). Part distortion and anisotropy characteristics (anisometric columnar grain morphology, strong crystallographic texture) are the other two major issues. Warping, cracking, or delamination of a component can result in part rejection. On the microstructure level, defects can also form as significant residual dislocations, solidification substructure, and element

segregation due to the high solidification rate as well as loss of element due to preferential vaporization (Ref 35). All the defects are significantly affected by the thermal history (i.e., melt pool temperature, thermal gradient, cooling rate, and cyclic reheating) in AM processes.

Gas pores may generate from various sources. First, it can come from the residual gas entrapped at the interparticle spacing during rapid solidification. Secondly, the gas phase formed through the reactions of oxidation and reduction in the melt also leads to pore formation. In addition, porosity can be caused by the evaporation of certain elements and volatile solid material. Moisture and coagulation of shrinkage are also related to porosity. Lack-of-fusion pores form when the melted metal powder solidifies before being able to completely fill existing gaps. The morphology, size and distribution of pores are also playing an important role. Gas porosities tend to be small (< 100 μm) and spherical, while the lack-of-fusion pores, also called void, tend to be much larger (> 100 μm), have irregular shape, and most importantly, are slit-shaped. Gas porosity reduces the modulus and thereby affecting the deflection behavior of the materials. In addition, the fatigue life of a material is also greatly impacted by the presence of porosity, including the size, shape, and the location of the void (Ref 36). Typically, AM materials exhibit substantial shorter fatigue life and lower high cycle fatigue (HCF) strength as compared with wrought materials. The fatigue fracture surfaces reveal that the failure mechanism of fatigue life is attributed to the close-to-surface void acting as a crack initiation site for stress concentration. These surface voids provide the required stress concentration to develop cracks at a lower number of fatigue cycles. Thus, the failure mechanism for AM materials is more affected by void location rather than its shape or size.

Surface roughness issue is attributed from a combination of build orientation, particle size distribution, removal of the support structures, the staircase effect, and the rippling effect from quick solidification of melt pool. It is also affected by the presence of unfused or partially fused raw materials contiguous to the layer contour profiles (Ref 37). Components for high end applications require an average surface roughness less than 1 μm. Surface roughness is the major cause of the crack initiation since the valleys in the surface profile act as stress concentration notches that induce fracture. It negatively affects fatigue resistance and wear behavior of the build part. Increase of the fatigue life can, therefore, be obtained by delaying crack initiation through improving the surface roughness.

The dimensional accuracy and conformity of the printing part are related to many factors. The cyclic heating/cooling and remelting of the previous layer when the current layer is deposited cause an uneven cyclic thermal load across a certain number of layers according to the level of the energy source. The heat from the cycles accumulates to form high thermal gradient within the deposited part. Along with the continuously varying slice contours, such anisotropy gives rise to residual stresses resulted from the degree of the thermal gradient, which therefore causes part shrinkage during the building process. Such highly textured material in the as-built status is dominated by columnar-grained macro-structure and exhibits anisotropy in both crystallographic microstructure and bulk mechanical properties.

Moreover, the intrinsic error of staircase features, which is caused by the layer-wise nature of part discretization into successive layers on the curved face perpendicular to the building direction, affects the surface finish and tolerance of the
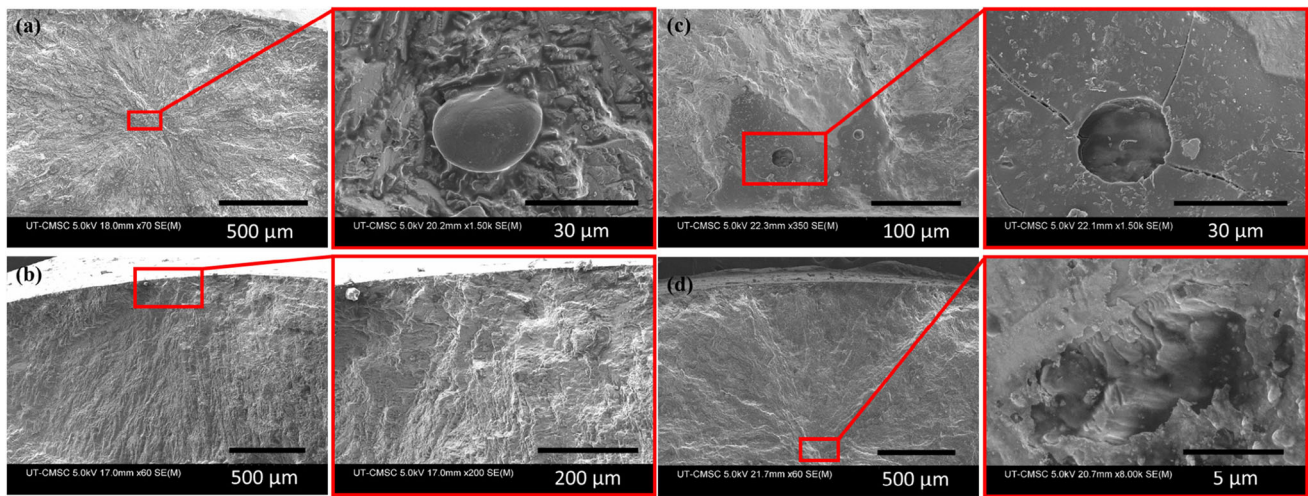
Fig. 2 SEM micrographs of crack initiation during fatigue failure of machined HIPed Ti-6Al-4 V specimen fabricated by SLM: (a) un-melted particle (axial loading), (b) surface defect (torsion loading), (c) porosity from entrapped gas (in-phase axial-torsion loading), (d) partially melted region (in-phase axial-torsion loading) (Ref 40). Reprinted from International Journal of Fatigue, Vol 117, Reza Molaei, Ali Fatemi, Nam Phan, Significance of hot isostatic pressing (HIP) on multiaxial deformation and fatigue behaviors of additive manufactured Ti-6Al-4 V including build orientation and surface roughness effects, Pages 352–370, Copyright 2018, with permission from Elsevier

fabricated component. Due to the thermomechanical nature, the staircase feature generated through the process control algorithm on the geometry of individual cross sections of layers, thin features, and sharp corners is non-removable by parameter optimization but can be minimized by post-processing operation (Ref 38).

During high-temperature exposure, part geometric distortion is inevitable and cannot be reversed by heat treatment. Part distortion, which is also called warping, is related to the residual stress caused by cyclic heating/cooling and a large temperature gradient between layers. Vibration of the metallic part during machining can also contribute to the part distortion. Residual stresses within the part can lead to anisotropy and decrease fracture toughness. Numerical modeling and physics-based analytical models have been applied to simulate and predict the distortion. The main mechanism behind the distortion can be described through thermo-elasticity, elastic–plastic, and displacement theories (Ref 39). Due to the significant difference in heat input and conduction between two successive layers, the thermal gradient induces different rate of expansion of the two layers as well as elastic/plastic compressive strains. In general, the longitudinal residual stress forms at the top of the printed article with a parabolic distribution and increases when more layers are deposited with decreasing thermal gradient. This transition of stress between compressive and tensile states at different locations of the article leads to warping. The magnitude of such residual stress is governed by material properties (thermal expansion, thermal diffusivity, and conductivity), phase transformation, geometry and position of components, processing parameters and function, etc. Part distortion can be minimized by preheating the substrate, insulating of the system, embedding the part inside the powder to enable a cool-down stage, and limiting the melt pool size. Shorter scanning path, larger layer thickness, and alternative scanning direction also reduce the stress.

Cracks are formed when insufficient liquid phase is presented during solidification, especially a rapid cooling process. The cracks can be divided into two groups as microcracks and macro-cracks based on the scale of their size.

Liquid-state cracking, or hot cracking occurs when too much stress is applied on the liquid film between two growing dendrites and the liquid from the melt pool is unable to backfill the inter-dendritic gap. Such crack can exclusively be found at the columnar grain boundaries. The crack also affects creep behavior of AM parts at elevated temperature. At elevated temperature, grain boundary cavitation and crack growth dominate the creep behavior. Even a low concentration of oxygen at elevated temperature, can accelerate the creep crack growth rate during post-heat treatments. All the cracking mechanisms are driven by the high residual stress and the microstructural development during the rapid solidification. The extreme low ductility of certain alloy is induced mainly by strain-age cracking (SAC), which is the result of stress accumulation by the precipitation or hard phase that prevents relaxation of the matrix either inside grain or near grain boundaries in regions of segregation. While intergranular cracks, which are also called ductility dip cracks (DDC), can be observed in alloy structure after thermal post-treatments. The formation mechanism of DDC is attributed to the dissolution and reprecipitation of certain alloy phase during cooling. SAC can be controlled by avoiding grain boundary sliding and microcracking. These low-temperature creep mechanisms raise the residual stress and can be minimized through post-treatments such as precipitation hardening, surface peening, etc. Post-surface treatment imparts a compressive residual stress on the surface and retards the initiation of cracking. Figure 2 demonstrates cracks and their initiation during fatigue test of Ti6Al4V specimens fabricated by SLM and treated through machining as well as HIP.

Beam-based AM techniques often encounter operational-related defects. Pores also originate from improper setting on the energy input of the AM process. The input energy per unit volume of material is determined by factors of beam power, scan speed, hatch spacing, and layer thickness. The melt pool is a balance of input energy and heat conduction around itself. This balance limits the amount of liquid phase developed and therefore controls the geometry of the melt pool. Thus, spherization effect, which is also called balling, occurs when

the molten pool forms in an instable spherical shape under certain irradiation force and the transverse velocity of the beam, resulting in poor surface quality, low density, and emergence of pores. When input energy is insufficient for the material, lack-of-fusion and poor consolidation of the powder occur in the as-print article. Excessive energy leads to overheating, spattering, and defect of keyholing. Generally, optimizing the overall energy input can control the total amount of porosity in the final print part. Excessive energy evaporates the material to form the vapor phase, which decreases heat transfer rate and thereby creating a much deeper melt pool than intended. The keyhole defect occurs when the vapor cavity collapses and develops a pore on the previously deposited layer due to the instabilities inherent to the system. Hatching or path defects occur when the algorithms used to plan the beam path for each layer leave gaps in the geometry.

In summary, post-process techniques have been adopted and studied to address the abovementioned issues for different materials under various conditions. Mechanical properties such as fracture toughness, ductility, fatigue strength of the metal AM parts can be effectively improved through post-treatment processes. A typical sequence for post-processing can be a stress relief first, followed by HIP, then solution heat treating and precipitation hardening, and finally support removal after necessary heat treat cycles and post-surface treating if part requires tighter tolerances or a superior surface finish. A recent review by Ye et al. showed results of preliminary comparison among those post-treatments (Ref 41). However, in-depth analysis with sufficiently coverage of different metallic materials, 3D printing techniques, and advanced post-processing is lacking. This paper tends to provide such comprehensive work and offer in-depth understanding of the effectiveness and drawbacks of different post-treatments on AM-built metallic structure.

1.3 Fundamental Theories of Metal Printing

For the PBF AM process, the energy input of laser or electron beam can be simply written in the form of beam power density (Ref 42, 43):

$$E = P/vs't, \qquad (Eq\ 1)$$

where v is the beam travel speed in cm/s, s' is the beam hatch spacing in cm, and t is the layer thickness in cm. Thus, the linear power density (in J/cm) is $E_l = P/v$. The combined effect of high solidification velocities and high thermal gradient presented in either the powder bed or melt pool leads to the formation of highly textured structure, which locates on the upper-right corner of the solidification map constructed by generalized temperature gradient (G) versus growth rate (R) plot. The solidified microstructure is governed by the ratio of $G \bullet R$ and G/R. The layer cooling rate then can be expressed as (Ref 44):

$$GR = A/e^{aE_l}, \qquad (Eq\ 2)$$

where a and A are material constants. In dendrite formation, the inter-dendritic spacing, λ, is related to the cooling rate by Kurz–Fisher relationship (Ref 45-47):

$$\lambda = a/GR^n, \qquad (Eq\ 3)$$

where a is a constant and n can vary from $\sim\frac{1}{4}$ to $\frac{1}{2}$, for secondary dendritic arm spacing, $\lambda = d_2$, $n = 3$. Therefore,

increasing $G \cdot R$ in general decreases the size and spacing of the residual microstructure. During layer building, the microstructure of the AM part changes from columnar to equiaxed grain structure as G/R decreases. In this process (Ref 44):

$$G/R = 2\pi k\left(\Delta T^2\right)/BPv, \qquad (Eq\ 4)$$

where k is the thermal conductivity of the layer, ΔT is the liquidus-solidus temperature difference, B is a constant, P and v are the beam energy and travel speed, respectively.

According to the "rule of thumb" of $H \sim 3\sigma_y$, Vickers hardness, H, of a metallic structure can be approximated with the tensile yield stress σ_y (Ref 48). With considering of the Hall–Petch relationship, σ_y can be written in the general form as follows:

$$\sigma_y = \sigma_0 + \frac{K'}{\sqrt{D}} + \frac{K''}{s} \qquad (Eq\ 5)$$

where σ_0 represents an intrinsic yield stress of a single crystal of the metal or alloy, K' and K'' are material constants, D is average grain size of the polycrystalline metal or alloy grain size, and s is the spacing or dimension of intragrain microstructures such as phase platelets, stacking faults, twins, etc. Therefore, hardness and tensile behavior can both be related to the microstructure of the material.

The inherent dislocations in an AM-built metallic structure can enhance mechanical properties (Ref 49). The improvement in yield strength can be correlated to strengthening mechanisms in microstructure of AM-built materials. Metals with an FCC structure normally are subjected to deformation form dislocation cell substructures that follow empirical relationship and it can be written as the equation below (Ref 50, 51):

$$\sqrt{\frac{\pi}{4}d^2} = \frac{10}{\sqrt{2}\rho_d}, \text{ or } d = \frac{10\sqrt{2}}{\sqrt{\pi\rho_d}}, \qquad (Eq\ 6)$$

where d is the dislocation cell diameter and ρ_d is the bulk dislocation density. Therefore, a classical strain hardening model to account for strengthening from both high-angle grain boundaries (HAGBs) and dislocation densities can be expressed with an additional term of dislocation Taylor hardening (Ref 52-54):

$$\sigma_y = \sigma_0 + \frac{K'}{\sqrt{D}} + \frac{K''}{s} + \alpha MGb\sqrt{\rho_d}, \qquad (Eq\ 7)$$

where α is a proportionality factor measuring the efficiency of dislocation strengthening, which ranges from 0.2 to 0.8, M is the Taylor factor that can be assessed from EBSD analysis, G is the shear modulus, and b is the Burgers vector.

In summary, Eq 1, 2, 3 and 4 describe a simplified approach to evaluate the relationship between process parameters and the potential structure of the metallic part, while Eq 5, 6 and 7 establish the link between them and the resulting strength considering the intrinsic dislocation and provide a quick estimation of yield strength of the printed specimen.

2. Thermal Post-Processing

Thermal post-processing includes hot isostatic pressing (HIP), sintering/infiltration, traditional heat treatment methods (annealing, normalizing, tempering), etc. Thermal post-processing is applied to metallic parts fabricated by AM processes

Table 1 The effects of thermal post-processing on mechanical properties of metallic structure

Process	Porosity, %	Modulus	Tensile strength	Ductility	Hardness	Fatigue resistance	Corrosion resistance
HIP (Ref 55–63)	< 0.01	Higher	Lower	Higher	Dependent	Higher	Dependent
Annealing (Ref 55, 57, 60, 64–77)	< 0.1	Lower	Lower	Higher	Lower	Higher	Higher
STA (Ref 62, 67, 78–85)	< 0.3	Higher	Higher	Dependent	Dependent	Higher	Dependent
Solutionizing (Ref 74, 79, 80, 86])	< 0.3	Lower	Lower	Higher	Lower	Higher	Dependent
Aging (Ref 58, 79, 80, 87, 88)	< 1.0	Higher	Higher	Lower	Dependent	Higher	Higher
HIP + STA (Ref 58, 83, 89–95)	< 0.01	Higher	Higher	Higher	Higher	Higher	Higher
Sintering (Ref 84, 96–99)	< 0.8	Higher	Higher	Higher	Higher	…	…
Infiltration (Ref 12, 98–100)	< 0.2	Higher	Higher	Higher	Higher	…	…

to enhance their properties, achieve the desired microstructures, relieve the residual stresses, and reduce chemical segregation and directionality from solidification, adjust pore morphologies and distributions in the material. It is noteworthy that recrystallization occurrence during post-thermal treatments at high temperature is critical to the final structure of the printed part. Recrystallization fully resets the microstructure and diminishes the Zener pinning effect from secondary dispersion phases due to the grain growth. Therefore, it eliminates the dislocation cell structures and has a negative effect on the mechanical properties. Specifically, annealing and aging can eliminate discontinuities at the interfaces, while HIP can enhance the elongation along the build direction by removing internal voids. The anisotropic characteristics of AM-fabricated materials can be eliminated by recrystallization or multiple variants of a dominant second phase. Table 1 summarizes a generic understanding of the effect of post-thermal treatment.

The effect of post-heat treatment and treatment cycles, which can alter both grain structure and intragrain microstructures, can be evaluated by the following equation (Ref 44):

$$D_{grow} - D_{initial} = At/\exp(Q_G/RT), \tag{Eq 8}$$

where $D_{initial}$ is the initial grain diameter, D_{grow} is the thermally processed grain diameter, A is a constant, Q_G is the activation energy for grain growth, R is the gas constant, T is the temperature, and t is holding time at the specific temperature.

The solutionizing time, t_s, in solution treatment can be expressed as (Ref 80, 101):

$$t_s = \frac{-\lambda^2 \ln k}{4\pi^2 D_0} \exp\left(\frac{Q_D}{RT}\right), \tag{Eq 9}$$

where D_0 is the diffusion constant, k is the material constant, and Q_D is the diffusion activation energy. Equation 8 and 9 estimate the evolution of grain size in the printed metallic structure during post-thermal treatment.

2.1 Hot Isostatic Pressing (HIP)

Hot isostatic pressing was developed around 1955 to further densify pre-consolidated powder after sintering. Figure 3 shows the schematic view of typical HIP equipment. The pre-sintered sample is placed in the chamber filled with inert gas

and heated up to 2000 °C with elevated pressure up to 30,000 psi. During the treatment, the specimen is collapsed mechanically under the isostatic pressure (Ref 102). HIP is widely used for consolidation of metal or ceramic powders and has also been shown to increase the density in metallic components by reduction or elimination of porosity. Due to the intrinsic porosity of as-built metallic structures, HIP is such a vital process for the AM-fabricated metallic part and attracts the most attention for priority of adoption in AM post-processing. This also separates itself from other traditional heat treatment techniques. Typical process parameters used in the literature to treat different AM metallic structures are listed in Table 2. Generally, the processing temperature in HIP is below the melting point and slightly higher than the solidus line according to ASTM F3301. The HIP temperature should be above the solvus temperature to achieve a porosity level under 0.01%. HIP does not have a significant impact on the grain structure and the columnar grain boundaries when the treatment temperature is around or below the solubility point.

HIP increases the strength, ductility, and plasticity of the AM metallic structure. It also decreases the chemical segregation, promotes the formation of equiaxed grains, eliminates anisotropy through recrystallization, and improves the homogeneity of the microstructure. Both super- and sub-transus HIP enable uniform response in fatigue and tensile tests of the treated specimen. Scattering in the performance of fatigue and tensile test is also reduced for AM-built parts after treatment. In addition, HIP relaxes residual stresses and reduces the notch sensitivity of the defects. It minimizes the degree of presence of internal pores and cracks but has an insignificant impact on the fatigue life of the metallic part (Ref 103). A high pressure in HIP reduces the gas pores, lack-of-fusion pores, blowholes, and microcracks formed inside the as-print sample by collapsing the pores through plastic deformation. With sufficient temperature and holding time, creep and diffusion mechanisms lead to material bonding and pore closure. Typically, the residual gas entrapped in the original powder particles without dispersion to the surface can be eliminated. HIP improves the overall tensile properties (e. g., 9% increase in elongation) of DLF-prepared stainless steel parts due to reduced porosity, amount of carbides and residual stress (Ref 104). Tran et al. reported that the cryogenic mechanical properties of DED-printed CrCoNi

MEAs at 77 K were effectively enhanced by HIP with increased tensile strength and no reduction in elongation
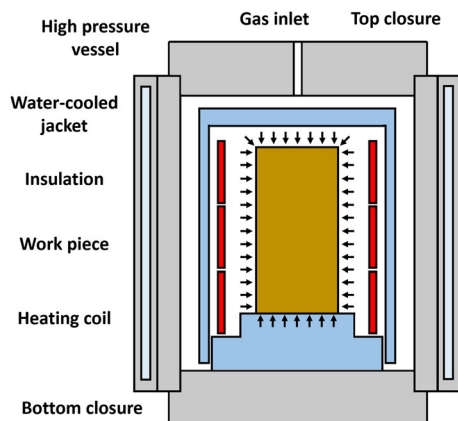

Fig. 3 A schematic of a typical HIP process

compared to those of as-built ones (Ref 105). Such combination of high strength and ductility results in increased strain energy density (56%) and decreased amount of micropores, as well as the work hardening effect caused by early activation of deformation twinning.

HIP significantly alters the grain morphology from an elongated columnar structure in build direction to a dominantly equiaxed grain structure formed through recrystallization. The structure change eliminates anisotropy, which can be concluded through EBSD result on Haynes 282 superalloy samples fabricated by SLM and post-treated with HIP (Ref 106). HIP also has capability of optimizing the secondary phase for its presence and distribution that either enhances the high-temperature strength or avoids the potential crack initiation at the interface. Slow HIP cooling rate also leads to the formation of hard secondary phases mainly within the grains and along the grain boundaries, thus forming a continuous film. HIP at 1250 °C with 145 MPa not only reduces the porosity and texture anisotropy of $Ni_{41}Al_{41}Cr_{12}Co_6$ alloy fabricated by SLM, but more critically enables the segregation of secondary

Table 2 Typical HIP process parameters for different metal-based materials

Material	HIP process
Ti-6Al-4 V alloy	900–960 °C for 2–4 h 100–120 MPa in argon and a natural furnace cool (Ref 59, 111–116)
	Super-transus HIP (1100 °C-100 MPa-2 h) and quench with $\sim$ 750 °C/min (Ref 117)
	927 °C for 5 h with 150 MPa and 5 °C/min heating and cooling rate (Ref 118)
SiC fiber/Ti6Al4V	890 °C for 2 h with 140 MPa (Ref 119)
Ti-48Al-2Cr-2Nb alloy	1200 °C for 4 h with 103.4 MPa (Ref 120)
TiAlNb alloy	1150 °C and 1200 °C for 4 h with 200 MP (Ref 121)
CoCr alloy	1200 °C for 4 h with 100 MPa and quench to 760 °C (Ref 122, 123)
MEA CrCoNi	1150 °C for 4 h with 101.3 MPa and furnace cool (Ref 105)
HEA Al_xCoCrFeNi	1100 °C for 2 h with 300 MPa and cool with 5 °C/min (Ref 108)
Mg alloy	450 °C for 3 h with 103 MPa (Ref 124)
AlSi10Mg alloy	500-530 °C at 100 MPa for 2–3 h and a furnace cool until 93 °C (Ref 125–129])
AlMgZrSc alloy	325 °C for 4 h with 100 MPa in argon (Ref 130])
Al-6061 H-18 alloy	580 °C for 1 h with 100 MPa (Ref 131)
Hastelloy X	1155-1160 °C for 3-4 h with 103 MPa (Ref 93, 132)
	1177 °C for 4 h with 150 MPa (Ref 109)
Inconel 718	1120–1170 °C for 2–4 h with 100 MPa (Ref 58, 133–135)
	1200 °C for 4 h with 103/120 MPa and uniform rapid quenching (Ref 83, 89, 91, 136)
	1185 °C for 3-4 h with 170 MPa furnace cool to 980 °C for solutionizing (Ref 137)
Inconel 625	1120 °C for 4 h with 100 MPa (Ref 138)
CM247LC	1177–1200 °C for 4 h with 103/150 MPa (Ref 63, 95)
Haynes 282	1185 °C for 3.5 h and 150 MPa (Ref 106)
K447A	1200 °C for 4 h and 150 MPa (Ref 139)
Rene88DT	1160 °C for 2 h and 200 MPa (Ref 140)
Ni41Al41Cr12Co6	1250 °C and 145 MPa (Ref 107)
NiFeMo	1230 °C for 3 h with 120 MPa (Ref 141])
WC–Co alloy	1420 °C for 30 min with 4 MPa (Ref 142])
WC-FeNiZr alloy	1350 °C for 3 h with 103.4 MPa (Ref 143)
Ultra-low carbon steel	1162 °C for 3 h with 101.7 MPa (Ref 144)
Stainless steel 410	1121 °C for 4 h with 103.4 MPa (Ref 110)
Stainless steel SC420	1100 °C for 2 h with 100 MPa (Ref 104)
H13 tool steel	1130 °C for 6 h with 100 MPa (Ref 145)
TiB_2/316L SS	1150 °C for 2 h with 207 MPa, rapid cool to 900 °C or 200 °C (Ref 146)
AlFe composite	485 to 525 °C for 2 h with 100 MPa (Ref 147)
Cu alloy	1075 °C for 2 h with 206.84 MPa (Ref 148)
	800-950 °C for 4 h with 100 MPa (Ref 149)
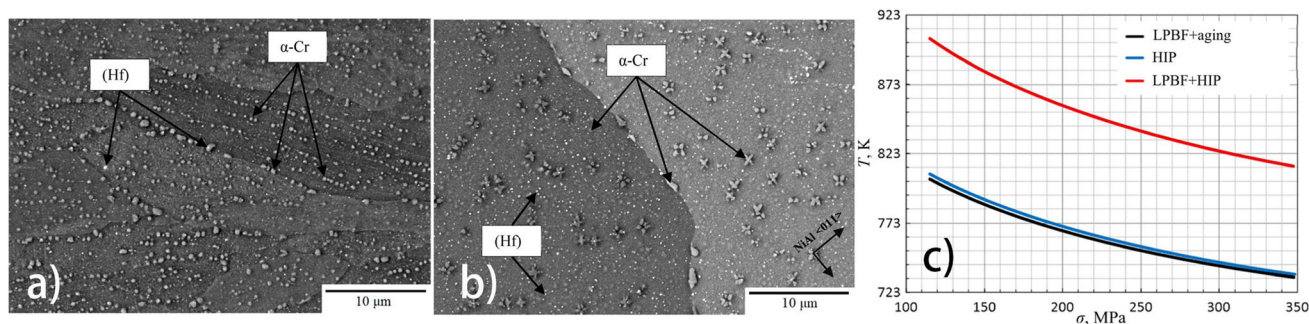
Fig. 4 SEM image of $Ni_{41}Al_{41}Cr_{12}Co_6$ alloy fabricated by SLM with post-treatment of (a) aging at 1150 °C for 3 h at vacuum, (b) HIP at 1250 °C with 145 MP, and (c) Maximum allowable operating temperature versus compressive load for $Ni_{41}Al_{41}Cr_{12}Co_6$ alloy workpiece with a lifespan ≥ 100,000 h, accumulated plastic strain ≤ 1%, and creep rate e = 10^{-4} s^{-1} (Ref [107]). Reprinted from Additive Manufacturing, Vol 31, Yu.Yu. Kaplanskii, E.A. Levashov, A.V. Korotitskiy, P.A. Loginov, Zh. A. Sentyurina, A.B. Mazalov, Influence of aging and HIP treatment on the structure and properties of NiAl-based turbine blades manufactured by laser powder bed fusion, Article 100,999, Copyright 2020, with permission from Elsevier

precipitations inside matrix grain (Fig. 4a and b) (Ref [107]). This significantly increases the maximum allowable operating temperature of the alloy workpiece by ~ 80 °C (for 100,000 h in the load ranging from 100 to 350 MPa) compared to aged one, as shown in Fig. 4(c). Joseph et al. stated that HIP not only eliminated the large pores (> 5 μm), but also induced the dissolution of grain boundary precipitates as well as grain coarsening of globular FCC/BCC structure in DLF-deposited AlxCoCrFeNi HEAs (Ref [108]). Furthermore, HIP exhibits effectiveness in reducing the thermal crack and thereby enhancing the overall high-temperature strength of the SLM-printed Hastelloy X sample (Ref [109]).

As a result, pore closure, microstructure homogenization, and densification occur simultaneously during HIP and thereby improving the overall mechanical properties of the final part. The elongation and plasticity can be greatly promoted because of the reduction of pores and solid solution of the secondary phase in the treated part. Owing to the reduced porosity and dislocation density, as well as the grain growth, the tensile ductility increases to more than 10-20% of the as-printed part, leading to continuous stress–strain curves of the specimens. Nonetheless, metallic components still can exhibit mechanical properties on parity with those of wrought metals and alloys (Ref [4], [110]). Annealing twins can also be observed in the microstructure after HIP.

HIP can be combined with other post-processing procedures to achieve a comprehensive result with superior properties of the AM part. For instance, the fatigue strength of machined specimens after annealing following HIP can achieve more than 10 times higher (Ref [150]). Also, with the sequence of HIP and then chemical etching, the residual internal pores are closed or at least significantly reduced by HIP, and the degree of the plate-pile like stacking defects is reduced by chemical etching. Depending on the duration, the chemical etching can have a slightly detrimental or beneficial effect on the ductility of HIP samples. More frequently, HIP is followed by traditional heat treatment, like solutionizing and aging (STA), to achieve a better combination of properties of the material. Zhao et al. found that HIP promoted both the tensile strength (5-10% increase to 1400 MPa) with less scattering and ductility (10 and 17% elongation before and after HIP) on LSF-printed Rene88DT specimens under following treatment of STA (Ref [140]).

In spite of the benefits that HIP can bring to AM metallic structures, HIP has its limitations. The HIP-treated metallic specimen typically exhibits increased ductility with a certain level of reduction in tensile strengths and sometimes even fatigue resistance due to microstructure coarsening developed during HIP. Although grain growth can be controlled by lowering the processing temperature and holding time, the coarsening of the grains and thereby the increased effective slip length reduce the YS, UTS, and toughness (Ref [151]). HIP increases the grain size to 3 times greater than that of as-built conditions for Ti-43.5Al-4Nb-1Mo-0.1B TNM-B1 alloy (EBM/SLM) (Ref [121]). The abnormal grain growth of WC and the surface roughness are the two major issues in post-HIP of PBF-built WC-Co and WC-FeNiZr alloys (Ref [142], [143]). Besides grain growth, phase transformation can be the other adverse effect of elevated temperature in HIP. Due to grain coarsening of B2 precipitate at grain boundary, HIP-treated DLF-deposited AlxCoCrFeNi HEA samples exhibit brittle fracture and reduced ductility in tension (Ref [108]). The undesirable secondary phases formed during HIP lead to a potential negative effect on creep performance. Figure 5 shows fracture surfaces examined in SEM for Inconel 718 specimen fabricated by SLM. HIP specimens are dominated by intergranular cracks due to excessive intergranular precipitations, while heat-treated and as-built specimens contain less and little intergranular precipitations, respectively. As a result, the creep lifetime for HIP specimens is only 25 and 40% as much as that of heat-treated and as-built specimens (Ref [136]). It is also noticeable that pores with a close distance to the exterior surface are ineffectively cured through HIP. The internal pores sometimes are not fully cured (Ref [113]). Many studies also report that post-heat treatment could reopen certain number of closed pores cured by HIP. Figure 6 demonstrates an illustration of reconstructed pores through μSXCT technique on Ti6Al4V samples fabricated by EBM. The β solution treatment of the HIPed sample regrows the gas porosity with a factor as high as 200% in size compared to those in HIPed status except for lack-of-fusion pores (Ref [111]). HIP generally impacts negatively on the hardness of the treated part (Ref [116], [147]). The hardness after HIP is similar to that of the solution annealed condition, but lower than that of the as-print and precipitation hardened condition. When a well-engineered alloy composition is presented during HIP, hardness can be improved. The dispersion hardening of 5 nm-sized Sc-rich fine dispersed and coherent Al_3Sc allows the specimen of AgMgZrSc alloy to achieve higher hardness (Ref [130]). Inhomogeneous distribution
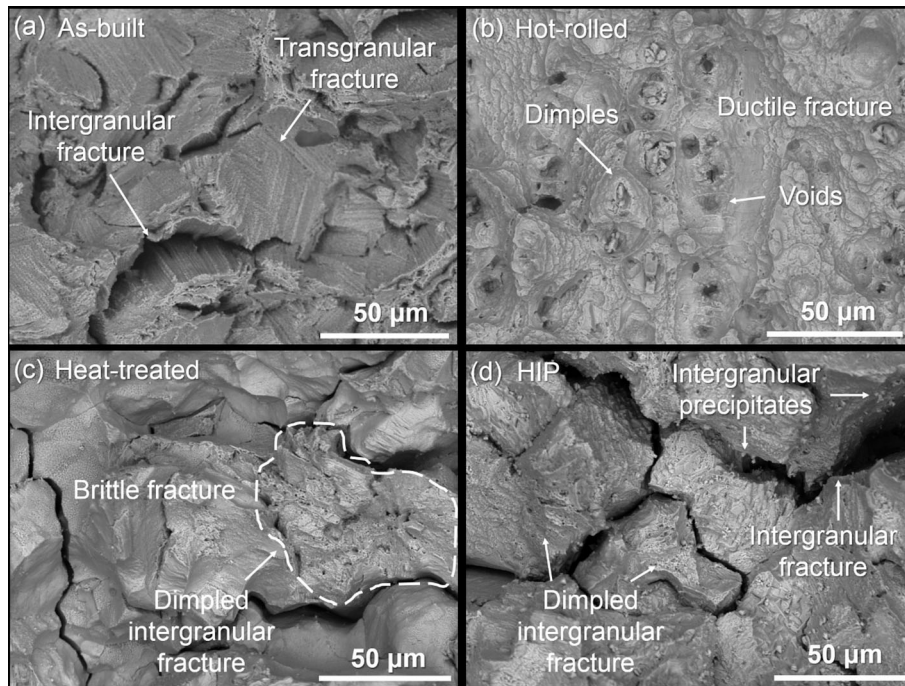
Fig. 5 SEM images of creep zone on the fracture surfaces of Inconel 718 specimen produced by SLM to show different fractures: (a) as-built, (b) hot-rolled (sheet material), (c) heat treatments (homogenization, solution, age), (d) HIP treatment (1200 °C, 103 MPa, 4 h) (Ref 136). Reprinted from Additive Manufacturing, Vol 24, Z. Xu, J.W. Murray, C.J. Hyde, A.T. Clare, Effect of post processing on the creep performance of laser powder bed fused Inconel 718, Pages 486–497, Copyright 2018, with permission from Elsevier
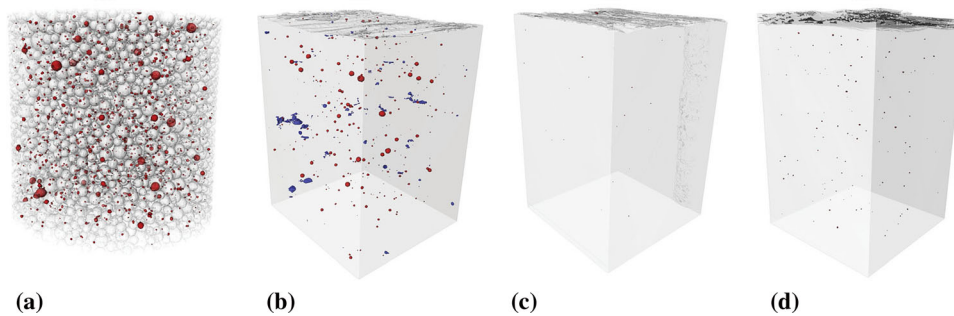

Fig. 6 Porosity scanned by μSXCT in Ti-6Al-4 V ELI powder and samples fabricated by EBM with treatments: (a) powder, (b) as-built, (c) HIP, (d) HIP + β solution treatment (Ref 111). Reproduced from Materials Research Letters under the CC BY 4.0 license

of certain elements in the build direction could not be completely healed through HIP. The atmosphere adopted in HIP also influenced the processed material. For example, when nitrogen is used in the chamber, the nitriding and formation of nitrides cause the specimen to lose plasticity significantly (Ref 152). Chemical transformation of nitriding lead to mass change as well as increase in strength and brittleness of the specimen. The existence of nitrides in the material is confirmed in microstructure observation. The allowable size of the part that can be treated in HIP is also restricted by conventional equipment. Specialized ultra-large HIP apparatus for large-scale production of AM specimen has been developed and utilized to address that issue (Ref 153).

In a study of IN718 alloy printed by SLM, HIP is experimented with temperature (500-1300 °C), pressure (500-1500 MPa), and holding time (2-4 h) followed by natural cooling in the furnace (Ref 154). HIP increases the relative density from 99.92% in as-built part to 99.98%. As shown in

Fig. 7, with increasing pressure and temperature in HIP, 100% density cannot be achieved due to the entrapped inert gas at the interparticle space. A critical temperature is identified to enable efficient densification in HIP. Further increasing temperature and pressure above 100 MPa does not achieve a lower porosity. A higher HIP temperature leads to greater tensile elongation and fracture stress due to larger grains. Moreover, HIP also induces a drop of the fatigue life. Overall, the heat treatment and cooling during HIP processing do not lead to age hardening of the samples.

Through means of x-ray microtomography analysis, it is confirmed that HIP significantly reduces internal porosity of AM-built metallic part, but sometimes it is ineffective to close pores connecting to the surface or gas entrapped pores (Ref 131, 155-158). Young's modulus is usually slightly promoted by HIP, while the elongation to failure (EL = 13.8%) of as-built samples significantly affects after HT (EL = 16%) and HIP (EL = 16.1%) (Ref 159). Poulin et al. demonstrated that HIP
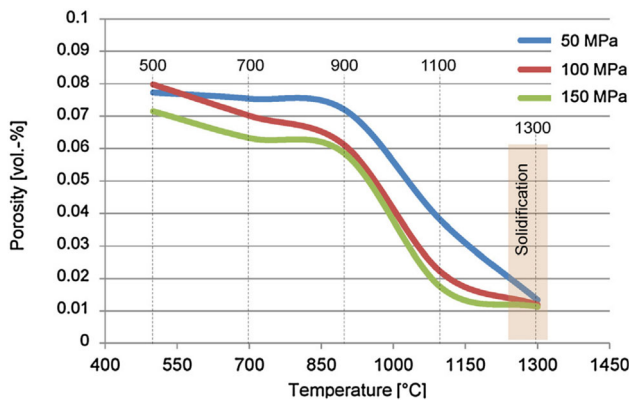
Fig. 7 Porosity changes of IN718 alloy samples fabricated by SLM after HIP at different temperatures and pressures (Ref 154). Reprinted from Additive Manufacturing, Vol 13, W. Tillmann, C. Schaak, J. Nellesen, M. Schaper, M.E. Aydinöz, K.-P. Hoyer, Hot isostatic pressing of IN718 components manufactured by selective laser melting, Pages 93–102, Copyright 2017, with permission from Elsevier

also reduced the overall pore size in SLM IN625 sample (Ref 138). Beside isotropic behavior, both modulus and elongation to failure are slightly improved compared to stress relieved samples. HIP shows less effectiveness on improving ductility of machined sample since pores removed in the as-built part have a heterogeneous spatial distribution with subsurface defects. The sample after HIP exhibits similar behaviors in tensile and torsion tests compared to wrought Ti6Al4V despite the microstructural transformation and thermal shrinkage (Ref 40). The HIPed specimen also shows less cyclic softening during plastic deformation. The failure mechanism is also insignificantly impacted by HIP. On EBM-fabricated IN718 sample, HIP does not induce considerable grain coarsening due to the pinning effect from the high fraction of carbides at the grain boundary (Ref 160, 161). This can also be observed in SLM-built AgMgZrSc alloy, in which Fe-rich particles precipitate at the grain boundaries (Ref 130). HIP also can promote the precipitation of Cr-rich carbides at grain boundaries in SLM Hastelloy X part. As a result, the tensile behavior is improved while the hardness and yield strength decrease after HIP (Ref 93, 132). HIP process has no significant influence on the density and hardness of the print samples produced by BJAM process, such as Stellite alloy (Ref 162). In addition, ultra-low carbon steel is also insensitive to HIP regarding densification (Ref 144). UAM-built 410 stainless steel (SS) can be enhanced by HIP on shear strength and hardness through grain boundary strengthening and formation of martensite (Ref 110). In contrary, UAM-built Al-6061 H-18 alloy exhibits reduced YS due to the recrystallization and the dissolution of strengthening precipitates (Ref 131). Besides tensile strength, HIP can also have an impact on thermal and electrical conductivity, such as Cu alloy produced by BJAM (Ref 148, 163).

The microstructure of the as-built Ti6Al4V or other alloy samples contain spherical pores ($< 100 \ \mu m$) and non-melted surfaces. HIP transforms the less ductile α-martensite structure to the more ductile α- β phase. HIP greatly heals the anisotropy effect in the microstructure by removing the process-induced defect and directional flaws (Ref 107, 120). HIP leads to coarsening of the alpha phase lamellae in the acicular microstructure. The α laths are widened from $\sim 1.0 \ \mu m$ in an as-built status to 3-4 μm, while there is no significant grain growth of the prior β grains since the

temperature is below the β-transus (920 °C). In contrast, super-transus HIP, which is conducted at temperature above 920 °C and rapid quenching, can improve the strength and reduce the anisotropy in the as-print microstructure compared to standard HIP cycle for EBM-fabricated Ti6Al4V (Ref 117). The fine basket weave structure with less degree of elemental partitioning and slightly coarser α can be obtained to achieve higher tensile strength with an isotropic behavior. The structure of CoCrMo alloy can also be altered by HIP treatment with a high density of stacking faults in the FCC Co-Cr grain matrix and more equiaxed grains. HIP at 1000 °C annealing temperature leads to a fully recrystallized fine structure of ultra-low carbon steel with reduced microhardness. For AlSi10Mg alloy fabricated by SLM, HIP leads to diffusion and agglomeration of Si into coarse granular phases with disappearance of grain boundaries and formation of needle-shaped intermetallic phase (Ref 126, 127, 129). Lee et al. reported that although no significant grain size change was observed in the microstructure of CM247LC alloy produced by SLM after HIP, different shapes of γ' phase were presented within the matrix γ phase, which considerably improved the tensile strength by 32% and elongation by 3 times (Ref 63).

As mentioned, the pores formed during the printing process act as crack initiation sites. As a result, the fatigue properties of as-built part can be substantially improved by HIP treatment (Ref 40). A higher fatigue limit can be achieved with up to 40% increase than that of as-built SLM-Ti6Al4V samples (Ref 164). The fatigue resistance and the number of loading cycles before failure for the EBM-Ti6Al4V specimens after HIP can reach to one to two orders of magnitude greater than those of untreated specimens(Ref 115). However, without prior treatment to remove the surface roughness like machining, HIP is statistically restricted on the promotion of fatigue properties of the as-built part (Ref 165). HIP itself does not affect the surface morphology and thus has no effect on reducing the surface roughness (Ref 166). Many studies indicate that a non-machined specimen has higher defect population on the surface, whereas the machined specimen is dominant to initiate cracks through internal porosity. A reduced fatigue strength, only 2/3 of the wrought material, can be induced in as-built samples due to the transition of microstructure and porosity (Ref 167). HIP shows little impact on the fatigue performance of IN718 and AlSi10Mg alloy fabricated by SLM due to the inclusions and brittle phases in the microstructure (Ref 168). Molaei et al. performed HIP to 17-4 PH stainless steel by L-PBF at 1120 and 105 MPa for 2.5 h, followed by solutionizing (1050 °C and 70 MPa for 20 min) and cooling at a rate of 200 °C/min (Ref 169). It was found that entrapped gas pores with a size of 70-80 μm were shrunk to below 10-20 μm after HIP applied and were below a critical size limit for fatigue. Consequently, the fatigue performance was improved by one order at higher cycles. HIP may additionally change phase structures in other alloy systems, which affects the fatigue behavior. Wu et al. performed HIP (1000 °C/150 MPa, 1 h) to a lattice structure fabricated by SLM and Ti6Al4V alloy, followed by furnace cooling (Ref 56) and found that the less ductile α'- martensite phase transformed back to the more ductile β phase while the untreated columnar β grains were converted to equiaxed grains. The endurance limits and fatigue strength at 10^6 cycles of the untreated and HIP-treated samples were 0.3 and 0.55, and 43 and 55 MPa, respectively. The quasi-static and dynamic studies of Ti6Al4V lattice structures show that HIP treatment increases the fatigue strength at the same surface condition of the lattice strut (Ref 61).

Grell et al. reported that HIP increased the impact toughness of print parts in all directions when the oxygen content level was lower than 0.5 wt% in the as-built structure of EBM Ti-6Al-4 V (Ref 170). HIP also increases the fracture toughness with improved uniform response for EBM-printed Ti-48Al-2Cr-2Nb alloy and stainless steel 316L specimen (Ref 120, 171). HIP typically promotes the corrosion resistance and mechanochemical performance of a metallic part. For Ti-6Al-4 V, HIP slightly improves the stability of passivation film and optimizes the phase composition when 3.5 wt.% NaCl solution and ambient temperature are applied (Ref 114), For CoCrMo alloy, HIP homogenizes the structure by dissolving the $Cr_{23}C_6$ carbide precipitates and eliminating corrosion sensitization which is caused by Cr depletion from the formation of these carbides (Ref 44). Wear resistance and hardness are both deteriorated after HIP when a high processing temperature and holding time are applied in SLM-printed TiB_2/316 SS composite (Ref 146).

In conclusion, the above-mentioned analysis indicates that the alloy design and the selection of HIP temperature as well as post-HIP cooling are crucial to the effectiveness of the HIP post-treatment on the metallic AM part.

2.2 Sintering/Infiltration

Sintering is essentially a heat treatment step that densifies a green body of powder compact to a solid with required microstructure. Such process adopts heat to coalesce particles without liquefaction of the particles. The sintering temperature is normally raised just below the melting temperature of major constituent of the material. Four categories of sintering can be defined as solid-state sintering, liquid phase sintering, viscous sintering, and vitrification. Sintering also includes hot pressing and hot isostatic pressing, both of which are assisted from external pressure. The driving force for this irreversible process is the reduction of the free energy of the system, which is associated with elimination of the internal surface area. The mechanism of the process identifies the pattern of mass transportation, for example, when referring to crystalline particles, surface diffusion, lattice diffusion, vapor transport, grain boundary diffusion, lattice diffusion, and plastic flow are the six common patterns defined. The final microstructure is required to be controlled against the coarsening of the grains, which is significantly affected by the particle size, surface condition, packing status, and grain boundary effect before sintering.

Infiltration is a process to fill the pores of a sintered material with a liquid metal or alloy that has a lower melting point. Under capillary force, the molten infiltrant is drawn into the interconnected pores of the skeleton and ideally fills the entire volume. The driving force of infiltration is also the reduction of surface free energy. Infiltration is promoted by a low wetting angle of the liquid with the solid and a pressure gradient. Highly alloyed infiltrants such as eutectic alloy AlSiMg or AlCu have been developed to enhance the final density of aluminum alloy, but normally also cause a reduced ductility of the infiltrated part ($< 1\%$) (Ref 172). For one-step process, a full furnace cycle of infiltration includes preheating for lubricant burn-off, pre-sintering, and finally infiltrating when the infiltrant compact is in contact of the sintered part within the chamber. The double-step process requires sintering of the target material first. The infiltration parameters are the infiltration temperature (reduction of the viscosity of the infiltrating liquid) and the dwell time above the liquidus of the infiltrating liquid. Short times are preferred to limit extensive reaction of the liquid with the skeleton. Infiltration can be advantageous compared to liquid phase sintering when the liquid is insoluble in the skeleton material. For a Fe-Cu system, the infiltrating powder is consisted of copper alloy base plus a substantial amount of iron, lubricant, graphite, nickel, manganese, etc. Special element can be added in the infiltration system to lower the surface tension of the liquid melt, thereby increasing the infiltration rate and final density.

As mentioned in HIP process, porosity is not desired as it causes stress concentration during loading and acts as crack initiation sites. The porosity can be effectively reduced by sintering and infiltration. Sintering induces bridging among the metallic particles accompanied with reduced surface area and energy, while infiltration introduces metallic materials in a liquid form into the porosity (Ref 96, 98, 100, 173, 174). The infiltration process uses chemical vapor for deposition or, more commonly, a low melting metallic liquid to wet and infiltrate into the porous and rigid ceramic or metallic structure at ambient or elevated pressure. The infiltrated material forms a new phase, sometimes through reaction, which greatly reduces the porosity (Ref 175). The sintering and infiltration processes can be used alone or in combination to reduce porosity and improve mechanical properties.

The grain size of BJAM-built metallic structure after sintering can be estimated through the following equation (Ref 97, 176):

$$D_{\text{sinter}} = \frac{0.6 \times D_{\text{initial}}}{\sqrt[2]{1 - f_s}}, \quad \text{(Eq 10)}$$

where D_{sinter} is the grain size after sintering, f_s is the fractional density of the sintered material, and 0.6 is a coefficient of a typical fractional green density of $\sim 60\%$. The tensile strength of porous material can be estimated using the equation as follows (Ref 177):

$$\sigma = \sigma_0 K \left(\frac{\rho}{\rho_t}\right)^m, \quad \text{(Eq 11)}$$

where σ is the tensile strength of the porous material, σ_0 is the strength of the wrought material, ρ and ρ_t are the density of the porous material and its theoretical density, respectively, K is equivalent to a stress concentration factor due to the pores, and m is the exponential dependence of strength on porosity. Both parameters depend on the processing conditions, and the equation is valid in the absence of any microstructural problems. Furthermore, the yield strength of a BJAM-built specimen after sintering and infiltration can be estimated under the assumption listed below:

1. The yield stress is determined in bend test when specimen starts to fail,
2. The yield stress of the infiltrated material can be approximated by an iso-strain model.

Thus, the strength of the sintered skeleton in the sintered material ($\sigma_{\text{sint}}^{\text{SS}}$) and the infiltrated material ($\sigma_{\text{inf}}^{\text{SS}}$) can be written as (Ref 12):

$$\sigma_{\text{sint}}^{\text{SS}} = \frac{\sigma_{\text{TR}}}{(1 - P)}, \quad \text{(Eq 12)}$$

$$\sigma_{\text{inf}}^{\text{SS}} = \frac{\sigma_{\text{TR}} - f_{\text{inf}} \sigma_{\text{inft}}}{(1 - f_{\text{inf}})}, \qquad \text{(Eq 13)}$$

where σ_{TR} is the transverse rupture strength, P is the porosity of the sintered material, f_{inf} is the volume fraction of the infiltrant, and σ_{inf} is the yield stress of the infiltrant, which can be estimated from the hardness (H) of the infiltrant using Tabor relation ($\sigma \sim H/3$).

The ductility of porous material has an expression in the ratio to the wrought material (Ref 178):

$$Z = \begin{cases} \frac{(1-\varepsilon)^{1.5}}{(1-c\varepsilon^2)^{0.5}}, & \varepsilon < 0.15 \\ \frac{(1-\varepsilon)^{1.5}}{(1-0.15^2 c)^{0.5}}, & \varepsilon > 0.15 \end{cases}, \qquad \text{(Eq 14)}$$

where Z is the relative ductility (ratio of elongation of porous material to wrought material), ε is the porosity, and c is a coefficient representing the sensitivity of the ductility to porosity for the material under consideration.

The kinetics of infiltration is explained by the Washburn equation to estimate the infiltration time, which can be written as follows (Ref 173, 179):

$$t = \frac{h^2}{\frac{\rho r^2}{4\mu} \left(\frac{2\gamma_{LV} \cos\theta}{\rho r} - gh \right)}, \qquad \text{(Eq 15)}$$

where t is the time, h is the height of the capillaries or height of the specimen (assumption for simplicity), ρ is the density of the infiltrating material, r is the average radius of the pores, μ is the viscosity of the infiltrant, γ_{LV} is the surface tension between the infiltrating material and solid preform, θ is the contact angle, and g is the gravitational constant. Dissolution kinetics can be estimated using the Noyes-Whitney relationship shown below (Ref 173):

$$\frac{dm}{dt} = A \frac{D}{d} (C_s - C_b), \qquad \text{(Eq 16)}$$

where m is the mass, t is the time, A is the surface area of reinforcement material, D is the mixed diffusion coefficient, d is the diffusion distance, C_s is the concentration of saturated solute, and C_b is the initial concentration of solute. Equation 10, 11, 12, 13, 14, 15 and 16 describe the effect of sintering and infiltration and their kinetics on treating porous metallic structure.

A proper sintering practice can allow the green body to reach a sintering density over 90, up to 99%, which can be illustrated in reconstructed μCT scan images (Ref 9). Generally, higher sintering temperature and time promote the mechanical properties. Cordero et al. found that after bronze infiltration the transverse rupture strength of the iron specimen produced by BJAM is 4 times higher than that of the sintered structure (Ref 12). Cramer et al. conducted sintering (1600 °C, 4 h) and melt infiltration of Co (1520 °C, held at 1 and 60 min separately) to a WC preform by BJAM. The hardness of the as-printed structure was 4.8 GPa and increased to 5.9 and 6.6 GPa by sintering combined with infiltration for 1 and 60 min, separately (Ref 173). Xu et al. printed 98 wt.% high alloyed steel (HAS) microparticles and polylactic acid (PLA) in dichloromethane (DCM) by extrusion, and performed sintering (1165 °C, 6 h) followed by infiltration with 10 vol.% copper liquids (Ref 99); apparent bridging was found among the

metallic particles after sintering, and porosity was reduced from 15% to 0.2% after infiltration. As a result, the post-treated AM structures greatly increased tensile modulus and strength. Meanwhile, the sintering conditions may affect the final mechanical properties of the AM metallic structure. The elastic modulus increased from 3.1 to 196 and 195 GPa after sintering and copper infiltration, respectively. Xie et al. prepared 316 SS sample through SLS process with post-sintering from 300-1300 °C in several isothermal steps. The sintering completely removed the binder of ethylene–vinyl acetate copolymer and reduced the total porosity to 28% (Ref 180). Vennilaa et al. adopted copper alloy to infiltrate the SLS-produced stainless steel part and studied the hardness improvement through Taguchi method (Ref 181). Kumar et al. carried out a series of experiments of bronze infiltration on SLS-built iron-based alloy. The result showed that infiltration increases the density of the sintered part from 5 to 19%, which is dependent on powder composition and laser input power. The bronze-filtrated specimen may exhibit higher hardness or bending strength as well (Ref 182).

2.3 Traditional Heat Treatments

It is challenging to adjust the final microstructure by HIP or sintering only, and infiltration treatments are relatively sophisticated and costly with additional substances required (Ref 183). They are also incapable of fully solving other major problems like residual stress, limited ductility, low fatigue performance, and poor corrosion resistance. Heat treatments (HT) can solve those issues and improve the performance of AM metals. Therefore, HTs are more routinely used techniques for post-treating AM metallic structures (Ref 66, 67, 81, 86, 184, 185).

HT allows the metallic structure subjecting to a definitive time-temperature cycle that consists of heating, soaking, and cooling. HT plays a positive role in improving the physical properties, such as hardness, ductility, strength, corrosion as well as fatigue resistance, and their consistency with less deviation. However, heat treatments have limitations. HT is not capable of eliminating internal nor surface pores. It shows a negligible effect on further reducing porosity on specimens after HIP. The resulting microstructural changes and/or coarsening after HIP can cause strength reductions, while subsequent HT may lead to the reappearance of certain defects (Ref 186). HT sometimes also is ineffective in promoting the tensile strengths. In addition, it may cause a detrimental impact upon the repeatability in mechanical properties of treated specimen (Ref 187). Common alloy heat treatment methods include stress relieving, solid solution (T4), aging (T5), and solid solution + aging (T6).

Annealing is the process of heating up and maintaining a material at a specific temperature and then cooling it at a suitable rate according to the application. The main purpose of this process is to soften a material for improved machinability, cold working or to enhance electrical or mechanical properties. In general, annealing reduces porosity and residual stress. However, annealing at low temperatures (often referred to as aging) can induce precipitated reinforcing phases which increase strength (Ref 188). Dislocations can also be preserved at these low temperatures to maintain strength and hardness. In contrast, annealing above the recrystallization temperature can greatly "reset" grain structures, accompanied with grain growth and largely reduced dislocation density (Ref 189),

which consequently decreases the strength (Ref 190, 191). Thus, annealing at specifically selected temperatures is crucial for the final mechanical properties (Ref 69).

Steel is annealed and slow cooled to improve the ductility and refine the grain structures. As one of the annealing treatment, stress relieving only removes or reduces the internal stresses of a material, which is usually achieved by holding below the lower critical temperature. For steel, annealing has several different types, including heating above the upper critical temperature to form hypoeutectoid structure. Process annealing softens the cold-worked ferritic grains of the steel and recrystallization for further cold work. Spheroidizing typically applied to high carbon steels to refine the pearlite and form globular form of carbide in a matrix of ferrite.

Stress relieving (SR) is frequently used for AM manufactured parts to reduce the residual stresses left in the part from manufacturing and can have a significant impact on the mechanical properties, surface quality and microstructure. SR requires a protective atmosphere of inert gas or vacuum to avoid the occurrence of chemical reaction at elevated temperature. It is also suggested to be conducted on the part before separating from the substrate. Residual stresses can be either on the macroscopic scale affecting dimension and geometry of the whole component or on the microscopic scale changing grains size.

T4 treatment (solid solution) is the process that heating to a sufficient high temperature causes one or more of the alloying constituents to form a solid solution within the metal. Solutionizing can reduce and eliminate the microsegregation, dislocation networks, and promote recrystallization as well as homogenization of microstructures in AM metallic parts. T4 followed by a rapid cool in steel alloy leads to a structure with evenly distributed carbon phase and austenite. Both solution treating and annealing reduce the work hardened condition and undesirable impact from brazing, welding, and laser cutting for further processing. T4 significantly improves ductility but reduces YS. In addition, T4 treatment reduces susceptibility to intergranular stress corrosion and embrittlement also to increase high-temperature creep strength.

T5 (aging) treatment allows the metallic structure to be subjected to a long lower temperature heat treat cycle to develop an alloy specific microstructure. Aging increases strength by producing precipitates of the alloying element within the structure. It also enables precipitation hardening and thus gives more control over hardness by uniformly dispersed particles within grain structure to hinder the movement of atoms, consequently limiting dislocation occurrence in the materials. Typical T5 designations are H900 or H1075, which specify aging at 900 °F for one hour and at 1075 °F for 4 h, respectively. The T7 over-aging treatment aims at reducing residual stress while increasing the performance of the alloy with a higher processing temperature.

T6 treatment, which includes both solutionizing and age hardening (STA), increases the UTS but reduces the YS and ductility. After solution treating, the subsequent precipitation age hardening allows controlled release of the constituents either naturally (at room temperature) or artificially (at higher temperatures). Precipitation strengthens materials by generating precipitate clusters which significantly enhance the strength of the component. STA also improves the mechanical behavior and corrosion resistance at elevated temperature. Between solution treating and age hardening, austenite conditioning treatment and fast cooling can be adopted as intermediate

processing steps to treat metastable alloys to achieve desired properties. Such comprehensive STA treatment ensures the transformation from austenite to martensite in alloys.

For steels and nickel alloys, STA is normally performed under vacuum or in inert gas with rapid cooling. The STA-treated samples exhibit higher hardness and toughness than the sintered samples, which is attributed to the carbide precipitates dissolved by the solutionizing and formation of intermetallic precipitates during the aging process. While for aluminum alloys, solution treating is typically performed in air, followed by rapid quenching into various cooling medium. Fully annealing and slow cooling are required before STA for aluminum alloys. STA dissolves any precipitates present in the material and forms a single phase before re-precipitating desired secondary phases.

There are other thermal treating approaches. Normalizing is done on ferrous metals that undergo manufacturing processes to relieve the internal stresses by heating to a specific temperature higher than STA and cooling in open air. Normalizing provides uniformity in grain structure and maximum toughness. Tempering reduces the brittleness and internal stress especially for quenching by heating to a temperature below hardening and cooling in still air. A higher tempering temperature is benefit for resuming the ductility and build toughness. Typical HT approaches used for AM metal parts are listed in Table 3.

Heat treatment as post-processing for different AM techniques varies intrinsically. For example, EBM typically does not require a stress relieving heat treatment due to the elevated temperature for fully melting of the powder (Ref 192). The residual stresses that develop during SLM promote the formation of equiaxed grains during heat treatment-induced recrystallization reactions (Ref 193). Post-spray heat treatment (PSHT) is specifically developed as a post-thermal treatment for CSAM. PSHT can increase the density of the printed component by eliminating pores and diminishing the anisotropy in the microstructure. It also improves the strength as well as the ductility. Overall, optimization of the post-processing HT can control the microstructure, grain size, and distribution of precipitate for hardening and improve strength and creep properties, as well as fatigue, long-term stability, and hot corrosion resistance properties of the AM manufactured part. Typical process parameters of HTs for different metallic materials produced in AM are listed in Table 4.

Traditionally, when heat treating of Ti6Al4V for SR, temperature could be as low as 675 °C for holding and a cooling rate could be at less than 2.5 °C/min to maintain the achieved microstructure. A typical subcritical annealing or stress relieving leads to the transformation of the metastable martensite into a duplex α-β matrix, which increases ductility up to 30% with slightly reduced strength (Ref 6, 211). SR at a lower temperature does not change the microstructure significantly but may lead to fatigue crack growth (Ref 197). When SR is applied on SLM Ti6Al4V samples, it minimizes residual stress generated from the high cooling rates (Ref 194, 195). The annealing procedure should be performed in vacuum furnace to avoid oxidation and at a temperature close to the β-transus temperature of 1000 °C. Isothermal annealing is studied by applying to Ti6Al4V at 900, 920 and 950 °C (Ref 212). At 900 °C, α-platelets phase starts to form at the grain boundaries from the metastable α' phase. Sub-transus annealing at 920 °C obtains a dual-phase $\alpha + \alpha$' microstructure when the temperature is increased to 950 °C, and the microstructure evolves to a composition with an increasing portion of coarsen α-platelets

Table 3   Description of typical heat treatment methods for post-treating AM metallic structures

HT method	Description and effect	Process temperature
Annealing (Stress relieve)	Soften the structure to free internal stress, promote a homogenous chemistry, equiaxed microstructure, and uniform mechanical properties	Below the lower critical temperature and slow cooling
STA	Annealed to form an oversaturated solution, followed by aging to obtain reinforcing precipitates	Above solutionizing temperature
Process annealing (recrystallization)	Annealed at high temperatures to induce recrystallization and grain growth, reduce porosity and defects, and eliminate dislocations	Above recrystallization temperature
Homogenization annealing	Annealing at high temperatures for a long period and subsequent cooling	Below solidus line, allowing atom diffusion

**Table 4   Typical heat treatment parameters for different metal-based materials**

| Material	Heat treatment	Heat treatment process
Ti-6Al-4 V	Stress relieving #1	820 °C in 4 h, hold for 1.5 h, and slow cooling to 500 °C (Ref 164)
	Stress relieving #2	730-750 °C for 1-2 h
	Stress relieving #3	480 °C for 2 h (Ref 118)
	Stress relieving #4	800 °C for 2 h furnace cool (below β-transus) (Ref 194)
	Stress relieving #5	550 °C for 2 h
	Stress relieving #6	700 °C for 1 h and air cool (Ref 195)
	Annealing #1	913 °C for 2-4 h and furnace-cooled below 427 °C
	Annealing #2	927 °C for 2 h with 5 °C/min heating and cooling rate (Ref 118)
	Annealing #3	920 °C, for 2 h, followed by water quenching (Ref 196)
	Annealing #4	1050 °C for 2 h furnace cool (above β-transus) (Ref 197)
	Annealing #5	700 °C for 1 h and free convection cooling to room temperature (Ref 40)
	Annealing #6	800 °C for 2 h furnace cool (below b-transus)
	Annealing #7	870 °C for 36 h/650 °C for 8 h/1000 °C for 3 h (Ref 20)
	Duplex annealing #1	910 °C for 8 h and water quenching, then 750 °C for 4 h and furnace cool
	Duplex annealing #2	920 °C for 1 h and air cool, then 1100 °C for 1 h and air/furnace cool (Ref 198)
	STA	967 °C for 1 h and water quenched, then aged at 595 °C for 2 h air-cooled (Ref 118)
	β solution treat	1050 °C for 10 min
Inconel 718	Stress relieving	1065-1066 °C for 1.5 h and furnace cool (Ref 134, 199)
	Homogenizing #1	1177 °C for 1 h with 0.2 MPa and cooling at 38 °C/h to below 538 °C (Ref 199])
	Homogenizing #2	1093 ± 14 °C for 1-2 h, air cool (Ref 136)
	Annealing	980 °C for 1 h and air cool (cooling rate of 100 °C/min)
	Aging	720 °C for 8 h and furnace cool to 620 °C in 2 h, then hold for 8 h and air cool (cooling rate of 100 °C /min) (Ref 168)
	STA #1	1066 °C for 1 h and argon quenched to 65 °C, then 760 °C for 10 h and furnace cool, then 650 °C for 8-10 h and argon cool to room temperature (Ref 83, 90, 91, 134, 200)
	STA #2	980 °C for 1 h with 157 MPa rapid cool to room temperature, then 740 °C for 8 h with 138 MPa furnace cooling, then 635 °C for 10 h with rapid cooling (Ref 137)
	STA #3	980 °C for 1 h and air cool, then 720 °C for 8 h and furnace cool 620 °C (Ref 89)
	STA #4	980/1120 °C for 2 h, then 720 °C for 8 h, then 620 °C for 10 h (Ref 160)
	STA #5	982 °C for 1 h and argon fan cool to < 149 °C, then 718 °C for 8 h and furnace cool to 621 °C holding for 18 h, then argon fan cool to < 149 °C (Ref 134, 136, 199)
	STA #6	1030 °C for 1.5 h and water quench, then 780 °C for 7 h and air cool (Ref 92)
	High-pressure HT	1185 °C for 4 h with 170 MPa and argon quench to 1030 °C for 1.5 h with 145 MPa and argon quench, then aging 780 °C for 7 h and air cool(Ref 92)
Inconel 625	Stress relieving	870 °C for 1 h (Ref 138)
CM247LC	STA	1177/1232/1260 °C for 2 h and oil quench, then 1079 °C for 4 h and air cool, then 871 °C for 20 h and air cool (Ref 95)

Table 4 continued

Material	Heat treatment	Heat treatment process
Haynes 282	Solution treat	1120 °C for 2 h followed by water quench (Ref 106])
	Aging	1000 °C for 2 h and furnace cool, then 788 °C for 8 h and furnace cool
CMSX-4	STA	1300 °C for 15 min and water quench, then 1140 °C for 2 h and water quench, then 870 °C for 4 h (Ref 201)
Hastelloy X	STA #1	1172 °C for 30 min and water quench, then 745 °C for 6 h water quench (Ref 93)
	STA #2	1100 °C for 1 h, water quench, 720 °C for 8 h, 620 °C for 10 h, air cool (Ref 202)
DZ125	STA	1180 °C for 2 h, then at 1230 °C for 3 h and rapid cool, then γ' precipitation aging at 1100 °C for 4 h, then 870 °C for 20 h and rapid cool (Ref 94)
$Ni_{41}Al_{41}Cr_{12}Co_6$	Aging	1150 °C for 3 h (Ref 107)
$Al_{0.5}CrMoNbTa_{0.5}$	Homogenizing	1000/1300 °C for 24 h (Ref 203)
FeCrCoMnNi	Annealing	500/700/900/1100 °C for 4 h and furnace cool (Ref 72)
CoCrW	Solution treat	1100-1200 °C for 1 h (Ref 204)
CoCrMoW	Stress relieving	450 °C in 1 h and hold for 45 min, then heat to 750 °C in 45 min hold for 60 min, then natural cool to $\sim$ 600 °C, then air cool to $\sim$ 300 °C (Ref 205)
NiFeMo	Aging	550 °C for 1 h, then 1150 °C for 4 h, then slow cool to 200 °C (Ref 141)
Steel	Stress relieving	650 °C for 8 h (Ref 145)
	Annealing #1	1050 °C for 0.5 h and air cool, then 552 °C for 4 h and air cool (H1025)
	Annealing #2	727 °C for 1–2 h
	Annealing #3	950 °C for 4 h and furnace cool (Ref 206)
	Hardening and Tempering	Austenitize in vacuum at 1020 °C for 70–75 min and quench by nitrogen, then Twice temper at 585 °C for 2.25–3 h (Ref 145)
	Isothermal treat	500-700 °C for 1 h (Ref 158)
	Solution treat #1	900-1000 °C for 1 h and water quench (Ref 207)
	Solution treat #2	1000–1200 °C for 1 h and water quench, then 1200 °C for 4 h and WQ (Ref 71)
Al alloy	T5 #1	285-300 °C for 2 h and air cool (Ref 128)
	T5 #2	190-200 °C for 2 h and air cool
	Annealing #1	240 °C for 6 h and furnace cool (Ref 208)
	Annealing #2	200 °C/300 °C
	T6 #1	520-530 °C for 1 h and water quench, then 160 °C for 6 h
	T6 #2	540 °C for 8 h and water quench, then 160 °C for 10 h and oil bath (Ref 127)
	T6 #3	520 °C for 5 h and water quench, then 160 °C for 12 h and air cooling
	Solution treat	530 °C for 1 h or 5 h and water quench (Ref 209)
	Aging	160 °C for 10 h
Fe-Al alloy	Stress relieving	500 °C for 6 h (Ref 210)

and an intersected β matrix, which shows the sensitivity of the martensitic microstructure to annealing temperature. Specifically, annealing at 500 °C leads to a significant increase of the mechanical properties due to the strengthening of the dispersed fine β precipitates in the metastable α' martensite (Ref 196). Statistically, annealing or SR has little impact on the fatigue behavior of the EBM-produced Ti6Al4V parts but only further coarsens the microstructure (Ref 165). As shown in Fig. 8, both HT and HIP increase the elongation, but have insignificant impact on YS and UT. Meanwhile, HT samples show almost identical fatigue behavior and S-N curves while HIP promotes the maximum fatigue strength from $\sim$ 450 to $\sim$ 600 MPa at 10^7 cycles to failure (Ref 156). Annealing at an excessive temperature, especially above the β-transus, is not recommended since it can result in undesired overgrowth of the α-platelets. High annealing temperatures fully decompose the martensite to fine lamellae β phase and coarsen the microstructure, which leads to 6-7% decrease in strength while little improvement in ductility compared to as-built parts (Ref 118). Only super-transus annealing can transform columnar grains to equiaxed prior-β phase grains, and meanwhile turn basketweave α to lamellar microstructure (α lamellae within prior-β grain) (Ref 198). Fast cooling in air post-super-transus annealing results in fine colonies and laths with greater strength than that of sub-transus. Super-transus air-cooled sample shows limited deformation and ductility with intergranular fracture, while the furnace-cooled sample has improved ductility. STA treatment for Ti6Al4V components involves firstly solution treating to develop a larger β-phase fraction followed by quenching and subsequent aging to decompose the unstable β phase. Normally, STA treatment refines the microstructure of AM-fabricated Ti6Al4V, promoting the strength up to more than 10% but with $\sim$ 30% decrease in ductility. Figure 9 illustrates a summary of yield strength vs. total elongation to failure for Ti6Al4V specimen fabricated by SLM, EBM, and DED with post-processing of HT and HIP. HIP on SLM-produced Ti6Al4V eliminates the defects such as porosity and lack of fusions and transforms martensite into lamellar, while for EBM as-built Ti-6Al-4 V, HIP mainly removes all the pores and other defects but only coarsens the lamellar microstructure. DED produced Ti6Al4V specimens exhibit more scattering in tensile properties and low ductility with moderate strength. Xu et al. performed annealing treatments to SLM-built Ti6Al4V alloys under 700, 750, and 799 °C for 4 h followed by air cooling (Ref 65). Transformation from α' to $\alpha + \beta$ precipitate increases with annealing temperature, reducing the α/β interface areas that are vulnerable sites for corrosion. Also, β phase has higher corrosion resistance due to its ability to form a more
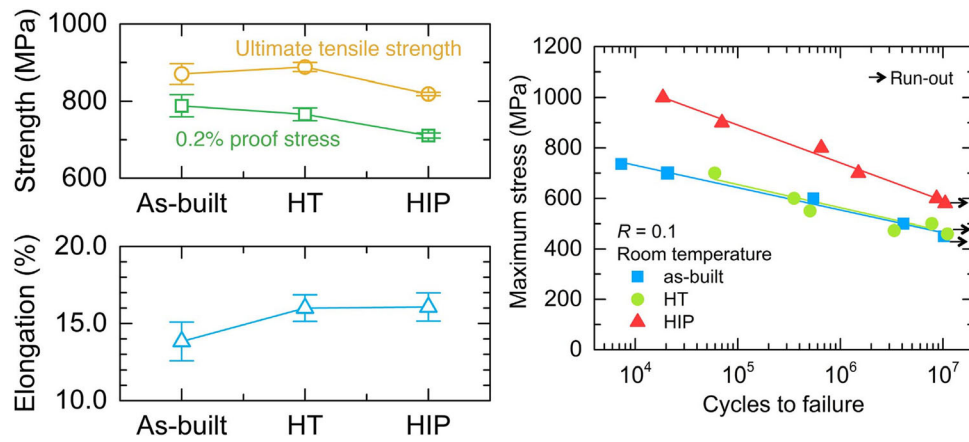
Fig. 8 The measured YS, UTS, elongation, and S–N curve for EBM-built Ti6Al4V alloy specimen at as-built, HT (920 °C, 2 h), and HIP (920 °C, 100 MPa, 2 h) conditions (Ref 156). Reprinted from Materials Science and Engineering A, Vol 680, Xiaoli Shui, Kenta Yamanaka, Manami Mori, Yoshihiko Nagata, Kenya Kurita, Akihiko Chiba, Effects of post-processing on cyclic fatigue response of a titanium alloy additively manufactured by electron beam melting, Pages 239–248, Copyright 2017, with permission from Elsevier
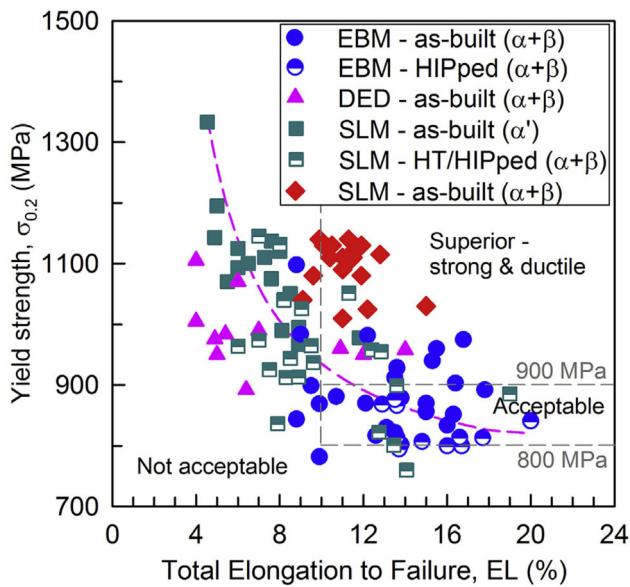
Fig. 9 Yield strength vs. total elongation to failure for Ti-6Al-4 V manufactured with different AM process and post-processing approaches (Ref 213). Reprinted from Acta Materialia, Vol 125, W. Xu, E.W. Lui, A. Pateras, M. Qian, M. Brandt, In situ tailoring microstructure in additively manufactured Ti-6Al-4 V for superior mechanical performance, Pages 390-400, Copyright 2017, with permission from Elsevier

stable oxide film, and it increased from 2.1 to 6.6, 8.5, and 9.4% for the as-printed sample with increasing annealing temperatures.

Most AM-produced Ni-based superalloys exhibit a substantial degree of inter-dendritic segregation and other undesirable intermetallic phases. As a result, a two-step treatment of HIP + STA is developed and adopted to reduce the defects and create the optimum size and fraction of precipitates for high-temperature applications (Ref 214). IN718 specimens fabricated by EBM is subjected to STA and a combination of HIP + STA (Ref 83, 160). Solution treating at 1120 °C for 2 h is sufficient to dissolve δ-needle phase without significant coarsening. A complete STA treatment enables precipitation of

δ-needle phase in a relatively small size, promotes little grain growth, and increases the hardness compared to as-built condition. After HIP + STA, the size distribution and volume fraction of the NbC precipitation remain unchanged. Significant difference in phase composition is also observed after STA (980 °C, then 720 °C, then 620 °C) and HIP (1200 °C) + aging (720 °C, then 620 °C) (Ref 89). STA sample contains more δ and γ'' phases, while HIP sample has a greater amount of carbide and γ' phases. HIP sample also exhibits a higher degree of oxidation resistance at 900 and 1000 °C. The HIP + STA homogenizes the precipitate phase and retains the columnar grain structure, leading to the improvement in YS, UTS and fatigue strength at both room temperature and 650 °C (Ref 90). SR alone can homogenize the microstructure of IN718 samples and lower the compressive residual stress that attributes to the evolution of the phase composition. A combination treatment of SR, homogenization, and STA substantially reduces the anisotropy but promotes the strength due to formation of coherent twins and γ'/γ'' precipitates as well as increased equiaxed grain morphology (Ref 199). Such combined treatment also significantly increases the maximum strength of the specimen during cyclic loading and leads to strain heterogeneity as well as localization. A comprehensive study of IN718 fabricated by SLM, BPD, and WAAM shows that the YS and UTS for all three types of printed parts are similar in value in spite of the slight difference in as-built status and heat treating details (Ref 134). HIP eliminates the concentration gradient, while a lower solution treat temperature leads to finer grain size and greater elongation to failure for all the samples. IN718 EBM part after HIP + STA treatment has a better creep performance when it is dominated by columnar grains rather than equiaxed grains in microstructure (Ref 91). HIP and heat-treated specimens yielded a mean of 20 h and 90 h creep lifetime at conditions of 650 MPa and 650 °C compared to 55 h of as-built condition (Ref 136). The excessive intergranular precipitation after HIP causes the shortest creep lifetime due to intergranular cracking under creep condition. The measured hardness of the specimen can be ranked from high to low at the conditions of STA, high-pressure HT + aging, HIP + STA, and HIP + aging (Ref 92). STA promotes the portion of retaining γ'' in comparison to the as-built material and thereby resulting a higher microhardness of the print part.
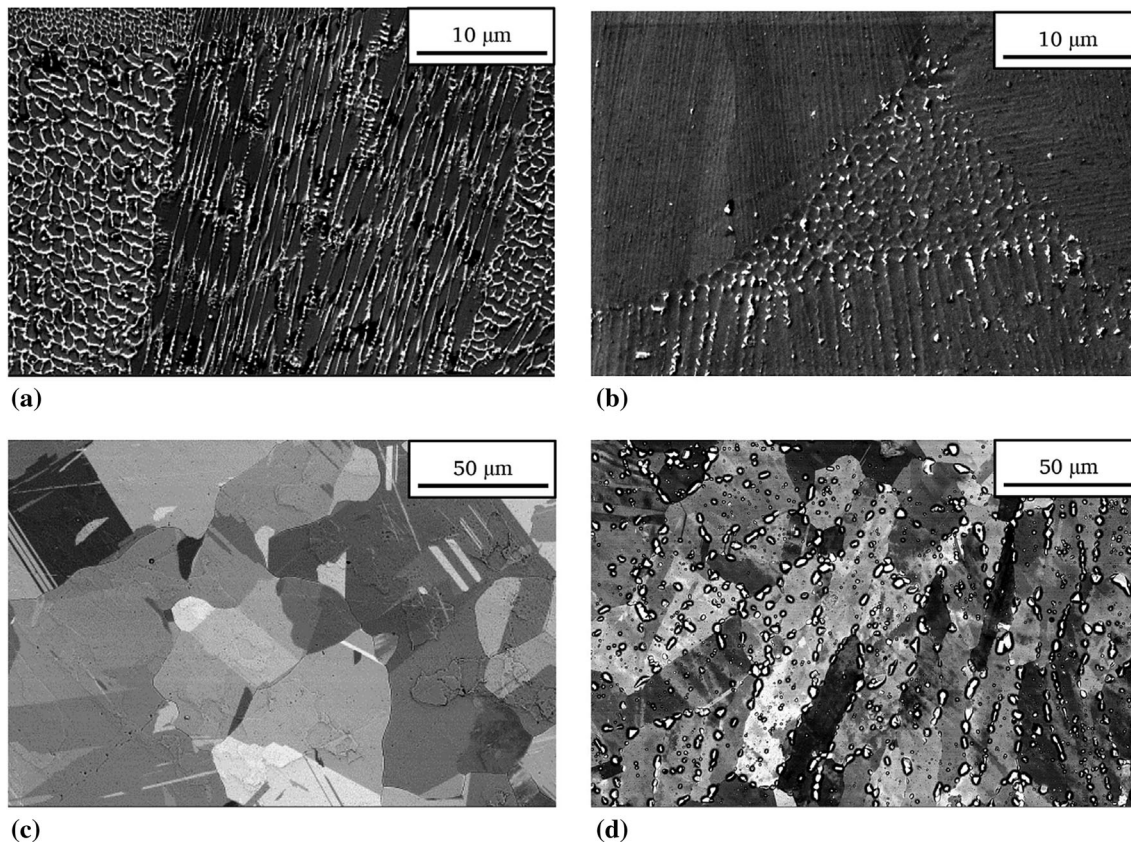
Fig. 10 Grain structure of Inconel 625 alloy specimen printed by SLM and LMD at annealed conditions of (a) 700 °C, (b) 900 °C, (c) 1100 °C (SLM), and (d) 1100 °C (LMD) for 1 h (Ref 68). Reprinted from Materials Science and Engineering: A, Vol 764, J. Nguejio, F. Szmytka, S. Hallais, A. Tanguy, S. Nardone, M. Godino Martinez, Comparison of microstructure features and mechanical properties for additive manufactured and wrought nickel alloys 625, Article 138,214, Copyright 2019, with permission from Elsevier

Defects like porosity and grain structure show little variation except for coarsening after STA treatment (Ref 137). Gallmeyer et al. performed solution annealing (1020 °C, 15 min, water quench), followed by aging (720 °C, 24 h) applied to IN 718 samples produced by L-PBF (Ref 79). Due to the precipitation of the strengthening γ' and γ'' phases, the treated sample had a yield strength, ultimate tensile strength, and elongation of 1245, 1640 MPa, and 16.6% separately, compared to 760, 1335 MPa, and 21.3% in the as-printed sample. Raza investigated the effect of solution treat, STA, and HIP on SLM-built IN718 plate (Ref 62). STA (954 °C, 1 h + 760 °C, 5 h + 649 °C, 1 h) increases the microhardness 470 HV compared to 300 HV of as-built condition, while solutionizing and HIP show little impact on the hardness. STA shows less susceptibility to crack than that of solution treating alone, while HIP samples exhibit similar crack susceptibility compared to wrought materials.

Stress relieved IN625 sample printed by SLM shows considerably higher UTS, YS, and fatigue crack propagation threshold values than those of as-built sample, but also causes strong microstructure anisotropy (Ref 138). Nguejio et al. prepared an IN625 alloy structure by SLM/LMD, and performed annealing at 700, 900 and 1100 °C in a furnace for 1 h followed by cooling in air (Ref 68). As shown in Fig. 10, annealing at temperature over 900 °C causes the recrystallization to transform the dendritic microstructure to equiaxed grains with annealing twins. However, annealing at 1100 °C for 1 h is not sufficient to form a fully homogeneous microstructure. The γ'' phase precipitated from the matrix (Fig. 10a) at 600 °C and

provided strengthening effects. Moreover, γ'' precipitates dissolved into the matrix when annealing over 900 °C. As a result, the yield strength, and elongation were 422, 495, 451, 230 MPa, and 10, 13, 14, 28% in the as-printed sample, respectively. When EBM-fabricated Ni-based superalloy DZ125 containing Hf is treated with HIP and STA, the unwanted size gradient in γ' columnar grains in the as-built condition can be eliminated (Ref 94). Nonetheless, the reappearance of intergranular cracks with a wide opening width after HIP + STA is caused by the effect of γ' dissolution and re-precipitation of fine γ' during the cooling stage of STA. Similarly, CM247LC is treated with thermal post-processing, in which the aging study shows that normal recovery is taken place when temperature is below 700 °C (Ref 215). Precipitation of γ' and carbides increases the creep resistance by suppressing the low-temperature creep mechanisms like the grain boundary sliding. Microcracking increases at high temperature (> 900 °C), which is driven by the high residual stresses from the rapid cooling. The low-temperature annealing (< 700 °C) leads to increased microcracking. In another CM247LC study, Divya et al. found that the large amount of fine intercellular and intracellular γ' precipitates and dislocations were coarsened and reduced, respectively, by partial recovery and recrystallization through annealing at 1230 °C for 2 h followed by air cool (Ref 77). A super-solvus solution at 1232 °C followed by two-step aging can achieve a long-term microstructural stability with no deleterious phase under 1000 h exposure at 871 °C on a new Ni-based superalloy

(Ref 95). However, a sub-solvus HIP + STA can generate a fully dense fine-grain microstructure with a bimodal distribution of γ' precipitates. Aging at 1000 °C and HIP both can enable strengthening of the γ' phase on Haynes 282 fabricated by SLM (Ref 106). A higher fraction of γ' phase leads to enhanced mechanical properties. Further aging shows no significant coarsening of the γ' grains. When HIP and STA are applied to CMSX-4, a holding time of 15 min at 1300 °C is sufficient to homogenize the alloy (Ref 201). A short aging for 2 h at 1140 °C and 4 h at 870 °C is sufficient to develop a fine γ/γ' microstructure with a unimodal γ'-precipitate size distribution. Two topologically close-packed phases (TCP), laves and Ta/Ti carbides, precipitate at the grain boundaries and at the edges of the specimens, respectively. When HX superalloy is treated by HIP + STA, HIP firstly dissolves the intergranular filament of carbides and to control the carbide re-precipitation as well as formation (Ref 93). A subsequent STA can dissolve the film of carbides at grain boundaries and form equiaxed grains. Such two-step heat treatment can tailor the microstructure of AM part of HX alloy for high-temperature applications.

FeCrCoMnNi HEA is heat-treated after printing through LMD to improve the tensile strength and ductility (Ref 72). When it is annealed above 700 °C, recrystallization occurs in the microstructure and meanwhile the microhardness decreases with increasing temperature. Furthermore, annealing at 1100 °C reduces the segregation and homogenizes the distribution of different elements in HEA. The EBSD and pole figure plots also indicate the promotion of grain growth, and residual stress is more relieved with increasing temperature. $Ni_{41}Al_{41}Cr_{12}Co_6$ alloy does not show significant improvement in mechanical properties and performance at elevated temperature after aging treatment alone (Ref 107). CoCrW alloy printed by SLM is solution treated for 1 h at 1150 and 1200 °C with water quench to fully dissolve the diamond-like pattern structure and precipitates at grain boundaries (Ref 204). Solutionizing at 1150 °C and furnace cool lead to a great number of large σ phase precipitations dispersed in grains and at grain boundaries. In contrast, solutionizing at 1100 °C with water quench shows fine $M_{23}C_6$ precipitations while solutionizing at 1150 and 1200 °C with water quench reveals fine-grain structure with point-like $M_{23}C_6$ precipitates and annealing twins, which represents the martensite transformation from γ-phase to ε-phase and results in slightly lower tensile strength (1160 to 1110 MPa) but much greater elongation to failure (10 to 20%) compared to as-printed specimens. A higher solutionizing temperature leads to a higher elongation value and a high cooling rate benefits the formation of ε martensite. Furnace cooling also increases UTS and YS more significantly than those of water quenched samples. When CoCrMoW alloy is stress relieved and further treated between 450 and 945 °C, the ε-Co (hcp) martensite phase is stabilized with coarsened grains and higher volume fraction (Ref 205). Thus, UTS and hardness are little affected while ductility is greatly degraded due to the coarsening of precipitates. Al0.5Cr-MoNbTa0.5 samples fabricated by EBM are treated at 1000 and 1300 °C (Ref 203). Homogenization treatment improves the microstructure but has little impact on the porosity. The study of WC-17Co MMC fabricated through SLM shows that annealing from 400 to 1000 °C with furnace decreases the amount of cracks and increases the hardness (Ref 216). With increased temperature above 600 °C it shows no significant improvement on hardness and fracture toughness. The WC phase is consumed at higher temperature and transforms to other brittle phases, resulting in lower wear resistance and toughness. In addition, HT at ambient atmosphere is applied to MMC of AlSi10Mg matrix with WC reinforcement to minimize the thermal and residual stress (Ref 208).

For steel, austenitic stainless steels are not typically heat-treated after fabrication. For example, the duplex stainless steel requires a post-build heat treatment to obtain the duplex structure and therefore to obtain the combinations of strength and stress corrosion cracking (SCC) resistance (Ref 217). When isothermal heat treatment is conducted in air at 400, 800, 600, and 1000 °C, recrystallization is found to be complete at 800 °C and meanwhile the hardness drops significantly (Ref 144). The grain size after annealing at 400 °C or 600 °C is slightly increased compared to that of the as-built sample. Further grain coarsening and reduced hardness are obtained after annealing at 1000 °C. Another isothermal study (500–1300 °C) on 316L stainless steel samples by SLM shows that high temperature (over 800 °C) diminishes the original cellular structure and prevents the formation of passive film, which causes a decrease in microhardness and open circuit potential due to recovery, recrystallization, and grain growth (Ref 158). When heat treating H13 tool steel printed by SLM, stress relieving and a microstructure of prior austenite, carbides, and ferrite result. The heat-treated steel exhibits lower strength and hardness but its elongation varies due to porosity (Ref 145). Hardening and tempering enable the formation of tempered martensite with fine, round, and randomly distributed carbides along martensite needle boundaries and therefore greatly increase the strength and hardness. Furthermore, HIP + hardening and tempering can achieve the highest strength and hardness, as well increase in elongation with lower scattering in values. When solution treating above 1100 °C is performed to a SLM-fabricated 316L SS sample, a substantial decrease of pitting corrosion resistance can be observed compared to its as-built condition (Ref 207). Such high temperature T4 transforms typical manganese silicate inclusions to manganese chromite inclusions and enables the formation of a considerable amount of MnS inclusions, which mainly causes the decrease of pitting corrosion resistance. However, another study of SLM-316L SS also reports that solution treating at 1200 °C for 4 h provides the best corrosion resistance with full austenitic microstructure (Ref 71). Subcritical annealing at 950 °C for 4 h on 316L SS can enable the transformation of cellular substructures from high-energy high-density dislocation wall to a low-energy subgrain boundary and therefore achieve the best corrosion resistance and mechanical properties (Ref 206). Higher temperature annealing triggers recrystallization and significantly reduces the low-angle grain boundaries (LAGB). For 4130 steel, long annealing treatment (10 h) causes abnormal grain growth, while annealing for 1 h on Ni foil (an interlayer for steel deposition using UAM) also leads to significant grain growth (Ref 218). Annealing at 727 °C for 10 h maximizes the shear strength, which decreases with lower annealing temperature. Longer annealing time also leads to reduced heterogeneity in the mechanical properties and higher energy absorption of the steel matrix from co-deforming of Ni-rich region. Yin et al. performed recrystallization annealing (by air and furnace at 1000 °C for 4 h separately) and HIP (1000 °C at 0.1 MPa, 4 h, and 150 MPa, 4 h) to a 316L stainless steel deposited by CSAM (Ref 183). Figure 11 shows that the porosity was reduced by annealing and eliminated after HIP. Due to recrystallization (the polygon grain shown in Fig. 11b and c) and elimination of dislocations, both annealed samples (~ 160 $HV_{0.5}$) and HIPed samples (~ 175 $HV_{0.5}$) had lower hardness
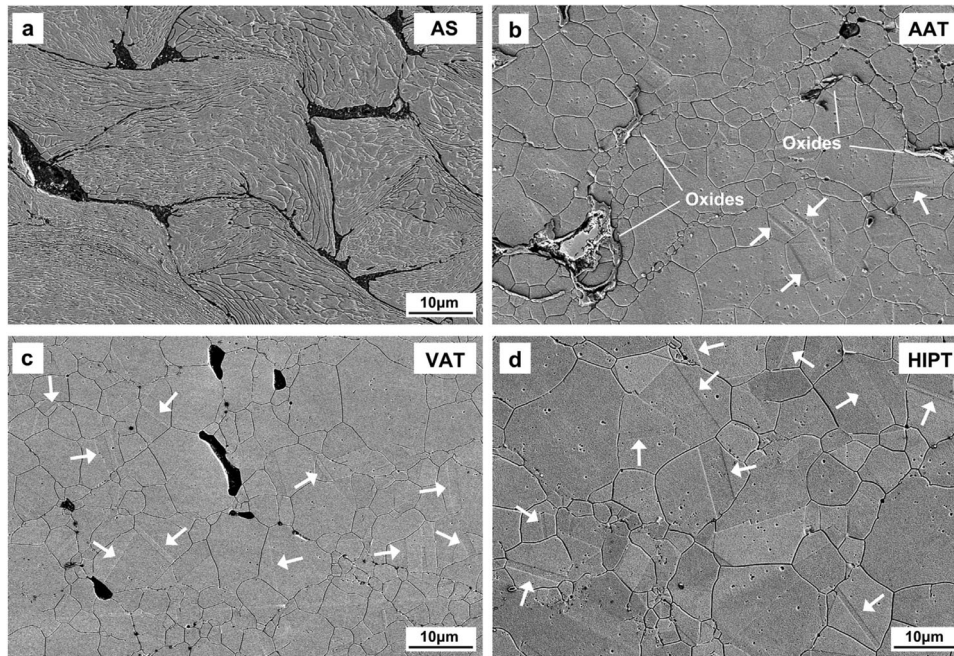
Fig. 11 Microstructure evolution of the 316L deposits before and after post-treatments: (a) as-fabricated, (b) air-annealed, (c) vacuum annealed and (d) HIP-treated. The formed annealing twins are marked by white arrows (Ref 183). Reprinted from Surface and Coatings Technology, Vol 370, Shuo Yin, Jan Cizek, Xingchen Yan, Rocco Lupoi, Annealing strategies for enhancing mechanical properties of additively manufactured 316L stainless steel deposited by cold spray, Pages 353-361, Copyright 2019, with permission from Elsevier

than the as-printed ones (250 HV$_{0.5}$). Nevertheless, due to the enhanced inter-particle bonding, increased ductility was achieved by 0.5, 17, and 13% with UTS of 39, 449 and 442 MPa for as-built, annealed, and HIP samples, respectively. Junker et al. applied age hardening and tempering to hot work tool steel X37CrMoV5-1 fabricated by SLM and concluded that both treatments have no significant impact on the Vickers hardness, while YS and UTS are greatly promoted especially after tempering from 800 and 1710 MPa to 1630 MPa (103% increased) and 2130 MPa (25% increased), respectively (Ref 184). In another work, SLM-built 24CrNiMo alloy steel was treated by tempering and annealing and exhibited decreased hardness (365-385 HV$_{0.5}$ to 310-330 HV$_{0.5}$), decreased yield strength (1053 to $\sim$ 1000 MPa), and increased elongation (10.7 to $\sim$ 12%) (Ref 75). The result also shows that the high-temperature friction and wear properties are considerably improved. Wang et al. investigated the effect of quenching and tempering treatment on 12CrNi2V alloy steel and found that its grain size is refined and the microhardness is improved (Ref 185). Tempering treatment alters the preferential orientation of the grains and increases the HAGB content, which leads to higher tensile properties and microhardness. Shi et al. reported that the normalization and subsequent tempering treatment decreased the tensile strength of LENS-deposited steel part due to the coarsening of quenched fine-grain martensite lath (Ref 219). However, such heat treatment also increased the plasticity and eliminated the anisotropy in tensile properties since new equiaxed austenite grains formed.

For aluminum alloys, the general effect of all these annealing treatments is to alter the distribution of Si-rich phases. Stress relieving results in eutectic Si particle coarsening and precipi-

tation of Si in the primary α-Al phase. It also decreases the UTS and increases the ductility. When stress relieved at 200 °C instead of 300 °C (standard T5) for 2 h, the SLM-printed AlSi10Mg specimen shows a 64% increase in YS due to the formation and dispersion of nanosized Si precipitates from the 200 °C supersaturated solution (Ref 128). T6 STA treatment, typically used for 6000-series Al alloys to develop additional strengthening, may improve the strength level of the HIP-material but also increase residual stress. T6 peak hardening has been designated as artificial aging at 160 °C for 6 h. The only other common artificial aging treatment is T7. T7 over-aging is specified as artificial aging at 205 °C for 3-6 h. Quench rate in the Al-Si systems is also critical, which includes forced air cool (by fan), near boiling water (95-100 °C), 100% ethylene glycol, and room temperature (20-25 °C) water. An increase in hardness directly correlates to an increasing quench rate (Ref 220). SLM-produced AlSi10Mg part is applied with two-step treatment of HIP and T6 STA (Ref 127). T6 treatment results in dissolution of the Si particles, precipitation, and coarsening to a large size ($\sim$ 4 μm) in the elongated Al grain structure with slight reduced hardness and tensile strength (Ref 129). After solution treating, homogeneity in microstructure can be achieved with refined grains while hardness is reduced, while the HIP causes much finer Si particles due to a solid solution temperature and slow cooling. The HIP + T6 specimens exhibit similar strength, elongation to failure, and toughness. In another case, T6 treatment not only eliminates the anisotropy but also increases the hardness with formation of Mg$_2$Si and Al$_5$FeSi precipitates (Ref 209). He et al. noticed that natural aging (T4) treatment increased the micro-hardness of AlZnMg alloy specimen fabricated by underwater friction stir AM from 85 to 105 HV$_{100g}$ (Ref 88). Natural aging

also improves the YS and UTS with no significant change on elongation.

3. Surface Treatment and Modification

In contrast to HTs that are effective in improving the bulk properties like modulus, strength and ductility of as-printed AM structures, surface treatment is used to mainly achieve a uniform surface finish or modify the surface properties. It provides a minimal surface roughness and certain degree of hardening on the surface to significantly improve the fatigue and corrosion resistance. The effects of major surface variables on the fatigue and corrosion resistance are summarized in Table 5.

Different applications of AM components require different criteria on degree of surface finish and tightness of part tolerance. The ultra-smooth finish on certain bearing application is expected to have a roughness R_a value lower than that of common mechanical application. On the other hand, biomedical applications generally demand a roughness R_a that benefits the osseointegration. However, surface roughness and geometric tolerances cannot be addressed by in-process control and needs optimal post-processing strategies. The adopted post-processing techniques can contribute to the variance of the surface roughness when uncontrollable parameters are presented (Ref 221). Conventional surface finish methods like machining and non-traditional approaches such as sand blasting, shot/laser peening, chemical etching, abrasive fluid machining (AFM), laser polishing/ablation, rotary ultrasonic machining (RUM), vibratory bowl abrasive finishing, electroplating, or micro machining process (MMP) can all achieve a low roughness Ra and increase fatigue life. Surface treatment, modification, and thermal post-processing can be applied in a designed sequence to relieve the residual stresses, enhance microstructure, promote the mechanical properties, and enable special functionality. For example, polishing alone to relieve the residual stresses at the near surface may be insufficient to heal the induced deeper internal stresses and part distortion.

Surface roughness is one of the most important features of intricate AM components. Surface roughness is measured using a profilometer or analyzing the surface morphology using SEM. On the surface the height of a peak or the depth of a valley (f_n) is measured at N locations along the profile length L. The average surface roughness (R_a) is numerically calculated as (Ref 222):

$$R_a = \frac{1}{N} \sum_{i=1}^{N} |f_n|. \tag{Eq 17}$$

The surface roughness caused by 'stair step effect' is due to the stepped approximation by layers of curved and inclined surfaces. A second mechanism for forming rough surfaces is improper melting of powder particles and balling phenomenon. The average surface roughness (R_a) depends on the layer thickness (t_l) and the build angle (h) and can be represented by the following equation (Ref 223):

$$R_a = 1000 t_l \sin\left(\frac{90 - \theta}{4}\right) \tan(90 - \theta), \tag{Eq 18}$$

where R_a is the arithmetic mean of the surface roughness of a region with a particular build angle. Surface roughness increases with the increase in layer thickness. Therefore, the common AM obstacle of balancing the tradeoff between intricacy and build time arises in the case of surface roughness.

The relationship between the geometry of the notch and the microstructure of the material can be described by the equation below (Ref 224, 225):

$$\sigma_i^{\text{nom}} = \frac{\sigma^{\text{app}}}{Z_i}, \tag{Eq 19}$$

where σ^{app} is the applied stress, σ_i^{nom} is the distribution of the nominal stress ahead of the notch root as a function of the distance from the notch i, mapped as $i = 2a/D$, and Z_i is the notch factor given by:

$$Z_i = \frac{\sqrt{i}}{\overline{\alpha} + \overline{\beta}} \left[\frac{\overline{\beta}}{\lambda_i} + \frac{\overline{\alpha}}{\sqrt{1 + \lambda_i^2}} \right]^{1/2}, \tag{Eq 20}$$

Table 5 Effects of sample surface variables on the corrosion and fatigue resistance

Variables of sample surface	Effects of the variable on fatigue resistance	Effects of the variable on corrosion resistance
Roughness	Higher roughness causes higher stress concentration and probability of crack initiation, therefore reducing fatigue resistance	Higher roughness, porosity and defects create more difficulty to form a protective oxide film and reduce corrosion resistance
Surface porosity and defects	Porosity and defects with higher density/number and sizes are potential sites for crack initiation, reducing the fatigue resistance	
Surface crystallinity	Higher surface crystallinity promotes crack propagation along preferential crystallographic directions, reducing fatigue resistance	Higher crystallinity results in better corrosion resistance due to reduced diffusion of water

$$\lambda_i = \frac{1}{\alpha^2 - \beta^2}\left[\alpha\sqrt{(\alpha + iD/2)^2 - \alpha^2 + \beta^2} - \beta(\alpha + iD/2)\right],$$

(Eq 21)

where $i = 1, 3, 5\ldots$ The parameters $\bar{\alpha} = 2\alpha/D$ and $\bar{\beta} = 2\beta/D$ represent the notch depth α and the notch half width β in a dimensionless form. The parameter D represents the distance between two successive barriers. In the case where grain boundaries are considered being the dominant barrier, D is regarded as the grain diameter. The elastic stress concentration factor, K_t, can be expressed as (Ref 226):

$$K_t = 1 + 2\sqrt{\frac{\alpha}{\rho}},$$

(Eq 22)

where ρ is the is the radius at the root of the notch. It indicates that a greater depth and a smaller root radius will lead to a higher value for K_t. Thus, a semi-empirical equation to relate the surface stress concentration factor with roughness parameters R_z is described below:

$$K_t = 1 + n\sqrt{\lambda\frac{R_z}{\rho}},$$

(Eq 23)

where R_z is the 10-point surface height, n is a constant that is equal to 1 for a mechanically processed surface, and λ is the ratio between the width and the height of the notch. The estimation of the intrinsic surface roughness of an additive manufactured metallic part and its corresponding effect on the mechanical behavior can be described mathematically by Eq. 17, 18, 19, 20, 21, 22 and 23.

AM processes also generate surface texture features on article that are undesirable or a specific feature of the surface structure that is required to be modified for functioning or performance. For instance, the goal of modifying the surface of a biomaterial is to create a specific chemical and physical environment that offers a favorable cellular response in hard or soft tissues (Ref 145). Surface modification by introducing texture change and residual compressive stresses within a thin outer layer has been shown to significantly enhance the mechanical properties of the part. The processed materials exhibit higher hardness, enhanced corrosion properties, cracking resistance, fatigue strength and lifetime, as well as extraordinary tribological properties. Surface engineering techniques consist of physical and chemical approaches. Shot peening, ultrasonic shot peening, laser shock peening, cavitation peening (CP), deep cold rolling, surface mechanical attrition treatment, ultrasonic impact treatment, and barrel finishing all physically modify the near-surface layers through severe plastic deformation (SPD) and accumulating energy on the surface. For example, introducing residual compressive stresses to the thin outer layer significantly enhances the mechanical properties of the part such as corrosion resistance, fatigue strength, and extraordinary tribological properties. These physical approaches also introduce microrelief in the near-surface and reduces surface roughness.

Chemical post-process methods are preferred for AM part due to their features such as improving the surface quality, promoting better dimensional and geometric stability, corrosion resistance, modifying the surface roughness, increasing abrasion resistance, and more (Ref 227). Chemical modification post-processes include plasma and chemical vapor deposition, atomic layer deposition, and electrochemical deposition, which result in oxidizing/nitriding/carburizing surface or incorporating elements that self-passivate (Ti, Cr, Al) to a surface to form surface functionalization, ion infusion, single layer coatings, or coatings comprising many layers of different compositions. There are other chemical post-treatments such as chemical etching, nanotube formation, chemical polishing, electrochemical polishing, and electroplating that promote the surface roughness and surface topography.

Abrasive finishing includes abrasive fluidized bed (AFB) (Ref 228), centrifugal finish (CF) (Ref 229), linishing (Lin) (Ref 229), tumble finish (TF) (Ref 230, 231), ultrasonic cavitation abrasive finishing (UCAF) (Ref 232), abrasive blasting (AB) (Ref 85, 221, 233-235), abrasive polishing (AP) (Ref 233), drag finish (DF) (Ref 236), vibratory finish (VF) (Ref 221, 236), and barrel finish (BF) (Ref 237). Table 6 gives a fundamental description and comparison among various surface treatments commonly adopted as post-process for AM-built metallic structures.

3.1 Traditional Surface Treating

Traditional surface treatments include milling, grinding, vibratory grinding, polishing, blasting with ceramic media, micro machining, etc. Due to the generally complex shape of the AM metallic structures, traditional mechanical treatments are not suitable for treating their surfaces. For example, it can be difficult for mechanical polishing and rolling to reach some corners and cavities of the structure, especially weak and thin structures (Ref 294). Traditional machining, firstly, could cause severe material waste and become inappropriate when tolerance is tightly met. Secondly, milling and grinding flatten and enhance the surface but induce tool marks and compressed residual stresses due to the deformation. It also has no capability of treating complex geometry and internal faces. In additional, traditional machining performs inefficiently on work hardening materials such as superalloys.

For flat or simple curved surfaces, finishing process typically uses a depth of cut less than 1.0 mm to decrease the roughness on the specimen surface. A common polishing process using microgrinder on titanium alloy Ti6Al4V, stainless steel 316L/17-4 PH, and cobalt chromium alloy shows that the surface roughness R_a of all the specimens reaches in the range of 0-2 μm (Ref 295, 296). Traditional machining and polishing are also used to treat the tensile specimen of bulk HEA (CrMnFeCoNi, Ni6Cr4WFe9Ti) fabricated by SLM (Ref 297, 298). Other studies reported that polishing to 1200 grit or more on Ti6Al4V sample can achieve a surface roughness ~ 0.2 μm in terms of R_a (Ref 114, 164). Bagehorn et al. reported that with simple milling the R_a value was reduced up to 98% to 0.3 μm for SLM-built Ti6Al4V (Ref 239). Tool machining can also achieve 0.2 μm of S_a for surface roughness (Ref 230). Conducting a fine abrasive finishing (FAF) on specimen of EBM-fabricated Ti6Al4V reduces the surface roughness even lower to an average value of 0.045 μm (Ref 299). Machining and fine abrasive finishing lead to 98.1 and 99.82% decreasing in surface roughness, respectively.

Finish machining (FM), drag finishing (DF), and vibratory surface finish (VSF) are applied to enhance the surface of the specimen in SLM Inconel 718 alloy (Ref 236). FM is conventional turning operation with specific operational parameter setting. DF uses a media of Kaolin and alumina to straight cut with F-triangle. In VSF operation, brown fused alumina is

Table 6 Description of typical surface treatments for post-process AM metallic structures

Surface treatments	Roughness R_a, μm	Internal face	Surface composition	Note
Machining, grinding, polishing (Ref 230, 234, 236, 238-240)	~ 0.1	No	Little impurities	…
Shot peening (SP) (Ref 59, 76, 85, 212, 230, 234, 238, 240-243)	< 4.0, up to 60% reduced	No	No impurities	Significantly improved fatigue properties, hardness, and surface compressive stress
Laser shock peening (LSP) (Ref 238, 244-251)	< 3.0	No	No impurities	Improved high-temperature oxidation resistance
Laser polishing (LP) (Ref 86, 228, 252-259)	~ 0.1, up to 99% reduced	No	No impurities	Improved fatigue properties and hardness
Chemical polishing (CP) (Ref 260–262)	< 0.5, up to 92% reduced	Yes	No impurities, create passivate layer	No significant impact on fatigue properties; preferential dissolution element; reduced modulus and surface compressive strength
Chemical etching (CHE) (Ref 235, 263-266)	< 6.0	Yes	No impurities, removal of oxide layer	Increased stiffness-to-density ratio, no significant impact on fatigue and tensile properties
Electrochemical polishing (ECP) (Ref 235, 240, 262, 264, 266-278])	~ 0.01, up to 98% reduced	Yes	No impurities, create passivate layer	Reduced modulus, hardness; improved fatigue properties, UTS, elongation, corrosion resistance; more effective on external features
Electrospark deposition (ESD) (Ref 202, 279)	< 2.0, up to 82% reduced	Yes	Target material	Reduced near-surface porosity, form intermetallic coating
Sputtering (Ref 280, 281)	< 10.0	Yes	Target material	Improved modulus, hardness, wear resistance, tribological properties
Hot working (Ref 69, 136, 282)	…	No	Little impurities	Improved YS, UTS, and elongation
Ultrasonic nanocrystal surface modification (UNSM) (Ref 283-286])	< 0.06, up to 88% reduced	No	Little impurities	Improved fatigue, corrosion, wear resistance, and compressive stress, reduced friction condition
Friction stir processing (FSP) (Ref 87, 287-293)	< 0.03	No	No impurities	Achieve ductilization with nanoscaled equiaxed grains and high-angle grain boundaries (HAGB)
Abrasive finish (Ref 85, 228-237)	2.0–20.0	Yes	Little impurities	Improved fatigue properties and hardness

used for cutting. As a baseline, the average roughness of as-built SLM Inconel 718 ranges from 19 to 24 μm. FM, DF, and VSF result in reduction of surface roughness up to 96, 73, and 88%, and they promote the hardness by 21, 10, and 10%, respectively. DF and FM also decrease the wear rate with 7 and 12%, respectively. The milling finishing of dry cutting on SLM Inconel 625 not only improves the surface quality but also greatly reduces the wear rate (~ 50%) (Ref 300).
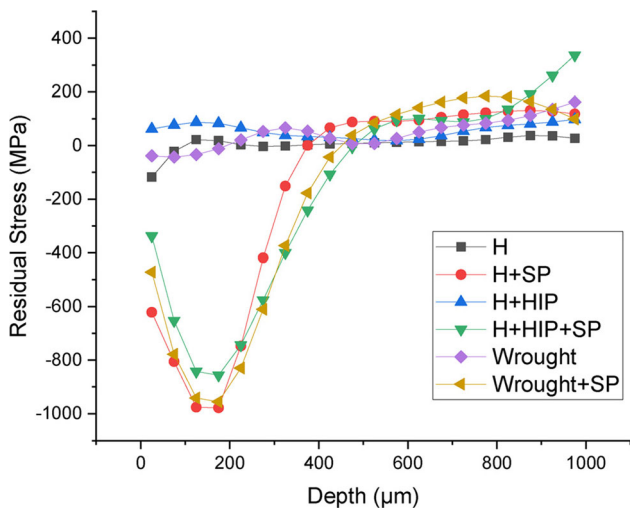
3.2 Peening

Peening is a process that plastically compresses material normal to a surface and results in transverse expansion and furthermore a local build-up of compressive stress. Peening

techniques includes shot, laser, ultrasonic peening, etc. The investigation by Soyama et al. revealed that cavitation peening, shot peening, and laser peening were all capable of reducing the surface roughness and promoting the fatigue strength (Ref 238). The improved fatigue strength after mechanical surface treatment such as peening can be estimated:

$$\sigma_f' = \sigma_f + a\frac{1}{\Delta R_z}\sigma_f + b\Delta H_{R15N}\sigma_f + c\Delta\sigma_R \qquad \text{(Eq 24)}$$

$$\Delta R_z = (R_z - R_z')/R_z, \qquad \text{(Eq 25)}$$

$$\Delta H_{R15N} = (H_{R15N} - H_{R15N}')/H_{R15N}, \qquad \text{(Eq 26)}$$

Fig. 12 The distribution of residual stress along the depth of wrought and SLM-produced IN718 with treatment of STA (H), HIP, and shot peening (SP) (Ref 168). Reprinted from Additive Manufacturing, Vol 36, Dennise Tanoko Ardi, Lim Guowei, Niroj Maharjan, Bisma Mutiargo, Seng Hwee Leng, Raghavan Srinivasan, Effects of post-processing route on fatigue performance of laserpowder bed fusion Inconel 718, Article 101,442, Copyright 2020, with permission from Elsevier

$$\Delta\sigma_R = (\sigma_R - \sigma_R')/\sigma_R, \qquad \text{(Eq 27)}$$

where σ_f is the fatigue strength of the reference condition, R_z is the surface roughness, H_{R15N} is the surface hardness measured at an applied load of 15 kgf, σ_R is surface residual stress, X' is the difference of the property between the reference condition and the estimated condition. Equation 24, 25, 26 and 27 describe the relationship between surface roughness, hardness, and strength and are used to evaluate the fatigue performance based on surface condition of the metallic structure.

3.2.1 Shot Peening (SP). Shot peening allows a specimen to be treated with high-speed bombardment (small, spherical, hard particles of metallic, glass, or ceramic) on the surface. The impaction of these particles with sufficient velocities creates plastic deformation with little heat generated. It requires multiple impacts for 100% coverage due to the spherical nature of the impacts. The shot generates transverse and normal forces and increases the hardness. Shot peening can generate a compressive stressed layer of up to 400 μm on the surface of IN718 article fabricated by SLM (Ref 168). Figure 12 demonstrates the distribution of compressive stress generated by shot peening on wrought and treated SLM-produced IN718 components.

When shot peening with steel balls (S110, utilizing an Almen intensity of I = 5''A) or ceramic balls (Z210, utilizing an Almen intensity of I = 12.2''N) were applied on SLM-built AlSi10Mg samples, the nanohardness distribution along the depth of the sample surface shows little difference (Ref 240). Sawicki et al. conducted a study involving two-stage shot peening treatment with steel and glass beads on an Al alloy (AlMg5Mn1Sc0.8Zr0.4) (Ref 241). The duplex peening can further reduce the roughness R_a by 50% compared to single steel peening. Abrasive blasting, shot peening, and mechanical polishing are examined for their effect on surface texture and tribological behavior of AlSi10Mg alloy samples fabricated by

SLM (Ref 234). The surface roughness R_a reduces from an as-built status to 18.71, 5.39 and 1.39 μm after shot blasting, shot peening, and polishing, respectively. Jebaraj et al. performed shot peening to a AISI 316L stainless steel sample produced by direct laser sintering, and the corrosion current dropped from 0.29 to 0.10 mA/cm^2 (Ref 301).

Shot peening is an effective approach in improving the fatigue strengths of AM-fabricated metallic structures, i.e., Ti-6Al-4 V, due to the introduction of a compressive residual stress layer (Ref 302). The effects of shot peening on fatigue performance were found to be strongly dependent on the microstructure as well as defects within the alloy prior to shot peening. Shot peening after STA significantly improves the fatigue life while HIP has negligible impact on fatigue behavior on STA samples. Denti et al. applied tool machining, tumble treatment (TB), and tumble + shot peening (TB + SP) to improve the surface finish for SLM-built Ti6Al4V alloy (Ref 230). The resulting surface roughness S_a is measured as 21.5, 18.9, and 4.83 μm for as-built, TB, and TB + SP conditions, respectively. Therefore, the TB-treated samples show a similar fatigue life compared to as-built one (2.4-2.6 $\times$ 10^4 cycles at maximum stress of 400 MPa). While the TB + SP treatment promotes the fatigue life to 1.5 times greater than that of as-built condition (2.4 $\times$ 10^4 cycles at maximum stress of 600 MPa). Uzan et al. reduced the surface roughness of a SLM-fabricated AlSi10Mg sample from 30 to 4.6 μm by shot peening, which greatly increased the fatigue limit from 50 to 110 MPa at a 10^7 cycle. Bagherifard et al. compared the sand blasting (SB) and SP treatments on SLM AlSi10Mg and found that both greatly increased the fatigue strength from 50 MPa of as-built to 173 and 185 MPa, respectively (Ref 85). When treated after T6 STA, both SB and SP showed reduced fatigue performance, especially for SP (102 MPa of fatigue strength). Damon et al. applied SP with S170 steel (0.4 mm, HRC 56, 0.1 MPa, Almen intensity = 0.2) to enhance SLM-built AlSi10Mg specimen (Ref 243). The SP treatment reduced the overall porosity by 0.1-0.3% in the surface area with up to 500 μm depth and promoted the fatigue strength at 10^7 cycles from 60 to 80 MPa (33.3% increase). Surface mechanical attrition treatment (SMAT), which is a peening-like system adopting steel balls driven by sonotrode, is used to impact the surface for inducing SPD. Portellar et al. concluded that SMAT can achieve a surface roughness to < 0.1μm with up to 94% of reduction and promote the microhardness to > 330HV$_{0.025}$ with up to 45% increase (Ref 303). Both YS ad UTS were improved from 527 to 624 MPa and 611 to 676 MPa, respectively, while the elongation was reduced from 29 to 16%.

Shot peening (SP), ultrasonic shot peening, barrel finishing, ultrasonic impact treatment are used to evaluate the surface improvement for SLM-fabricated IN718 turbine blade test parts (Ref 237). The barrel finishing (BF) is conducted in a rotating system consisted of a hexagon barrel, metal or ceramic shot media, and motor. In the process, the specimen surface is impacted continuously by the numerous high-speed collisions of the spherical shots with accumulated impact energy and plastic deformation. The USP (ultrasonic shot peening) utilizes the mechanical ultrasonic vibrations to bombard particles to generate severe plastic deformation on the surface of the specimen. Ultrasonic impact treatment (UIT) applies severe plastic deformation to the near-surface layers through impact loading from ultrasonic vibration of multi-pin head. Pins acquire their kinetic energy from the ultrasonic horn tip and produce impacts by the treated surface providing the normal
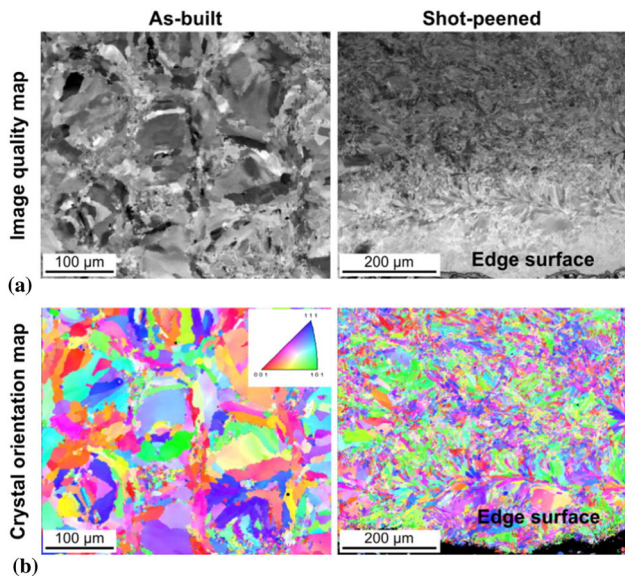
Fig. 13 EBSD plot of 17-4 stainless steel specimen fabricated by DMLS process in the as-built and shot-peened conditions (Ref 304). Reprinted from Materials & Design, Vol 110, Bandar AlMangour, Jenn-Ming Yang, Improving the surface quality and mechanical properties by shot-peening of 17-4 stainless steel fabricated by additive manufacturing, Pages 914-924, Copyright 2016, with permission from Elsevier

(vertical) component of load. The BF, USP, and UIT processes reduce the surface roughness (S_a) from 5.27 μm of the as-built status to 79.4, 73.8 and 42.6% of the current S_a. The residual porosity level is decreased by 23.1, 40.6, 55 and 84% of the as-built level (0.697%) after the BF, SP, USP, and UIT processes, respectively. BF, USP, UIT, and SP promote the surface microhardness by 14.2, 23.8, 50, and 66.5% of as-built hardness (390 HV). They also alter the tensile stresses on the surface of the as-built specimen (+ 120 MPa) to compressive stresses as $-$ 201.4 MPa (BF), $-$510.7 MPa (SP), $-$ 313.8 MPa (USP), and $-$ 428.7 MPa (UIT).

A combination of aluminum oxide and glass beads are utilized in shot peening post-process to improve the surface of the 17-4 stainless steel article printed by SLM (Ref 304). SP achieves a reduction of $\sim$ 70% on the S_a value (1.2 μm) compared to that measured before SP (4.0 μm). In addition, SP induces an austenite-to-martensite transformation and grain refinement in the treated samples due to plastic deformation (Fig. 13). Refined grain structure ($\sim$ 50% lower in crystalline size) is caused by work hardening during SP. After the peening process, the specimen exhibits a residual compressive stress of $\sim$ 700 $\pm$ 3 MPa in contrast to the as-built sample with a residual stress of $\sim$ 119 $\pm$ 18 MPa. The plastic deformation is regionally inhomogeneous, indicating that repeated mechanical loads on the material surface are statistically concentrated in certain directions. The region consists of fine grains with high dislocation densities as well as random directions, and hence the area has a very low lattice strain. The exchange of intrinsic stress might also promote the transformation from subgrains to finer structures. Furthermore, grain refinement could result from the shear deformation induced by localized concentrated stress. The SP layer consists of a mixture of ultrafine grains (20-200 nm) along with sub-micrometer grains. The yield strength of the shot-peened specimen is notably increased by $\sim$ 40%

relative to that of the as-built sample, which is because of the high dislocation density, grain refinement induced by SP (Hall–Petch relation), and the strong and fine-structured surface layers. The wear performance of the shot-peened parts is significantly enhanced through the improved grain refinement effect and the formation of fine-structured surface layers, stronger surface layer, lower surface roughness, and higher microhardness.

3.2.2 Laser Shock Peening (LSP). Laser shock peening (LSP) is known for inducing compressive stress to the subsurface of a material and creating transverse compressive stress field as well as small amounts of cold work (3-5%) with little change on the bulk properties of the treated material (Ref 244). The depth of LSP-induced compressive stress can reach to approximately 1 mm of the treated surface, which is one order of magnitude higher compared to that induced by SP. Curvature and stretch can be achieved on heavy section after the treatment of plastic straining. In the LSP process, short intensive laser pulses strain the material, create a plasma on the surface of the specimen, insert dislocations deep into the material, generate pressure pulses that create local plastic deformation, strain hardening, and deep compressive stresses (Fig. 14a). The plasma pulse propagates as a compressive stress wave inducing cold working into the surface of the component. Typical LSP requires aluminum or iron foils to protect the workpiece from thermal effect. LSP without coating (LPwC) has been developed to better serve applications for maintenance. Karthik et al. summarized the surface roughness and compressive residual stress after LPwC treatment for various alloys (Ref 305). The increase in fatigue strength and fatigue life, as well as the decrease in corrosion current are all reported. New derivatives of LSP have been developed and adopted in applications and studies, such as warm LSP (WLSP), cryogenic LSP (CLSP), femtosecond LSP (FLSP), and also hybrid-techniques like electropulsing-assisted LSP (EP-LSP). More details of the mechanism of LSP and the effect of LSP on mechanical properties on materials such as ceramics and metallic glasses can be obtained from the recent review work by Zhang et al. (Ref 306).

LSP can generate 100% coverage with multiple impacts per beam spot. Laser-peened materials resist crack initiation and growth and typically demonstrate higher cracking and corrosion resistance thereby supporting enhancement in fatigue strength and lifetime of treated components. LSP enables higher levels of tensile fatigue loading before the fatigue limit is reached. The whole process can be engineered precisely in a spot-by-spot manner. When LSP is applied strategically to localized high stress areas, a deep level of plastic deformation provides superior fatigue enhancement. LSP imparts a deeper level of residual stress as it produces little cold work and thus minimally changes material hardness and yield strength. LSP would be especially beneficial for applications where geometry requirements create areas of increased stress such as in fillets and notched areas leading to local stress risers. Generally, the plasma at elevated temperature is generated by the confined area at the sample surface. Thus, the induced shock wave propagates into the sample within the constrained layer. The peak pressure P can be written as (Ref 294, 307):

$$P = 0.01 \sqrt{\frac{\alpha}{2\alpha + 3}} \sqrt{ZI_0}, \tag{Eq 28}$$
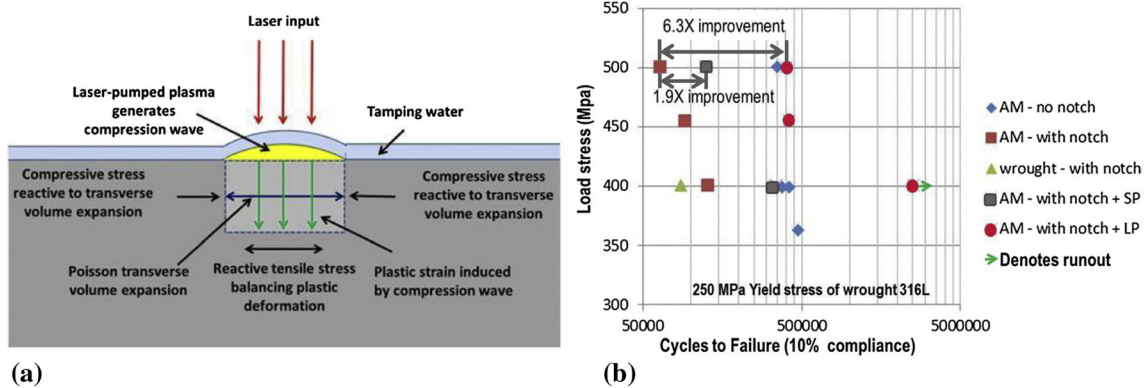
Fig. 14 Laser peening: (a) schematic view of peening mechanism and stress distribution, (b) fatigue lifetime test result vs. stress loading for AM 316 L stainless steel (Ref 244). Reproduced from Additive Manufacturing under the CC BY 4.0 license

where P is laser-induced pressure in GPa, Z is the reduced shock impedance between sample and confinement layer in $gcm^2 s^{-1}$; and α is the efficiency of the interaction, which represents the constant fraction of the internal energy as thermal energy. Since strain rates exceed more than 10^6 s^{-1} within the target material in LSP, Hugoniot elastic limit (HEL) model can be adopted to describe the dynamic yield strength under uniaxial strain condition assuming that yielding occurs when the stress in the direction of the wave propagation reaches the HEL with Poisson ratio v (Ref 308, 309). Thus, the dynamic yield strength under uniaxial strain condition was defined by Braisted and Brockman (Ref 310):

$$\sigma_{dyn} = HEL \frac{1-2v}{1-v}. \tag{Eq 29}$$

The load stress σ_L applied to the material can be described with strain ε_L (Ref 311):

$$\sigma_L = \begin{cases} (K + \frac{4}{3}G)\varepsilon_L, \sigma_L \leq \frac{1-v}{1-2v}\sigma_{dyn} \\ K\varepsilon_L + \frac{2}{3}\sigma_{YS}, \sigma_L \geq \frac{1-v}{1-2v}\sigma_{dyn} \end{cases}, \tag{Eq 30}$$

where K is the material bulk modulus and G is the material shear modulus. Equation 28, 29 and 30 evaluate the pressure and stress induced by laser on a material.

LSP was first studied by Fairand et al. on the enhancement of tensile properties for 7075 aluminum coupled with solutionizing, T73, and T6 (Ref 312). Hackel et al. compared the effects induced by SP and LSP. They found that at a stress loading of 501 MPa, the cycles to failure of AM 316 L stainless steel samples with notch increased by 1.9 times by SP while 6.3 times by LSP (Fig. 14b) (Ref 244). The higher effectiveness of the LSP is attributed to its development of more plastic deformation against localized high stress areas. Lu et al. studied the LSP treatment through FEM simulation and experiment on 316L stainless steel (Ref 294). The hardness distribution along the depth of the specimen surface shows that approximate 20% of increase is induced by LSP (1 Hz, 1064 nm, 20 ns, 3-mm spot size, 50% overlapping rate, pulse energy 7 J) within the depth of 2.0 mm. The yield strength has an increase of 16% after LSP (400 to 460 MPa) while little change is observed for tensile strength and elongation. Chen et al. applied LSP up to 3 times of impacts to SLM-built TiC/IN625 nanocomposite material (Ref 245). LSP reduces the porosity from 1.71% in the as-built specimen to 0.12% after treatment and increases the microhardness from 405 to 462 HV. In high-temperature oxidation test, the mass gain per

unit area of the treated sample is 2.61 mg/cm^2 compared to 7.23 mg/cm^2 of as-built one, which is due to the high magnitude of residual stress, formation of dense continuous layer of Cr_2O_3 and $Ni(Cr, Fe)_2O_4$ spinel, and the cellular grain structure with high-density of dislocations. Jin et al. studied the effect of LSP on Ti6Al4V samples produced by EBM using a Nd:YAG laser (1064 nm, 1 Hz, 25% overlapping rate, 11.89 $GW \cdot cm^{-2}$) (Ref 247). LSP increased the hardness from 315 to 355 HV (11% increase up to 900 μm under surface) and the fatigue strength from 600 to 700 MPa at 2×10^7 cycles (16% increase). Lan et al. also employed LSP to treat EBM Ti6Al4V to analyze the microstructure evolution (Ref 250). Before LSP, the microstructure consists of the α and β lamellar structure (Fig. 25a) with tensile stress (45 MPa) on the surface layer. After LSP, α lamella was refined as nanoequiaxed, nanodeformation twins and submicroequiaxed grains (Fig. 25d) with residual compressive stress (-380 MPa) on the surface layer.

Nalla adopted both deep rolling and LSP to enhance the Ti6Al4V specimen and reports that deep rolling is more effective on generating compressive residual stress as well as improving the HCF/LCF fatigue strength with higher work hardening at both ambient and elevated temperature (Ref 313). Jinoop conducted a parametric study of LSP on IN718 (Ref 251). The microhardness and affected depth both increased with increasing number of shots and laser power, while the wear rate decreases with increase in laser power and number of shots. Kalentics et al. also investigated the LSP treatment on SLM Ti6Al4V and found that the distortion was partly healed by LSP (Ref 248). Based on the works done, Kalentics' group submitted the patent on a hybrid additive manufacturing process which combines LSP and SLM. They also concluded that LSP enhanced the microhardness up to 35% (290 to 390 HV) on an austenitic, nickel-chromium stainless steel (Ref 249). The following annealing substantially increased the recrystallization rate in the LSP affected zone and thereby achieving a finer equiaxed structure after LSP + annealing. Chi et al. investigated the effect of combining annealing and LSP treatment employed to enhance the Ti17 alloy fabricated by WAAM (Ref 246). Although annealing coarsened the as-built grain structure, the subsequent LSP induced the grain refinement with high density of dislocation and twins caused by severe plastic deformation. After HT and LSP, the surface compressive residual stress reached to -600 MPa, while the microhardness increased from 410 to 460 HV (Fig. 15). The YS, UTS, and elongation were all improved after the HT + LSP treatment. When LSP was applied to Al-Zn-Mg-Cu after solution treatment and re-aging, both the depth and
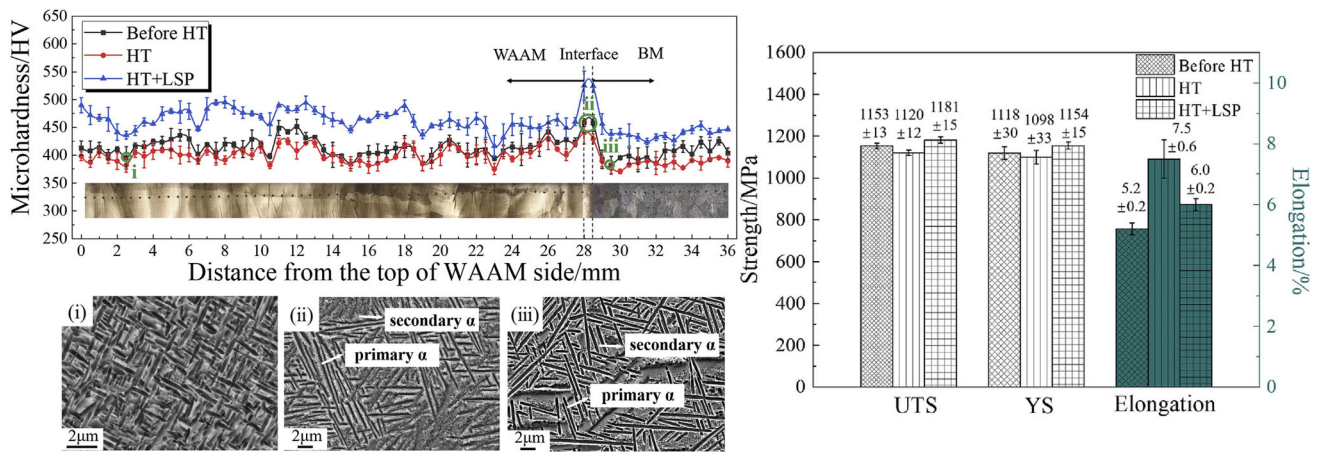
Fig. 15 Microhardness profile and corresponding microstructure as well as tensile properties of WAAM Ti17 specimen with base material (BM), post-treatments of HT (annealing 600 °C, 4 h, vacuum, furnace cool), and LSP (1064 nm, 15 ns, 20 J, 4 mm spot size) (Ref 246). Reprinted from Surface and Coatings Technology, Vol 396, Jiaxuan Chi, Zhongyi Cai, Zhandong Wan, Hongqiang Zhang, Zhenlin Chen, Liuhe Li, Ying Li, Peng Peng, Wei Guo, Effects of heat treatment combined with laser shock peening on wire and arc additive manufactured Ti17 titanium alloy: Microstructures, residual stress and mechanical properties, Article 125,908, Copyright 2020, with permission from Elsevier

coverage of the corrosion pits in chloride solution, as well as the depth of intergranular corrosion and the width of the intergranular cracks were all reduced for treated ultra-high strength Al-Zn-Mg-Cu alloy part. LSP introduced dislocations, stacking faults, slip lines and subgrain boundaries as sites that enabled the formation of continuous passive film.

3.2.3 Cavitation Peening. High-pressure water stream can be applied to treat the surface of AM part (Ref 314). When a waterjet impacts a material surface, it causes either cutting of the target material or plastic deformation in the deep surface layer. Above a certain impact stress threshold, the impact process induces compressive residual stresses which improve fatigue life. Cavitation peening results in improved microhardness compared to dry shot peening. It can be highly beneficial as AM parts are typically complex with narrow internal and external features which are easy to access with pure waterjets. A cavitating jet is normally produced by the flow of a water jet into a water-filled chamber. The advantages of waterjet-prepared surfaces are: higher bond strength, possible adjustable surface finish, no dust, possibility for automation and scaling up, surface cleaning, and accessibility to tight area. Unlike grit blasting which results in the entrapment of particles, waterjet profiling cleans the surface. It is hypothesized that waterjet roughening produces a favorable surface morphology for bonding because it creates undercuts which help locking in the coating. Ultra-high pressures (UHP) waterjet cutting and derivatives of waterjet-air jet (WAJ), abrasive waterjet (AWJ), and abrasive slurry jets (ASJ) are all potential techniques that can be used for support removal and surface finishing (Ref 315).

3.2.4 Ultrasonic Nanocrystal Surface Modification (UNSM). UNSM utilizes low-amplitude ultrasonic frequency vibrations to strike a tungsten carbide ball and scan over the surface of the specimen to induce high strain rate plastic deformation to improve the mechanical properties, enhances the resistance to fatigue, corrosion, as well as abrasion/contact failures by introducing residual stresses on the surface layer. The impact of ultrasonic vibrations induces surface severe plastic deformation (S^2PD) and refines the structure.

Kim et al. treated the LMD-built ANSI M4 tool steel specimen with UNSM and found that the hardness was improved 25%

from $\sim$ 780 to $\sim$ 920 HV due to the formation of martensite phase (Ref 283). The UNSM treatment can also reduce the surface roughness R_a from 0.5 to 0.06 μm with an 88% reduction. It also enables of significant enhancement on wear resistance (85% reduction on wear rate). With a vibration frequency of 20 kHz, a static load 10 N, and scanning speed 2400 mm/minute, UNSM can reduce the surface roughness R_a of the AlSi10Mg alloy from 18 to 3.5 μm (Ref 284). Applying similar UNSM treatment to NiTi alloy can only reduce the R_a from 12.1 to 9.0 μm, while a hardened layer of 125 μm was formed with 34.2% increasing in hardness from 304 to 408 HV (Ref 285). In addition, the improvement in corrosion and wear resistance can be observed in Fig. 16. Ultrasonic burnishing (UB), similar to UNSM, is an automated finishing technique that generates local plastic deformation using a spindle head and a wolfram-carbide ball with lubricant. Ultrasonic burnishing reduces the average surface roughness R_a of CoCr alloy and 316L SS specimen to 0.18 and 0.55 μm, respectively (Ref 316). Meanwhile, the average hardness of CoCr alloy and 316L SS has an increase of 47.4% to 551.07 HV and 70.7% to 338.17 HV, respectively. The improvement made by ultrasonic burnishing on surface roughness and hardness is better than those of a typical milling process. Zhang et al. applied a direct current during the UNSM to enhance the surface of SLM-built Ti6Al4V sample (Ref 317). With the assist of electrical current, the sample is held at 426 °C when treating with UNSM under a static load of 30 N, an ultrasonic vibration amplitude of 24 μm, a frequency of 20 kHz, a scanning speed of 2000 mm/minute. After the treatment, the surface roughness R_a reduced from 10.6 to 1.3 μm, while the hardness increased from 360 to 485 HV. Zhang et al. reported a surface pore reduction and a decrease in the surface roughness R_a from 10.6 μm to 5.9 μm for DMLS-prepared Ti6Al4V alloy part after UNSM treatment (Ref 318). With the increased microhardness (372.4 to 422.3 HV) and compressive residual stress, the fatigue behavior of treated specimen in rotary bending test was improved with an increase in cycle number to failure from 2×10^5 to 6×10^5 at 250 MPa.
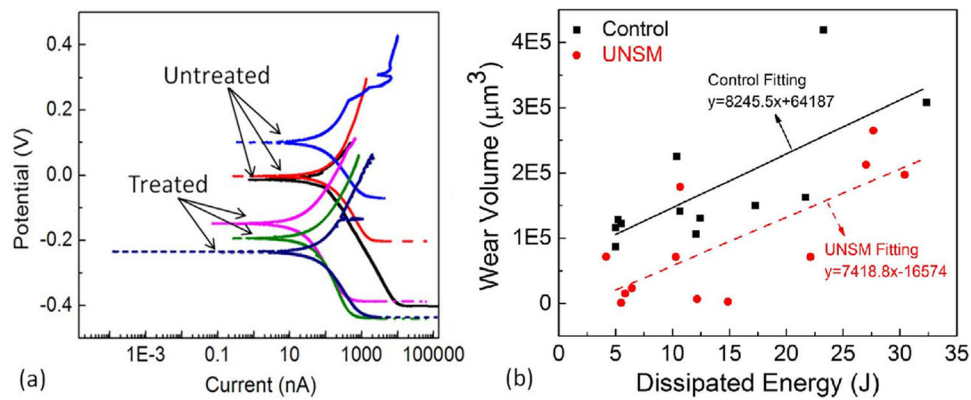
Fig. 16 Comparison of untreated and UNSM-treated SLM-built NiTi alloy specimen for (a) potentiodynamic polarization curves obtained in 3.5 wt.% NaCl solution for 1 h and (b) the wear volume at different dissipated energy (Ref 285). Reprinted from Journal of Materials Processing Technology, Vol 249, Chi Ma, Mohsen Taheri Andani, Haifeng Qin, Narges Shayesteh Moghaddam, Hamdy Ibrahim, Ahmadreza Jahadakbar, Amirhesam Amerinatanzi, Zhencheng Ren, Hao Zhang, Gary L. Doll, Yalin Dong, Mohammad Elahinia, Chang Ye, Improving surface finish and wear resistance of additive manufactured nickel-titanium by ultrasonic nanocrystal surface modification, Pages 433-440, Copyright 2017, with permission from Elsevier
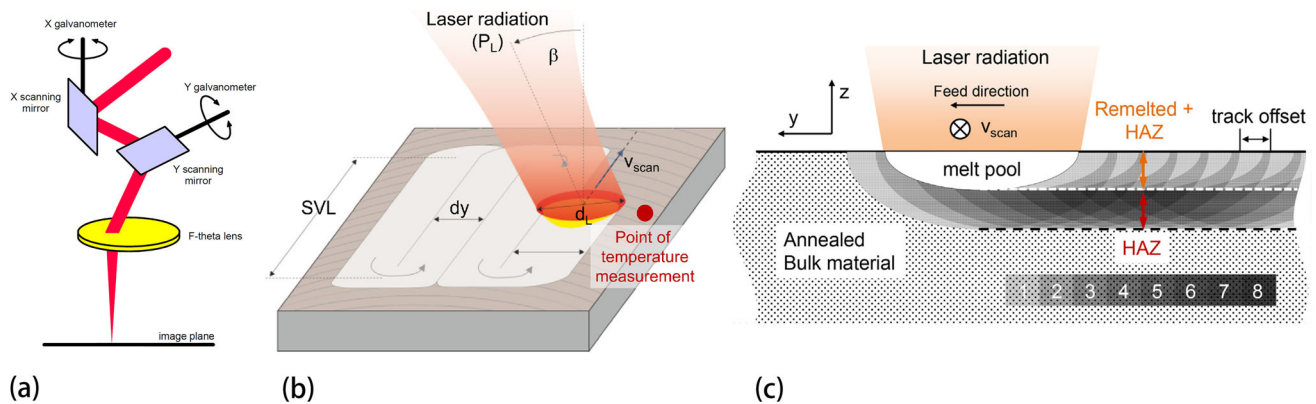

Fig. 17 Schematic diagram of laser scanning system, scanning pattern with key process parameters of average laser power P_L, laser beam diameter d_L, scanning velocity v_{scan}, scan vector length SVL, inclination angle β, and overlapping of HAZ (shades of gray represent the number of heat cycles) (Ref 319, 320). Reproduced from (a) Materials and (b,c) Materials & Design under the CC BY 4.0 license

3.3 Laser Surface Modification

Laser surface modification (LSM) is an applicable and flexible approach to improve the surface through means of scanning optics. Schematic diagrams of the laser scanning system, laser radiation and its interaction with the material under protective atmosphere, as well as the scanning pattern with key process parameters are shown in Fig. 17. The most common solid-state laser used in the industry is the neodymium-doped yttrium aluminum-garnet, or Nd:YAG. Copper vapor lasers and excimer lasers have also found wide use in materials processing applications. Copper vapor lasers have also proven their use in high accuracy micromachining, which have excellent beam quality and can usually produce a diffraction-limited spot on the substrate with only simple external beam steering optics. Nevertheless, copper vapor lasers have a shorter service life and require more maintenance than Nd: YAG lasers. Two different operation modes, continuous wave emission and pulsed radiation, can be used for laser polishing. Laser treatments can also be designated into different terminologies including laser polishing, laser micromachining, laser machining, etc.

LSM is different from laser peening which utilizes a compressive wave. It directly melts the top layer of the metal surface at the peaks and the relocation during the liquid phase to the valleys. Any un-melted metal particles on the surface are also melted and re-flow into surface valley areas. Beam wobbling in a prolate trochoid decreases the overall processing time on the polishing surface (Ref 319). Ablation method is the other process using a laser that can evaporate the materials and remove the defected layer. The laser processing of AM parts can considerably improve the roughness, wear and corrosion resistance, microstructure, and porosity. The laser processing leaves an excellent surface finish of about 1 nm which eliminates the need for sanding. When post-laser treatment is applied to Ti alloy, three different zones from the top surface toward the substrate are formed i.e., the treated zone (TZ), the heat-affected zone (HAZ), and the base material (BM). A titanium oxide layer is generated in the TZ. The HAZ includes lamellae of coarser grains and small equiaxed grains due to the induced recrystallization.

The energy transportation during laser polishing can be quantified as (Ref 252, 254, 256):
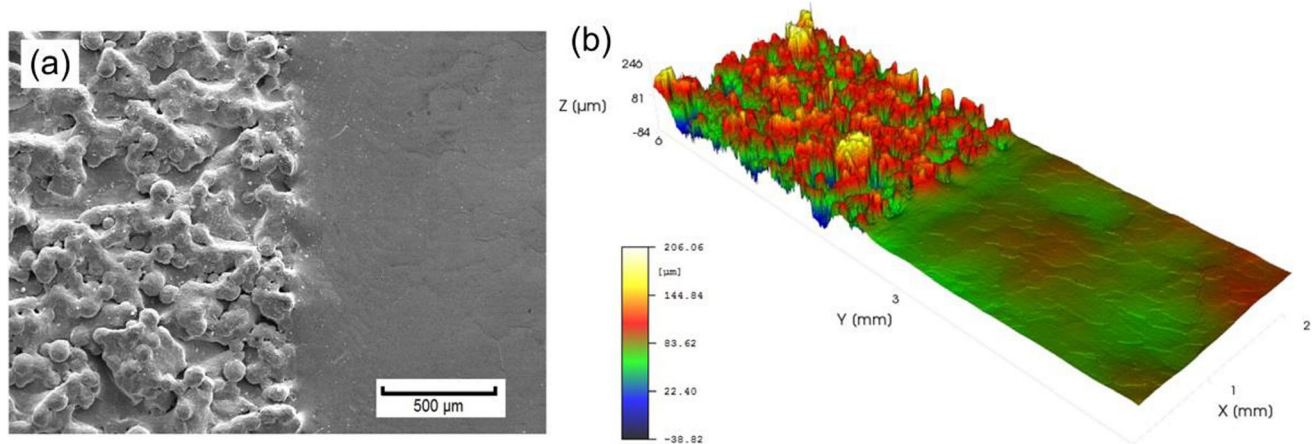
Fig. 18 Reduction in surface roughness achieved by laser polishing on EBM-built Ti6Al4V sample: (a) an SEM image showing the contrast between the original and polished surfaces; (b) the contrast between the original and polished topography, with an area of 2 × 6 mm (Ref 322). Reprinted from Additive Manufacturing, Vol 20, Yingtao Tian, Wojciech S. Gora, Aldara Pan Cabo, Lakshmi L. Parimi, Duncan P. Hand, Samuel Tammas-Williams, Philip B. Prangnell, Material interactions in laser polishing powder bed additive manufactured Ti6Al4V components, Pages 11-22, Copyright 2018, with permission from Elsevier

$$E = \frac{P}{D_0 \cdot v_p}, \qquad (\text{Eq 31})$$

where E is the energy density, P is the laser power, D_0 is the focus diameter, and v_p is the processing speed. When laser energy induces the material displacement on the surface of the treating specimen, the smoothening effect on the topography is determined by the attenuation of the high frequency waves as material flows. Such equivalency of laser interaction with material can be identified by the critical attenuation of frequency as (Ref 256, 321):

$$f_{\text{cr}} = \sqrt{\frac{\rho}{8\pi^2 \mu t_m}}, \qquad (\text{Eq 32})$$

where f_{cr} (1/mm) is the critical attenuation frequency, μ is dynamic viscosity, and t_m is the melting time. Equations 31 and 32 calculate the key parameters for laser polishing.

3.3.1 Laser Polishing (LP). In laser surface treating, an optical beam imparts energy onto the substrate material to conduct the ablation process. With sufficiently high intensities, the heating can be concentrated enough to first melt the substrate material within a localized zone, and then vaporize as well as ionize to form gas phase under the radiation. Meanwhile, the plasma and plume are also generated in the process due to the breakage of chemical bonds of the material through direct photon absorption. When the photon energy is adsorbed mainly by the chemical bond scission, the HAZ is controlled in size with reduced transient thermal stresses. Therefore, laser treatment is capable of applying a surface finish with little effect of bowing, warping, delamination, or edge melting but precise dimension control. Typical laser surface treatment reduces the roughness of an AM surface by remelting a layer of material approximately 50–200 μm in depth of the surface peak to fill the valley. Laser surface treatment using CO_2 and Nd:YAG laser system can obtain a reduction in R_a roughness up to 80% in average. Yung et al. applied LP to CoCr alloy fabricated by SLM and greatly reduce the surface roughness up to 93% from 4.6 to 0.4 μm with 8%

increase in Vickers hardness (Ref 253). Tian et al. found that LP is capable of achieving a surface roughness S_a at 0.51 μm from 21.5 μm before processing on EBM-fabricated Ti6Al4V samples, as shown in Fig. 18 (Ref 322). The microhardness has a 15% increase, up to 5.3 GPa as maximum, within the first 300 μm depth from the surface compared to as-built one. LP induces melting and quick solidification occurred in laser polishing and generates reinforcing precipitates. For example, γ' and γ'' precipitates were generated by laser polishing on SLM-built Inconel 718 alloy (Ref 323). Hard martensite phase can be observed on the LP-processed surface of 316L SS specimen (Ref 259). LP reduced the R_a from 7.5 to < 0.1 μm and increased its hardness from 345 to 440 HV. Hofele et al. studied the LP treatment on SLM-built AlSi10Mg alloy using both pulse and continuous laser modes (Ref 257, 258). The result reveals that the surface roughness R_a can be reduced from 12.22 to 0.145 μm but with increased surface porosity from 0.3 to 4.6%. Multi-pass LP treatment exhibits the process stability regarding varying initial surface roughness, although the size of remelting zone can be affected (Fig. 19). Xiao et al. tested the continuous wave laser polishing with the assistance of a steady magnetic field and found that it can achieve a surface roughness level of $R_a = 0.168$ μm and more than 100% increase of the microhardness on S136H steel (Ref 324). Temmler et al. summarized the formation of residual stress on the laser polished surface of ANSI H11 tool steel and analyzed the relationship among hardness HV 0.005, carbon content, oxygen content, polishing depth under Ar + 6 vol.% CO_2 atmosphere (Ref 320). The result shows a surface roughness of 50 nm is achieved and a residual tensile stress of up to 926 MPa is introduced to the treated surface.

Shot peening, laser peening, laser polishing, centrifugal finishing, and linishing have been applied for the surface modification of EBM- and SLM-printed Ti6Al4V articles to promote fatigue performance (Ref 229). The EBM samples are treated with HIP while SLM samples are treated with stress relieving heat treatment. Centrifugal finishing reduces the surface roughness of components by rotating a mixture of parts,
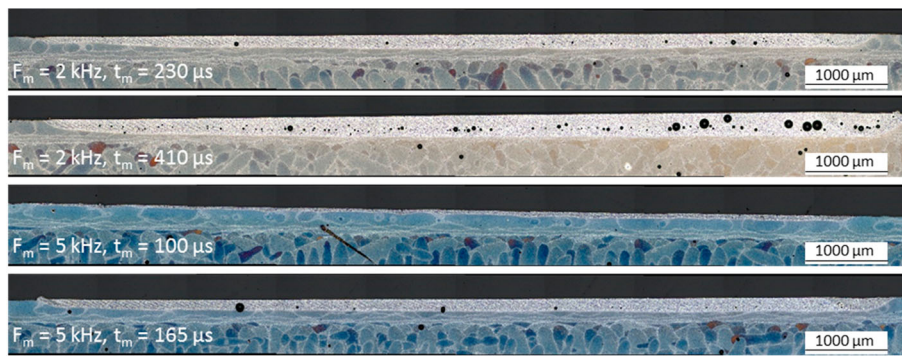
Fig. 19 Pores, remelted zone, polished zone on the cross section of SLM-built AlSi10Mg samples at different modulation frequencies f_m and modulation times t_m (Ref 257). Reproduced from Micromachines under the CC BY 4.0 license

abrasive media and carrying agents in a barrel. Linishing is the computer-controlled robot-operated process that uses high-speed abrasive brushes to diminish surface peaks and flatten surface valleys to achieve better surface roughness. The increase of fatigue strength after post-processing is listed for each post-process method as shot peening (EBM 110%, SLM 70%), laser peening (EBM 5%, SLM 20%), laser polishing (EBM − 30%, SLM − 50%), centrifugal finishing (EBM 100%, SLM 125%), and linishing (EBM 110%, SLM 25%). The fatigue strength of both EBM and SLM samples with as-built surface could be improved to levels comparable to wrought and machined Ti6Al4V alloy using centrifugal finishing or shot peening. The final fatigue strength after post-processing depends on a combination of surface roughness, surface residual stress, microstructure, and remaining defects. In addition, Fig. 20 illustrates the comparison of surface morphology of Ti-6Al-4 V produced by EBM/SLM and IN 718 alloy printed through SLM after different post-treatments.

3.3.2 Femtosecond Laser (FL) Machining. Femtosecond laser (FL) machining utilizes laser pulses with sub-picosecond duration to enable ultra-fast deposition of the energy into the material. Such interaction of laser and material is carried out by plasma mediated ablation, in which phonons are absorbed to lead to ionization and transformation of material to plasma with no intermediary phases. The HAZ on the specimen surface is greatly decreased in size and thereby allowing various heat-sensitive materials to be processed with sub-micron precision since the pulse duration time is much lower than the thermal diffusion time. An optimized laser pulse energy can be identified for surface finish and geometrical consistency. The areas irradiated with fs-laser radiation exhibit a reduction in surface roughness from about 100 μm to a few microns, depending on the process parameters and surface complexity (Ref 325). The use of high repetition rate ultra-fast laser radiation enables the efficient removal of the excessive material while precisely following the predetermined part geometry. Worts et al. adopted a FL with an amplified 10 kHz repetition rate, 185 fs pulse duration, and 100 μJ per pulse energy to treat the surface of SLM-produced Ti6Al4V part and reduced the surface roughness R_a from 4.2 to 0.8 μm (Ref 326). Lin et al. combined the FL and pulsed plasma polymerization (P^3) to deposit siloxane (SiO) and fluorocarbon (FC) stacking films using precursors of $C_6H_{18}OSi_2$ and C_4F_8 on 304 SS (Fig. 21) (Ref 327). After the deposition, the surface roughness R_a increased from 0.06 to 1.97 μm and the resulting SiO-

FC film exhibited strong superamphiphobicity and non-cytotoxicity.

3.4 Chemical and Electrochemical Polishing

Four common chemical treatments, i.e., chemical polishing (CP), chemical etching (CHE), electrochemical polishing (ECP), and electroplating for metallic AM are listed in Table 7. Chemical post-process methods are preferred for AM part due to their features such as improving the surface quality, promoting better dimensional and geometric stability, corrosion resistance, modifying the surface roughness, increasing abrasion resistance, and more (Ref 227). For example, passivation is the process of treating or coating a metal in order to reduce the chemical reactivity of its surface. In stainless steel, passivation means removing the free iron from the surface of the metal using an acid solution to prevent rust. Like in bio-application, CoCrMo have favorable wear properties compared to softer metals like titanium, thus coating CoCrMo increases the longevity of the implant by preserving the condition of articulating surfaces. Chemical etching or electrochemical polishing also has disadvantages: (a) they often result in excessive material removal that can affect part tolerances; (b) large features are not easily removed; (c) the preferential dissolution of some phases in multiphase alloys can cause short range roughening; and (d) conventional electropolishing methods are generally expensive and hazardous.

3.4.1 Chemical Polishing (CP). For CP treatment of Ti6Al4V SLM parts, standardized solution compositions are not applied. The suggested mixtures are often reported to be subject to the application. For high material removal rates, ultrasonic agitation is often applied for short processing times; however, preliminary investigations revealed that smoother surfaces ($R_a < 1$ μm) could be obtained with magnetic stirring and longer processing times (1 h) while ultrasonic agitation for the same duration led to cavitation and surface roughening. Heat treatment and chemical polishing under magnetic stirring are adopted to examine the effect on fatigue behavior of the Ti-6Al-4 V SLM specimen (Ref 328). The polishing efficiency is affected by the ratio of [HF]:[HNO3] in the solution. A relatively higher ratio shows increased efficiency and higher level of reduced surface roughness ($> 30\%$) to less than 2.0 μm. However, CP does not achieve a statistical higher fatigue performance without further polishing. The optimized chemical
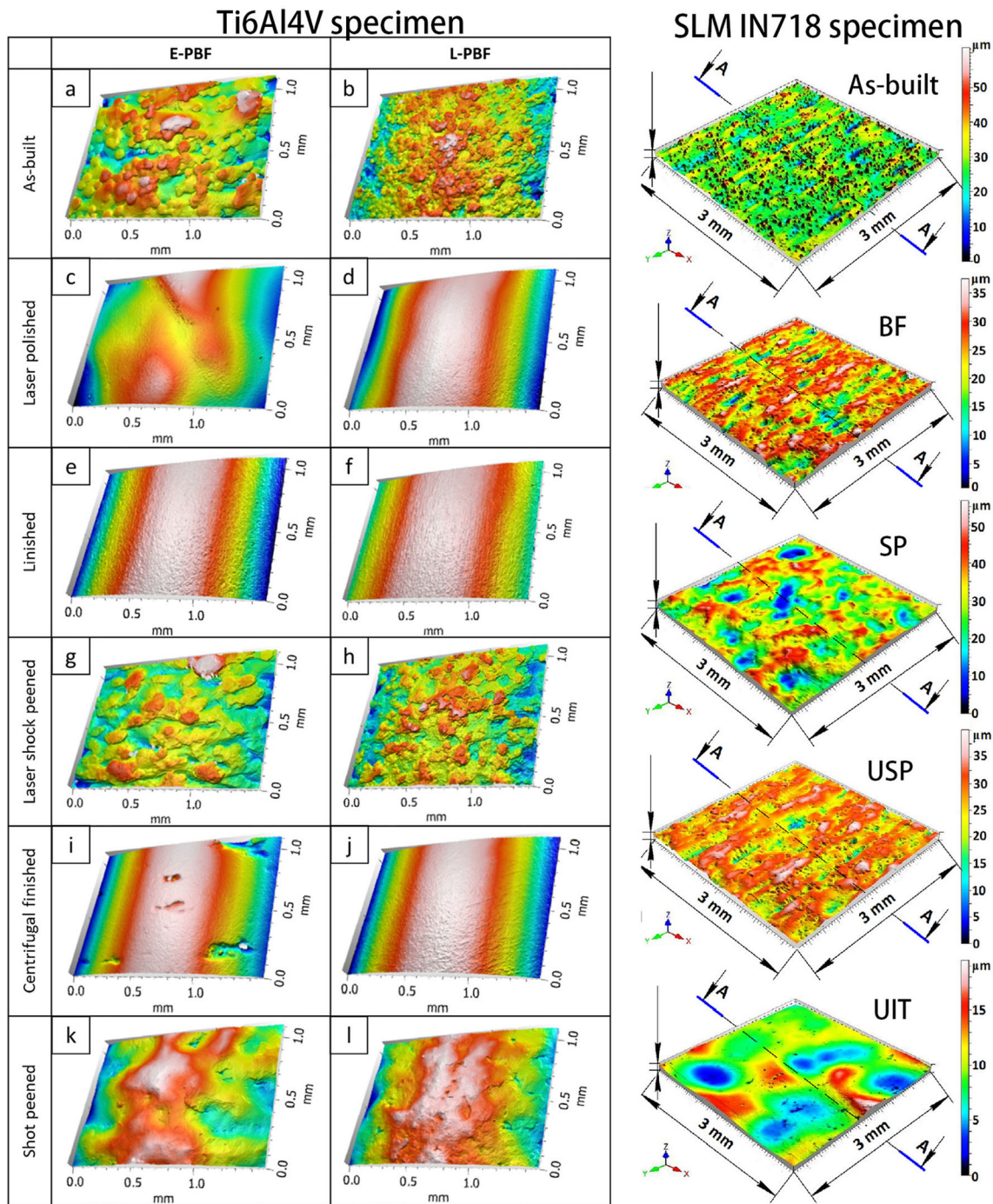
Fig. 20 Surface topography measured for as-built and post-processed specimen of EBM- and SLM-built Ti-6Al-4 V: laser polishing (LP), linishing, laser shock peening (LSP), centrifugal finishing (CF), shot peening (SP), SLM-built IN718 specimens: barrel finish (BF), shot peening (SP), ultrasonic shot peening (USP), ultrasonic impact treatment (UIT) (Ref 229, 237). Reprinted from International Journal of Fatigue, Vol 134, M. Kahlin, H. Ansell, D. Basu, A. Kerwin, L. Newton, B. Smith, J.J. Moverare, Improved fatigue strength of additively manufactured Ti6Al4V by surface post processing, Article 105,497, Copyright 2020, and from Surface and Coatings Technology, Vol 381, D.A. Lesyk, S. Martinez, B.N. Mordyuk, V.V. Dzhemelinskyi, A. Lamikiz, G.I. Prokopenko, Post-processing of the Inconel 718 alloy parts fabricated by selective laser melting: Effects of mechanical surface treatments on surface topography, porosity, hardness and residual stress, Article 125,136, Copyright 2020, with permission from Elsevier

polishing can remove all the partially sintered particles and layered defects on the surface. The comparison of Ti6Al4V sample surface treated with different concentration of HF-HNO$_3$ solution is shown in Fig. 22. Wysocki et al. applied three ratios of [HF]:[HNO3] solution system to CP treat the

SLM-built titanium scaffold (Ref 261). The result shows a significant improvement on the surface finish by removing the partially molten powder while Young's modulus and surface compressive stress are both reduced. Tyagi et al. utilized a commercial etching solution containing 10-30% phosphoric
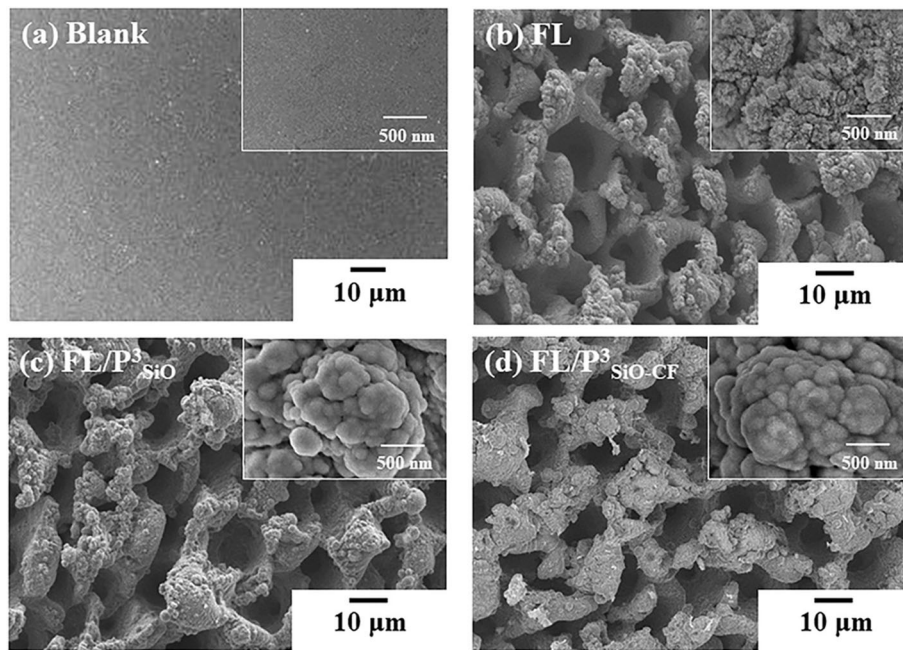
Fig. 21 SEM images on surface of 304 SS specimen with (a) blank, no treatment, (b) FL, femtosecond laser treatment, (c) FL/P^3 with SiO, treated with pulsed plasma polymerization to form siloxane nanoparticles, (d) FL/P^3 with SiO-FC, fluorocarbon coating (Ref 327). Reprinted from Surface and Coatings Technology, Vol 427, Cheng-Wei Lin, Ping-Yen Hsieh, Chia-Man Chou, Chi-Jen Chung, Ju-Liang He, Femtosecond laser surface roughening and pulsed plasma polymerization duplex treatment on medical-grade stainless steel substrates for orthodontic purpose, Article 127,819, Copyright 2021, with permission from Elsevier

Table 7 Post-processing approaches of chemical treatment

Process name	Description of the process
Chemical polishing (CP)	Specific bath of chemical solution is used for metallic materials to form passivation layer and polished surface
Chemical etching (CHE)	It enables chemical reactions between the chemical solutions (HCl, H_2SO_4, HF, HNO_3, COOH, HCl + HNO_3) and the metallic surface to diminish surface roughness
Electrochemical polishing (ECP)	Low-level dissolution of microsized irregularity at low temperature for fragile, complex parts; acidic electrolytes are used for AM metallic specimen
Electroplating	Metal film deposition on metallic surface electrolytically (Au, Ag, Zn, Cr, Cu, Ni, etc.)

acid, 1-10% hydrochloric acid, 1-10% nitric acid, and 1-10% proprietary surfactants to polish both the external and internal faces of SLM-built 316L SS part (Ref 329). Such CP process achieved an overall surface roughness R_a of 0.5 μm and also improved the corrosion resistance by the passivation layer.

3.4.2 Chemical Etching (CHE). A potential approach for reducing surface-level defects and porosity on complex geometries is chemical etching (CHE). CHE can improve the surface quality by cleaning the adhered particles and meanwhile have little impact on the fatigue properties. The process enables chemical reactions to occur between the chemical solutions and the surface to bring the surface roughness to the proper levels. The solutions are determined according to the properties of the metal surface. Typical solutions are used in CHE diluted and concentrated aqueous hydrochloric (HCl), sulfuric (H_2SO_4), nitric (HNO_3) and hydrofluoric (HF) acid, concentrated aqueous solutions such as oxalic acid ($(COOH)_2$) and aqua regia (HCl + HNO_3) chemical solutions. Before the process, AM samples are cleaned with soap solution, isopropyl alcohol,

distilled water, or ethanol to remove dust and loose powder particles that may disrupt chemical polishing. The AM-produced porous structures can be cleaned first in an ultrasonic bath using demineralized water, and then washed with ethanol followed by air drying to remove loose surface impurities and dust particles remaining in the pores. Afterward, the parts are immersed in the chemical solution and this solution abrades the dust particles attached to the surface of the porous structure and causes the weakly bonded particles to fall. The etchant removes material on the surface layer and blunts the surface defects and cracks. Optimizing the process settings and increasing overall energy can reduce the porosity. Chemical etching can cause significant deviation on the original geometry and dimensions due to indiscriminate low-contrast removal, as well as deterioration of the mechanical properties. For example, the material removal of Ti-6Al-4 V alloy using hydrofluoric acid (HF) based solutions can be described in Table 8 for the dissolution of titanium in HF-HNO_3 solutions. When titanium hexafluoride complex is the main reaction product, dissolution rate of
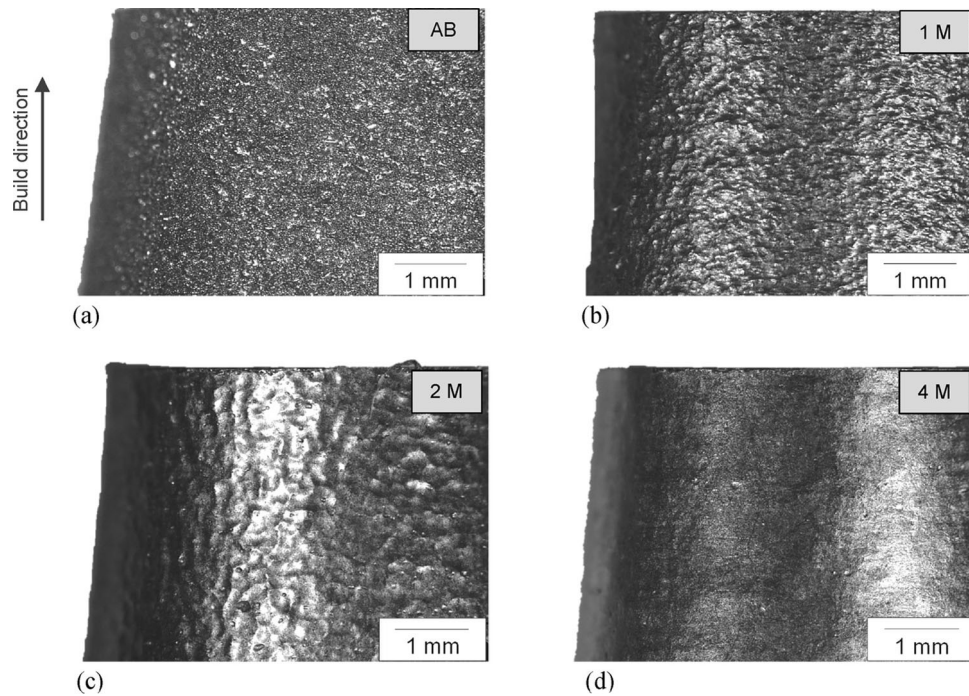
Fig. 22 Optical examination on treated surface of Ti-6Al-4 V ELI sample produced by SLM with different concentration of HF-HNO3: (a) as-built (AB), (b) [HF]:[HNO3] wt.% ratio = 1:10 (1 M), (c) [HF]:[HNO3] wt.% ratio = 1:5 (2 M), (d) [HF]:[HNO3] wt.% ratio = 1:2.5 (4 M) (Ref 328). Reprinted from Materials Today Communications, Vol 25, Martin Bezuidenhout, Gerrit Ter Haar, Thorsten Becker, Sabrina Rudolph, Oliver Damm, Natasha Sacks, The effect of HF-HNO$_3$ chemical polishing on the surface roughness and fatigue life of laser powder bed fusion produced Ti6Al4V, Article 101,396, Copyright 2020, with permission from Elsevier

titanium maintains a mole ratio of 1:6.4 between the expected moles of titanium to be removed and available HF in the solution accounting for the reactions with Al and V. In the case of insufficient HF, the titanium surface is gradually passivated through the reaction of nitric acid with the adsorbed trivalent titanium cations.

Chemical etching is applied to Ti-6Al-4 V specimen fabricated by the EBM process (Ref 155). Each specimen is dipped at room temperature in a fresh solution consisting of 12 mL HF (48%), 40 mL HNO$_3$ and 300 mL of distilled water without stirring. The specimens are rinsed under water immediately after being removed from the etchant in order to eliminate any trace of acid. Etching for 30 min eliminates most of pores in the subsurface region and reduces the roughness values R_a and R_z by 26 and 21%. After 60 min of etching, those values reach 39 and 34%, respectively. Elongation of the specimen after etching is increased by 36 and 41% for 30 min and 60 min. Notch-like defects that intersect the sample surface and plate-pile stacking defects are dissolved but not 100% removed from the surface. The etched specimen exhibit YS and UTS values as high as those of machined samples. Etching prevents the early failure from crack propagation, improves the ductility, and decreases the scattering of the data. After etching, the stress concentrations are much smaller and crack initiation leading to failure is delayed. CHE also has been applied to surface treating of lattice and strut specimens of Ti-6Al-4 V alloy as well as scaffold of CoCr alloy (Ref 112, 122, 330). The treatment includes degreasing using ethanol in an ultrasonic bath and etching in a solution of HF, HNO$_3$ and demineralized water in an ultrasonic bath. The strut thinning, which leads to a decrease of compressive proof stress, is also observed after etching. Etching also decreases the relative density by less than

8 and 10% after 3-min and 6-min processing, respectively. The specimens after both HIP and 6 min surface treatment has the lowest level of compressive proof stress measured at 28.49 MPa. Hooreweder et al. stated that the aqueous solution of 27 vol.% HCl and 8 vol.% H$_2$O$_2$ is capable of removing the remnant particles from the SLM-built CoCr scaffold samples but has no impact on strength and fatigue response (Ref 265). Generally, although CHE decreases the overall density and thereby the strength of the scaffolds, the improvement of the surface finish results in a substantial increase in fatigue resistance. CHE removes partially molten particles attached to the struts and reduces the local stress concentration. A combination of HIP, sand blasting, and CHE demonstrates the most effective approach for improving the fatigue behavior of lattice structures.

3.4.3 Electrochemical Polishing (ECP). Electrochemical polishing (ECP), also called electropolishing (EP), is an electrochemical dissolution process in an electrolytic cell, which is the reverse of electroplating. In ECP process, the sample and electrodes are immersed in the electrolyte for a specified time and applied with a potential difference between the electrodes. During ECP, a certain current is required to be maintained for a sufficient time. The anode and cathode are chosen based on the material of the target workpiece. Table 9 lists the chemical solution used as electrolyte in the previous studies. When current passes through the electrolyte, the peaks of the surface are more exposed to the dissolution, thereby smoothing the surface. The expected reaction happening on the anode side would be the oxidation of metal into the corresponding metal ions:

$$M(s) \rightarrow M^{n+} + ne^- \qquad \text{(Eq 33)}$$

Table 8 Reactions between titanium alloy and hydrofluoric acid during etching

Stage	Reaction formula
HF to react with TiO_2 film and titanium	$TiO_2 + 6HF \rightarrow [TiF_6]^{2-} + 2H^+ + 2H_2O$
	$2Ti + 6HF \rightarrow 2Ti^{3+} + 3H_{2(g)} + 6F^-$
Nitric acid to oxidize the H_2 gas to lower H_2 absorption	$3H_{2(g)} + 2HNO_3 \rightarrow 4H_2O + 2NO_{x(g)}$
Combined reaction considering acid dissolution	$Ti + 6HF + 2HNO_3 \rightarrow [TiF_6]^{2-} + 2HNO_2 + 3H_2O + 2H^+$

where M = metal element.

At the cathode surface, reduction of hydrogen ions to hydrogen gas would be expected to occur as the main reaction:

$$H^+ + e^- \rightarrow \frac{1}{2}H_2(g) \uparrow . \qquad \text{(Eq 34)}$$
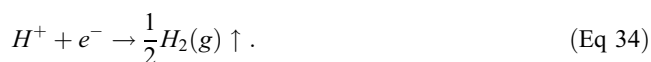
The solution typically was agitated by rotating a magnetic stirrer to avoid the agglomeration of the etching product near the AM sample surface. The experimental variables to be considered in the ECP include current density, electrode gaps, polishing time, electrolyte temperatures, type of electrolyte, and flow rate.

Electrochemical machining (ECM) is similar to ECP, which is also based on the phenomenon of electrochemical dissolution. Both the work piece and the tool material are dipped in the electrolyte solution, working as anode and cathode, respectively. The dissolution process occurs when an external current is present. ECM used as post-processing step for AM parts is particularly useful for functional surfaces, especially friction surfaces (contact surfaces), that require comparatively high quality (Ref 331). ECM can produce surfaces with a defined roughness, which also have the properties to withstand a steady friction use. ECM-treated metallic parts satisfy the tight dimensional tolerances.

ECP is aimed for fine polishing of the metallic surface with a mirror finish. It reduces the surface roughness, releases the residual stresses, removes material as well as impurities and irregularities from the anode by oxidation, and create a new passive layer. Such protective passive oxide layer slows down the reaction causing corrosion and increases the corrosion resistance. ECP can be used as the final step to heal the subsurface damages on the as-printed, mechanical, and thermal processed surfaces of AM-fabricated parts. It also minimizes the surface features like defect, microstructural variation, and preferred crystallographic orientation. ECP has no contact between the tool and the part, which leads to little wear and low residual stress.

Although ECP can substantially improve the surface roughness and increase the corrosion resistance, it reduces the hardness and Young's modulus of the treated metallic structure, which can be associated with dissolution of precipitates during processing and removal of residual surfaces. ECP is also ineffective to achieve micrometer level of roughness when treating internal surface and surface with rough initial conditions (Ref 271). Meanwhile, ECP typically shows no impact on YS but may have positive influence on UTS and elongation. The non-conductive phases present in the AM alloys are not affected by the ECP treatment and this impairs the surface quality of the AM alloys. The ineffectiveness of ECP method to the non-conductive phases and the difficulty of controlling the ECP process due to various variables are the disadvantages of this method. ECP also requires additional preparation of electrodes.

ECP is more effective to reduce the outer surface roughness than CP treatment. But the CP shows higher efficiency in polishing the internal surface than ECP. In addition, the overpotential ECP (OCEP), which is conducted at an elevated temperature (50-60 °C) with a suitable electrolyte for different metal alloys, can be more effective at improving the surface roughness (Ref 272). A combination of overpotential and conventional electrochemical polishing can achieve a highly selective removal of sticking particles. Kim et al. performed ECP to a 316L stainless steel cylindrical sample and reduced its roughness from 59 to 6 nm and corrosion current by nearly one order of magnitude (Ref 268). Zhang et al. performed ECP to SLM-built IN718 structure with a current density of 50 A/dm^2 in 20% vol. sulfuric acid/absolute methanol and agitation of 200 rpm (Ref 269). The surface roughness after 5 min of ECP reduces from 6.05 to 3.66 μm. The hardness and elastic modulus dropped from 4.7 to 3.8 GPa, 252 to 117 GPa, respectively. The reduction can be attributed to release of residual stress of sample surface and dissolution of reinforcing precipitates at the surface. The influence of ion concentration of the electrolyte is also critical to the ECP process. Zhang et al. demonstrated the reduction of surface roughness and weight loss of the target material with increasing the chloride concentration during 10 min of ECP at 0.5 A · cm^2 current density and 25 °C for SLM-produced Ti6Al4V alloy (Ref 270). Aggressive ECP parameters, such as high concentration of electrolyte and long treating time have a negative effect on the surface roughness and can potentially damage the printed structure.

When treating 316L SS, a solution of 50 vol.% phosphoric acid, 20 vol.% sulfuric acid, and 30 vol.% DI water can be used with a Nb counter electrode with a parallelepiped prism. The polishing process is conducted for 12 min at 5 A with reversing the polarity every 2 min to reduce the oxide deposition (Ref 231). ECP is tested and compared with contour scan strategy/remelting, tumble finish (TF), passivation, grinding/polishing on the effectiveness of surface treating for SLM-built 316L SS samples. TF is conducted for 3 h at a pulse rate of 2000 per min with different sizes of ceramic media. Passivation is carried out according to ASTM A967/A967M. Figure 23 illustrates the cross-sectional view of the treated samples and the relationship between breakdown potential (E_b) and surface roughness. ECP shows the most reduced roughness on the surface and a relative higher E_b, which indicates a lower susceptibility to the initiation of localized corrosion. Both TF and ECP flatten the surface peaks and smooth the surface on a complex part to reduce the susceptibility to pit initiation (higher E_b). TF-treated sample shows residual overhung features and area of oxygen rich layers leading to lower E_b, while both are mostly removed by ECP and grinding processes. Passivation of the as-printed

Table 9   Potential chemical solutions used in literature for different metals

AM material	Electrolyte solution
IN718	H_2SO_4 + methanol (Ref 269)
IN625	Perchloric acid + glacial acetic acid (Ref 275)
	H_2SO_4 + methanol (Ref 332)
Ti6Al4V	Ethanol + n-butyl alcohol + $Al(H_2O)_6Cl_3$ + $ZnCl_2$ (Ref 264)
	Ethanol + isopropyl alcohol + $Al(H_2O)_6Cl_3$ + $ZnCl_2$ (Ref 59, 333)
	Perchloric acid + acetic acid (Ref 235, 276)
	Ethylene glycol + magnesium chloride (Ref 270)
	CH_3COOH + H_2SO_4 + HF (Ref 266)
CoCr	H_3PO_4 + H_2SO_4 (Ref 277, 278)
CoCrFeMnNi	H_2SO_4 + methanol (Ref 334)
316L SS	H_3PO_4 + H_2SO_4 + DI water (+ glycerol) (Ref 231, 233, 262, 268, 272, 273)
	Choline chloride + ethylene glycol + urea + malonic acid (Ref 274)
AlSi10Mg	Ethanol + ether + $HClO_4$ (Ref 240)

part is ineffective in promoting the E_b and has minimal impact on the corrosion susceptibility. The ECP treatment may provide a robust approach for reducing surface roughness, removing tortuous surface features, and reducing susceptibility to localized corrosion for complex AM metal parts. In another study, ECP with deep eutectic solvents (DESs) reduced the R_a value to < 0.4 μm and increased the E_b from 40.6 to 127.2 mV/SCE (Ref 274).

To enhance the surface quality and dimensional accuracy of CoCrFeMnNi HEAs fabricated by SLM, five different surface finish approaches are adopted for comparison (Ref 334). The deformation of the microstructures resulted in the subsurface defects which induced the increment of microhardness and residua stress. Milling, grinding, EDM, ECP, and polishing reduce the surface roughness of the as-print CoCrFeMnNi HEA specimen from 30 μm to 1.0, 3.0, 4.0, 15.0, and 0.003 μm, respectively. When ECP is performed subsequently to milling, grinding, and EDM, the combined approaches further reduce the R_a. The microhardness of milling, grinding, and EDM specimens are greater than 300 HV, while the subsequent ECP lowers the hardness to around 200 HV due to substantial residual compressive stresses. Polishing leads to a similar microhardness since it is a low force process. A heat-affected layer is identified after EDM, which is caused by plastic deformation. More deformation is observed in milling sample than that in grinding sample. The contaminant of Cu and the heat-affected layer in EDM, as well as the deformation surface feature can all be diminished by the ECP. Damage-free surface can only be obtained by ECP and polishing, while milling and grinding cause micropores on the surface.

A series of post-processes of stress-relief, HIP, ECP, and SP are applied to SLM Ti-6Al-4 V alloy (Ref 212). The ECP treatment employs an alcoholic solution of aluminum chloride and zinc chloride. SP uses ZrO_2 and SiO_2 ceramic beads. The heat treatments of SR and HIP both decrease the YS and UTS of the as-built specimen around 10%. The surface roughness R_a is reduced from 6.83 μm of as-built condition to 5.07, 0.54, and 3.36 μm after HIP, ECP, and SP, respectively. HIP can reduce the porosity from 0.35% to below 0.05% on the as-built samples, and the remaining small pores have less detrimental influence on the fatigue behavior compared to calculation. SP is effective at deforming the large pores in the surface layer but has little impact on reducing the amount of the defects. A linear-declining SN curve indicates that surface peening is capable of reducing the crack initiation in the surface layer but has limited impact on the subsurface cracks and thereby causing crack initiation at high cycle fatigue regime. ECP does not show strong correlation in increasing the fatigue strength due to the large defects in the surface layer. Since the surface treatments have no substantial improvement on the surface roughness, no remarkable influence is observed on the fatigue resistance.

Uzan et al. adopted SP plus either mechanical polishing (MP) or ECP to enhance the surface of SLM-built AlSi10Mg alloy specimen (Ref 240). Figure 24 shows the improved fatigue resistance at a fixed 125 MPa load and S-N curve for SP, SP + MP, and SP + ECP conditions. ECP treatment on the SP specimen increases the maximum stress at 10^6 cycles from 110 to 118 MPa while under 125 MPa load ECP promotes the fatigue life from 1.9×10^5 to 3.1×10^5 cycles. Although SP + MP exhibits higher fatigue resistance, the surface finish after SP + ECP shows greater smoothness on the surface morphology.

3.5 Deposition and Coating

3.5.1 Laser Cladding. When LENS is used for surface modification, laser cladding can melt a thin layer of the target material by the laser beam to bond on the workpiece surface. It is a widely used technique of surface treatment/engineering in the industry to apply specific coating to metallic/ceramic structures for enhancement of surface properties especially for high wear resistance, oxidation resistance, or bio-compatibility for rigorous conditions. A clad track is created by injecting powder particles into the molten pool and finally solidifies as a pure clad layer with strong bonding to the substrate. The width of the track (clad width) and the thickness of the layer (clad height) depend both on the powder feed rate and the laser power. The cladding system consists of a fiber laser system and a powder feeding system, which typically equipped with a helicoidal coaxial nozzle. Nd:YAG laser cladding was proven to be more energy efficient with 50% of the raw power to be consumed for the process (with 20% used for melting the powder and 30% for heating the substrate) (Ref 335). Many systems of coating material have been developed, including titanium, cobalt, and nickel matrix reinforced by borides, carbides, nitrides, and intermetallic compound such as Ti_2Ni,

TiSi$_2$, Ni$_3$Ti, Ti$_3$AlN, Ti$_3$SiC$_2$, TiB, TiC, TiN, TiBCN, W$_2$C/ WC, Cr$_3$C$_2$, SiC, Ni$_2$Si/NiSi, MoSi$_2$, etc. When coating material is deposited onto the substrate, cladding and bonding zones form with dense microstructure under high heat temperature and fast cooling, which leads to solid solution phases and retaining the properties of the base material, minimizes the number of liquation cracks and yields higher-quality joints compared to vacuum brazing and arc welding. Other advantages include short processing time, flexibility, and precision in operation. However, the surface of each layer is uneven and susceptible to incomplete fusion as well as formation of pore/ microcrack, which significantly deteriorate the mechanical properties of bonding and cladding layer.

During cladding, the powder that impacts the substrate is retained by the surface. The fraction of the retained powder, which leads to the clad formation, can be estimated by (Ref 336):

$$\lambda = \frac{\dot{m}}{\dot{m}_f} = \frac{\dot{m}}{\rho_c u(V/l)} = \frac{\dot{m}_{\text{melted}} + \dot{m}_{\text{catch}}}{\rho_c u(V/l)}, \qquad \text{(Eq 35)}$$

where ρ_c is the cladding material density, u is the scanning speed, $\dot{m}$ is the powder feed rate contributing to the clad formation, $\dot{m}_f$ is the actual powder feed rate that the feeder provides to the process, and V/l is the clad volume per unit length, $\dot{m}_{\text{melted}}$ is the portion of the feed rate contributed by melted particles, and $\dot{m}_{\text{catch}}$ is the portion of solid particles. If assuming all particles that reach the liquid surface are in a liquid state and considering the mass of the liquid particles is determined from the energy consumed for the melting and the latent heat of fusion, the feed rate of melted particles can be written as:

$$\dot{m}_{\text{melted}} = \frac{m_{\text{melted}}}{t} = \frac{Q_{\text{particles}}}{t \cdot L} = \frac{a \cdot Q_L}{t \cdot L} = \frac{a \cdot P}{L} \qquad \text{(Eq 36)}$$

where Q_L is the total laser power delivered by the laser source, L is the latent heat of fusion of the particle material, P is the laser power, and a is the ratio of the energy absorbed by the particles. Equation 35 and 36 provide a simplified approach to estimate the cladding process based on laser power, coating material, and other process parameters.

Deng et al. deposited CoCrFeNiMo$_{0.2}$ HEA coating to enhance Ti6Al4V through laser cladding (Ref 337). The result showed that after cladding BCC solid solution phase and σ phase with non-uniform grain structure was formed by the high cooling rate on the substrate. The microhardness of the coated part reached to 900 HV compared to ∼ 400 HV of the Ti6Al4V base material. The oxidation resistance is also significantly improved since the dense Cr-enriched oxide layer effectively inhibits the inward diffusion of oxygen at elevated temperature. The corrosion potential of the coating is increased, while the corrosion current density is reduced, which indicates a higher corrosion resistance. In addition, a higher compressive residual stress is presented on the coating, which is also beneficial to the wear and fatigue resistance of the treated Ti6Al4V part. Maliutina et al. fed Ti48Al2Cr2Nb powder to laser cladding on TA6Zr4DE alloy part and resulted in a lamellar structure of γ-TiAl and α$_2$-Ti$_3$Al phases with deformation twins and high dislocation density (Ref 338). During oxidation, an oxide layer of 15 μm formed after 100 h at 900 °C containing TiO2 and Al2O3 that inhibit the oxygen diffusion. With the alloying element of niobium and chromium, the mass gain of the treated TA6Zr4DE part is one tenth of that of the untreated one. Bidron

et al. adopted laser cladding to refurnish cast CM247LC alloy parts with CM247LC powder without inducing hot cracking and found preheating over 1100 °C minimized the susceptibility of crack formation (Ref 339). When cladding was used to refurbish Ni-based superalloy K447A, the coating exhibits similar microhardness to the base structure, greater tensile strength but reduced plasticity due to the shrinkage defects and microcracks (Ref 139). STA treatment can promote the microhardness and recover the ductility, while it also decreases UTS and YS.

3.5.2 Electrospark Deposition (ESD). Electrospark deposition (ESD) can apply a metal coating on the AM part to improve the surface finish. Based on the different characteristics of the tool and target material, 80-90% of reduction in surface roughness of R_a can be achieved (Ref 202). When Inconel 718 coated through ESD onto Hastelloy X fabricated by SLM, surface hardness increases 85% with further hammer peening. The combined treatment leads to a greater size of the thermo-mechanically affected zone (TMAZ) but has no influence on the average coating thickness. With annealing and aging heat treatment to eliminate the TMAZ prior to forming the strengthening γ″ and γ′ phases, a much higher fatigue life, i.e., 50 and 5 times greater, at a stress of 350 and 550 MPa can be achieved, respectively. Figure 25 shows the effect of ESD and hammer peening on the side surface of the samples. Partially fused particles are remelted and covered under the Inconel coating (Fig. 25b). Hammer peening further smoothens the surface (Fig. 25c). In another work, AA4043 aluminum alloy was deposited by ESD on BJAM-fabricated IN625 specimen (Ref 279). The microhardness of the ESD coated sample is significantly promoted from ∼ 110 HV of the IN625 substrate to the range of 430-960 HV. This is caused by the different compounds, such as Ni$_2$Al$_3$ and other nickel aluminides, formed during the ESD process and unevenly distributed on the coated surface.

3.5.3 Magnetron Sputtering (MS). Magnetron sputtering is a common method to deposit diamond-like carbon (DLC) coatings, which can improve the surface properties. DLC exhibits chemical inertness, high hardness, low friction, and high wear resistance at normal ambient conditions and therefore is modified for scratch-resistant and tribological applications. Tillman et al. deposited DLC coatings using magnetron sputtering on to steel alloys fabricated by SLM, as shown in Fig. 26 (Ref 280, 281). It significantly promotes the hardness from ∼ 5 GPa to more than 20 GPa. In addition, the coefficient of friction is reduced from 0.7 to less than 0.3. The disadvantage of sputtering DLC coating is that it increases the surface roughness.

3.5.4 Atomic/Molecular Layer Deposition (ALD/ MLD). Atomic/molecular layer deposition (ALD/MLD) are techniques that deposit vapor phase thin film onto the substrate that enables a coating with high material quality, good uniformity, high conformality, and accurate thickness control (Ref 340). This post-processing method submits the targeting material to different alternate pulsing of precursor and reactant gases in a reaction chamber, allowing for the attachment of molecules to exposed surfaces. The coating/film is deposited layer-by-layer on the material, which gives an unparalleled control of the film thickness on the atomic level.

ALD is not suitable for the deposition of the micrometer-thick films onto metallic structure, while chemical vapor deposition (CVD) is capable of thick film deposition. Therefore, Moll et al. first deposited a layer of AlN by the CVD
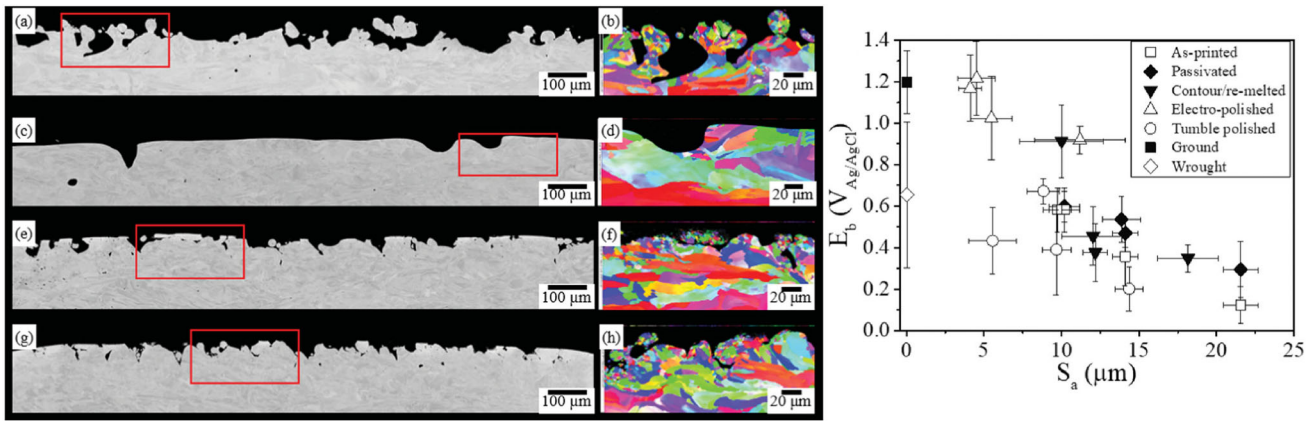
Fig. 23 SEM and EBSD maps of surface cross sections for (a, b) as-printed, (c, d) electro-polished, (e, f) tumble finish, (g, h) contour scan/remelting, and scatter plots of E_b with surface roughness measurements S_a (Ref 231). Reproduced from npj Materials Degradation under the CC BY 4.0 license
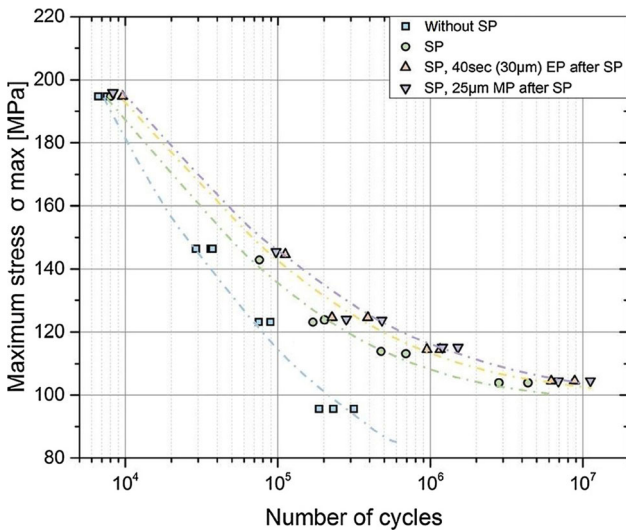
Fig. 24 S–N curves for SLM-built AlSi10Mg specimens under as-built, SP, SP + ECP, SP + MP conditions and also fatigue resistance under a fixed 125 MPa load (Ref 240). Reprinted from Additive Manufacturing, Vol 21, Naor Elad Uzan, Shlomo Ramati, Roni Shneck, Nachum Frage, Ori Yeheskel, On the effect of shot-peening on fatigue resistance of AlSi10Mg specimens fabricated by additive manufacturing using selective laser melting (AM-SLM), Pages 458–464, Copyright 2018, with permission from Elsevier

process using $AlCl_3$ formed by in situ chlorination from Al and Cl_2 gas and controlled the growth of AlN by the reaction between $NH_3 + H_2$ and $AlCl_3$, while plasma-enhanced ALD (PEALD) of AlN was carried out in reactor at 350 °C with precursor trimethylaluminium (TMA) and NH_3 (Ref 341). Figure 27a and b shows the TEM results on the cross section of the sample and reveal the topography and crystal orientation of the AlN coating on the Ti6Al4V substrate. Figure 27c shows the substantially declined mass gain measured on the coated sample compared to that of uncoated obtained in oxidation test. ALD has also been exploited to coat the metallic electrode such

as 3D printed titanium structure with MoS_2 for electrocatalytic performance of hydrogen evolution reaction (HER) (Ref 342).

3.6 Other Surface Treatments

3.6.1 Other Hot Working. Hot working, like hot compression and hot rolling, transforms and refines the microstructure. It eliminates the material defects by refining and homogenizing the inner grains through recrystallization and improves the related mechanical properties. Hot compression reduces the porosity ($< 0.1\%$) in the sample and thereby increasing the density of the microstructure by annihilating the pores (Ref 121). Hot rolling further refines the grain structure with improved cohesive strength and elongation of the deposits substantially. On the other hand, cold work via rolling can be applied to the part directly after material deposition in order to improve the microstructure and reduce porosity (Ref 343). Rolling continuously induces plastic deformation to cover the entire volume of printed section, which reduces tension stress on the interface but also generates compressive stress spreading over the whole section rather than on the surface only. The resulting distortion in the longitudinal direction is also reduced. Hot-rolled IN718 part fabricated by SLM exhibits superior creep lifetimes (~ 200 h) compared to conditions of as-built, heat-treated, and HIP at conditions of 650 MPa and 650 °C (Ref 136). The fine-grain microstructure in the hot-rolled part promotes the resistance to fracture under creep conditions, which leads to a ductile fracture surface. Hönnige et al. fabricated Ti6Al4V thin section specimen by a converted friction stir welding CNC gantry with a WAAM deposition unit and a customized roller device (Ref 282). After treated with SR and machining, the specimen is examined for the surface stress status. The inter-pass rolling shows little impact on the residual stresses.

3.6.2 Electropulsing Treatment (EPT). Electropulsing treatment (EPT), also called electropulsing processing (EPP) can modify microstructures of AM parts more rapidly than conventional annealing (Ref 289, 344). It utilizes either a
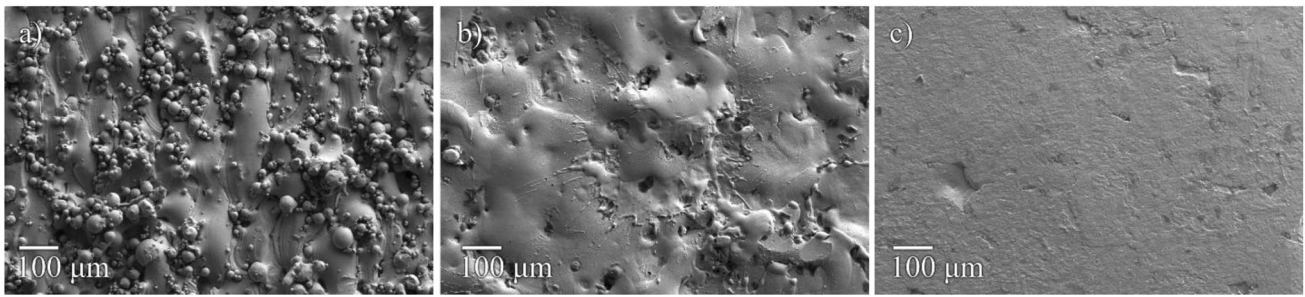
Fig. 25 Comparison on side surface of SLM Hastelloy X samples (a) as-built, (b) after ESD with Inconel 718, (c) after ESD + hammer peening under SEM analysis (Ref 202). Reprinted from Additive Manufacturing, Vol 36, Pablo D. Enrique, Ali Keshavarzkermani, Reza Esmaeilizadeh, Stephen Peterkin, Hamid Jahed, Ehsan Toyserkani, Norman Y. Zhou, Enhancing fatigue life of additive manufactured parts with electrospark deposition post-processing, Article 101,526, Copyright 2020, with permission from Elsevier
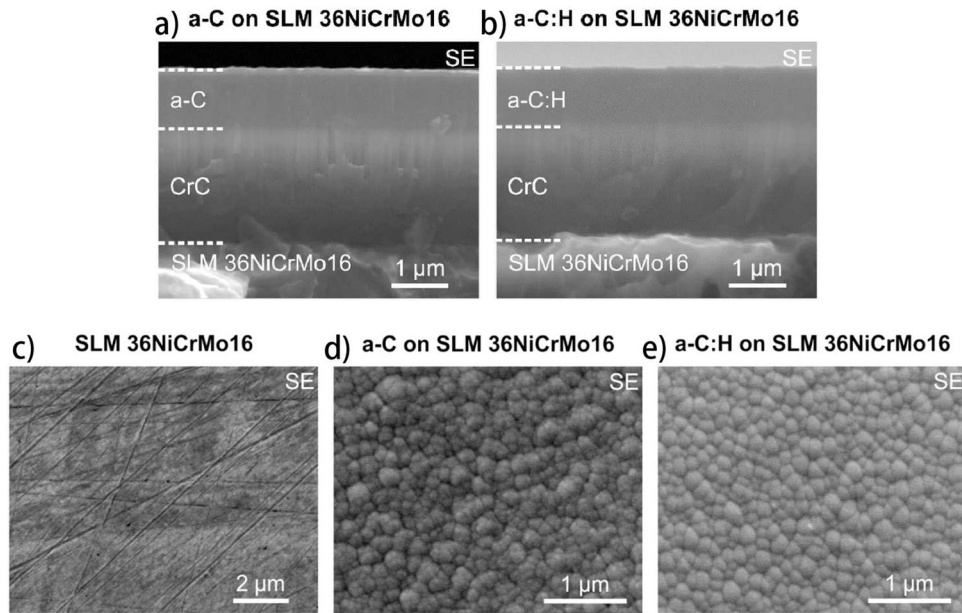

Fig. 26 morphology of the deposited DLC films by sputtering on SLM-built 36NiCrMo16 steel: (a) a-C film, (b) a-C:H film, (c) with no DLC coating, (d) a-c film, (e) a-C:H film (Ref 280). Reprinted from Surface and Coatings Technology, Vol 394, Wolfgang Tillmann, Nelson Filipe Lopes Dias, Dominic Stangier, Leif Hagen, Mirko Schaper, Florian Hengsbach, Kay-Peter Hoyer, Tribo-mechanical properties and adhesion behavior of DLC coatings sputtered onto 36NiCrMo16 produced by selective laser melting, Article 125,748, Copyright 2020, with permission from Elsevier

continuous current, or multiple pulses of high-current density with short duration to electrify the metallic surface. Both direct current (DC) and alternating current (AC) mode have been applied in the research. Similar to thermal annealing, electropulsing primarily alters the distribution of chemical phases and microstructural defects within materials. Furthermore, it significantly accelerates processes such as recrystallization, particle spheroidization, and grain growth. Electropulsing is effective in transforming the microstructure through the joule heating but has little impact on the dislocation density and grain macrostructure even when the current density is high. Electropulsing has potential to reduce internal residual stresses and porosity. For 316 L SS samples printed by SLM, the electropulsing reduces microsegregation without significantly altering the Vickers hardness or dislocation and grain structures. For AlSi10Mg samples, it partially spheroidizes the cellular, Si-rich, eutectic constituent created by rapid solidification. This increases the ductility and decreases the strength of

treated AlSi10Mg samples. For both materials, significantly less time is required to produce these microstructural changes via electropulsing than via thermal annealing. Applying EPT (10.7 A/mm^2 for 150 s) on Cu-20Ni-20Mn alloy decreases the dislocation density, accelerates the recovery as well as recrystallization, and dissolves the secondary phase, which enhances both the tensile strength and ductility (Ref 345).

3.6.3 Friction Stir Processing (FSP). FSP, an advanced technique derived from friction stir welding, can be used as a localized surface treatment for metallic component. FSP can be applied to refine the grains, improve the microstructure and properties of the materials to achieve ductilization. It can also reduce the porosity and potentially improve the fatigue performance of the part, which allows FSP to be an alternative approach for HIP. The printed specimen has an elongated grain microstructure with high portion of low-angle grain boundaries (LAGBs). The microstructure of as-built part after FSP is dominated by recrystallized fine equiaxed grains with high-
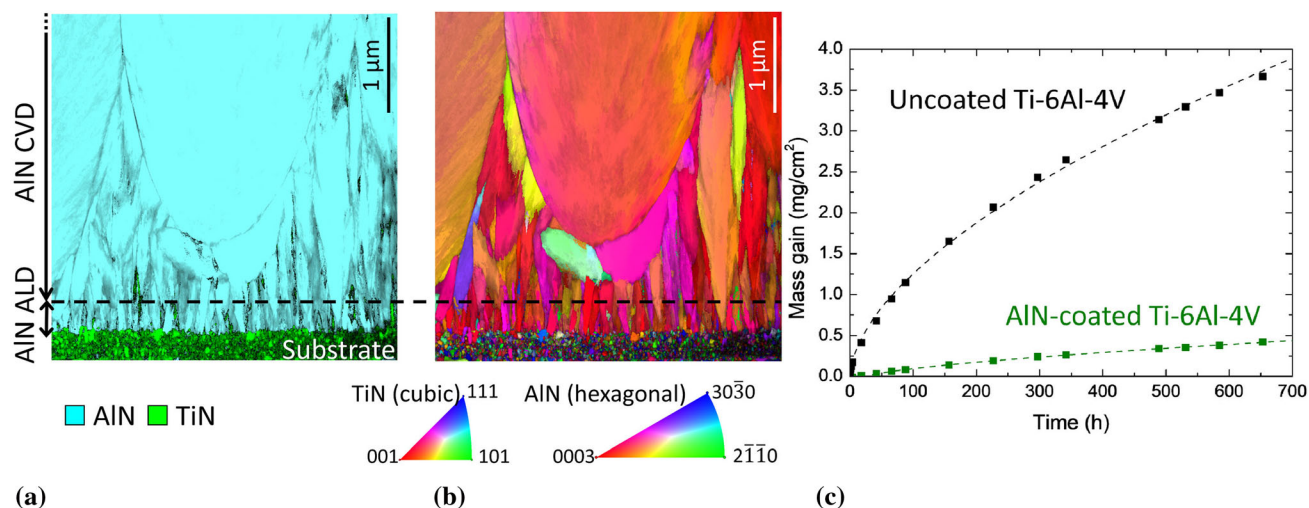
Fig. 27 TEM-ASTAR analysis of the CVD AlN film on the top of a 300-nm-thick ALD pre-deposition: (a) phase cartography and (b) crystallographic orientation along the growth direction, and the comparison of mass gaining in air oxidation of EBM Ti6Al4V uncoated and coated by a 7 μm thick AlN (ALD + CVD) at 650 °C, in which the dashed line shows the kinetic laws for AlN-coated and uncoated Ti6Al4V (Ref 341). Reprinted from Surface and Coatings Technology, Vol 415, A. Moll, J.-J. Blandin, R. Dendievel, E. Gicquel, M. Pons, C. Jimenez, E. Blanquet, F. Mercier, Coupling powder bed additive manufacturing and vapor phase deposition methods for elaboration of coated 3D Ti-6Al-4 V architectures with enhanced surface properties, Article 127,130, Copyright 2021, with permission from Elsevier

angle grain boundaries (HAGBs) including twin boundaries (TBs). The precipitates and grains are refined and homogenized due to the SPD and stirring produced by FSP, which increases their Vickers hardness. Furthermore, the strength and hardness of the AM parts after FSP are both promoted while the dimensional accuracy and geometry feature are not affected. FSP can also influence a larger depth as compared to other surface treatment techniques such as shot peening. A combination treatment of HIP + FSP has been adopted to enhance the AlSi10Mg samples fabricated by SLM (Ref 287). The FSP homogenizes the microstructure with fine equiaxed grains and significantly reduces porosity. The FSP alone on the as-built sample transforms the fibrous Si network into nanoscale particles by dynamic recrystallization. The FSP of the HIP sample promotes greatly the grain refinement by transforming the microstructure into fine Al matrix and Si equiaxed grains and therefore increases the homogeneity on the treated surface (up to 90%). Santos Macías et al. applied FSP to SLM AlSi10Mg and found that the porosity is reduced from 0.13 to 0.03% (Ref 290). In addition, the FSP treated samples shows a fatigue life up to two orders of magnitude greater than as-built and stress relieved ones. In another work, nano-TiB$_2$/AlSi10Mg composite was successfully enhanced for both tensile and ductile behavior (Ref 291). With slightly reduced tensile strength, FSP treated CSAM composite exhibited improved elongation (16%) and interfacial bonding. Deng et al. adopted FSP (800 *rpm*, 50 *mm/min*, plunge depth = 12.5 *mm*, tilt angle = 2.5°) and subsequent aging (200 °C, oil) to tailor the SLM-fabricated Mg10Gd0.2Zr (G10K) alloy (Ref 87). FSP greatly reduces the average grain size from 26.85 μm of as-built condition to 5.78 μm and increases the hardness by 25% at different age hardening times. FSP can improve the tensile strength and ductility simultaneously while aging (T5) can further promote the YS and UTS with reduced elongation.

Huang et al. utilized FSP (W–Re, 75 mm/min, 400 rpm, 2.5°) to enhance SLM-built Ti6Al4V specimens and found that FSP eliminated the 0.02% porosity in the at-built condition (Ref 288). Although it decreases the UTS from 1261 to 1085 MPa, the fracture strain is significantly improved from 0.21 to 0.65. The specimen after FSP was reported to have a higher mechanical strength than the one treated by HIP at a similar elongation at fracture, and vice versa. Li et al. compared the post-treatments of annealing (500 °C, 4 h, furnace cool), electropulsing (2000 A, 6 s, 590 °C), and FSP (30 mm/min, 1500 rpm, 2.5°) on CSAM-fabricated copper specimens (Ref 289). Figure 28 demonstrates that FSP is the most efficient solid-state process to form superfine equiaxed grains due to dynamic recrystallization than other treatments. Consequently, Fig. 28 also illustrates that FSP treated specimen achieves the best combination in tensile properties (UTS 310 MPa) and elongation (40%). FSP was also integrated on a WAAM system to simultaneously perform deposition and finishing (Ref 346).

3.6.4 Spark Plasma Sintering (SPS). SPS is one of the advanced sintering techniques that involves high energy density, high pressure, and short time for densification of a material. In a study of using UAM to print 4130 steel, post-processing of HIP and SPS are applied to as-built parts to improve the properties (Ref 22). Post-SPS process greatly diminishes the void defects at interlayer regions, leaving only small pores. SPS treatment also leads to the formation of continuous ferrite layer at the interfaces of the samples, which is nucleated from austenite phase due to the small inclusions as preferential sites. Specimens after the SPS post-treatment exhibit shear strength of about twofold higher than that of the as-printed ones. SPS- and HIP-treated samples show significantly higher resistance to shear. SPS has impact on the microhardness but also causes higher scattering in the resulting values.
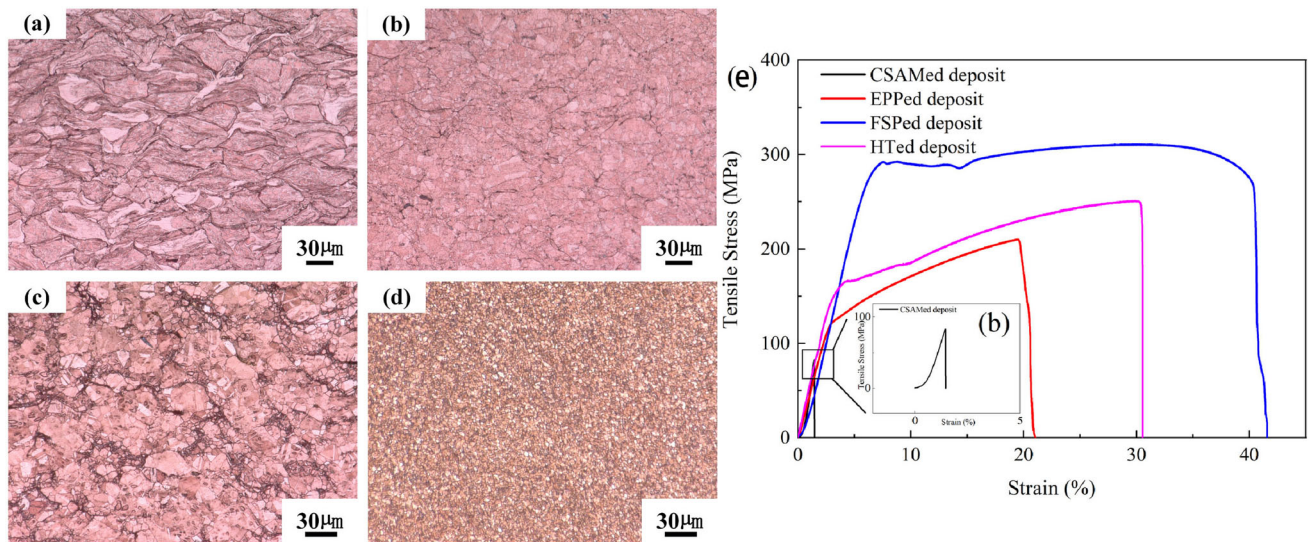
Fig. 28 Optical microscopic images of CASM-fabricated Cu specimens at conditions of (a) as-built, (b) HT (500 °C, 4 h, furnace cool), (c) electro pulse processing (EPP), (d) FSP treated, and (e) stress–strain curves of tested specimens (Ref 289). Reprinted from Surface and Coatings Technology, Vol 409, Wenya Li, Dong Wu, Kaiwei Hu, Yaxin Xu, Xiawei Yang, Yong Zhang, A comparative study on the employment of heat treatment, electric pulse processing and friction stir processing to enhance mechanical properties of cold-spray additive manufactured copper, Article 126,887, Copyright 2021, with permission from Elsevier
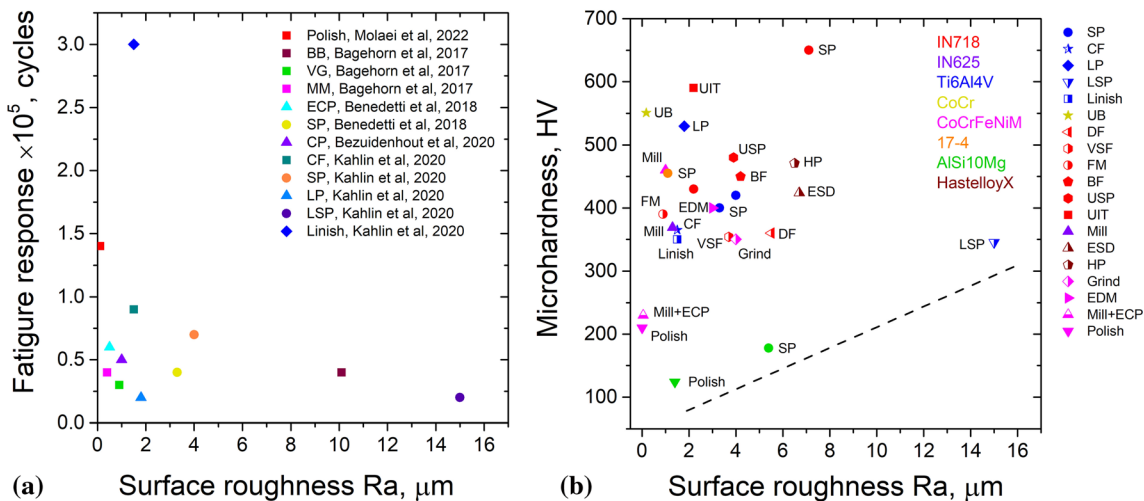
Fig. 29 (a) Fatigue response vs. surface roughness R_a for AM-built Ti6Al4V and (b) microhardness vs. surface roughness R_a for different AM-built alloys with post-treatments (BB: bead blasting, VG: vibratory grinding, MM: micro machining, ECP: electrochemical polishing, SP: shot peening, CP: chemical polishing, CF: centrifugal finish, LP: laser polishing, LSP: laser shock peening, Linish: abrasive finish, UB: ultrasonic burnishing, DF: drag finish, VSF: vibratory surface finish, FM: finish machining, BF: barrel finish, USP: ultrasonic shot peening, UIT: ultrasonic impact treatment, ESD: electrospark deposition, HP: hammer peening)

3.6.5 Summary. Figure 29(a) illustrates a collective plot on surface roughness R_a and corresponding fatigue response of cycle number to failure for Ti6Al4V. An inverse relationship can be observed in the graph, which indicates the necessity of reducing surface roughness in order to have an improved overall fatigue performance. A treated surface with less defective features such as notch, pore, microcrack, etc. is less prone to crack initiation and propagation regardless the usage of thermal post-treatments. On the other hand, the microhardness vs. surface roughness plot in Fig. 29(b) for different alloys shows no clear trending. Nonetheless, the listed treatments flattens the surface and meanwhile improves the hardness of the materials. Although

certain data for same treatment, for example, shot peening (SP), are scattered in the plot for different works, it is still significant to conclude that impact-related treatments with higher energy delivered to the surface lead to higher microhardness than those of abrasion-related ones.

4. Support Removal

Support structure provides the physical presence of the manufactured article on its own weight, to avoid collapse due to

burning or warping. Support structures are inevitable for fabricating in AM techniques. Consequently, a subtractive process is a crucial step for post-processing of the AM component. Support removal consists of cutting off material which surrounds the part as a byproduct of the build process (natural support) and rigid structures which are designed and built to support, restrain or attach the part being built to a build platform (synthetic supports). Popular techniques used for support removal include wire electrical discharge machining (EDM), water jet cutting, and laser cutting (Ref 344, 347, 348). Support removal also contains cleaning the loose powder surrounding the part and remaining inside the part geometry using brushes or compressed air. Powder removal is particularly important for interior passages that cannot be accessed easily with the grit blasting approach. Chemical etching away of powder in passages could require metallurgical studies of interior passage surface behavior. Methods to remove the trapped powders can also be designed such as grit blasting, chemical etching and ultrasonic vibration (Ref 171, 349). Bead blasting involves applying fine beads at a high pressure without damaging the surface and is an inexpensive and quick solution. A combination of grit blasting, vibratory grinding, micro machining and traditional milling is carried out on Ti-6Al-4 V printed by SLM process (Ref 239). A final surface roughness of $R_a = 0.3$ μm can be reached. This allows superior fatigue properties in strength and life. Since planning of subtractive procedure is heavy in labor, automated solutions with computer-aid algorithms for identifying and removing support materials in an AM part are adopted in research and production (Ref 350). Wire EDM, a thermal process, flattens the surface but causes a heat melt layer resulting in the increase of tensile residual stress and surface microhardness. In addition, EDM introduces residual Cu content on the processed surface as contaminant.

5. Minimization of Post-Treatments and Future Outlook

To minimize the cost of post-processing in AM, many approaches have been experimented and applied to improve the as-print part on its surface quality, dimension accuracy, manufacturability, etc. For AM process, adjusting the processing parameters to control the input of the energy density and the solidification process can avoid the necessity of post-processing. For example, optimized process parameters in SLM can produce fine α phase platelets and in Ti6Al4V part, which exhibits hardness greater than 4.0 GPa and eliminates the need for post-process HIP treatment if restricted porosity is achieved (Ref 44). The production of 3D-printed metallic products with smooth surfaces with an appropriate laser output and scan rate could potentially to minimize the amount of post-processing required, such as finishing and polishing (Ref 351). An alternative strategy of point heat source fill is configured in EBM process to produce IN718 alloy on a bulk scale with a controlled grain texture (Ref 90). On the other hand, fine-tuning of the base chemistry and grain boundary strengtheners improves resistance to hot cracking and minimizes the need for a post-build HIP cycle. Introducing TiC nanoparticles in the SLM-built HX alloy part can eliminate hot cracking defects and promote the heterogeneous nucleation (Ref 352).

One of the direct efforts is to attach a post-processing system, for example a 4-axis milling CNC or cold rolling system, with AM machine to allow in situ post-treatment to take place during the printing (Ref 353). Direct additive and subtractive hybrid (DASH) manufacturing system is developed in the concept of combining additive and subtractive process together with integrated operation system to produce high-quality and high-precision metal parts with limited human intervention and reduction in process cycle time (Ref 354). In situ post-processing can be used to improve material properties during layering. High-pressure rolling can be done after each deposition passage in order to refine the microstructure (Ref 282). Multi-pass sliding severe plastic deformation (SPD) and fine particle shot peening (FPSP) have been applied to DMLS-produced AlSi10Mg (Ref 355). In situ SPD reduces the grain size in the surface layer to 1–2 μm and heals the surface crack. In situ heat treating (ISHT) is developed to optimize the IN718 part during the printing process of EBM (Ref 356). The ISHT sample shows similar hardness but reduced tensile strength compared to peak aged conditions. Friction stir burnishing tool can also be applied simultaneously on to an WAAM system to suppress the dendrite growth and anisotropy in microstructure on as-printed 316L stainless steel (Ref 346).

Geometric and shrinkage errors can always be minimized and compensated through slice-based computational algorithm for stereolithography CAD model, for example, like Taguchi-based scaling model and statistical approaches. Many models have been established and explored for the relationship between AM parameters and part shrinkage ratio. In the concept of design for additive manufacturing (DFAM), the effect of parameters like mean cusp height error, sharp corners, support volume can be evaluated in weighted optimization model. As a result, the optimal build orientation can be determined numerically and systematically. Deep learning technique of using artificial neural network (ANN) can be adopted to analyze and generate the geometric compensation to counter the thermal deformations on the as-print geometry (Ref 357). Overhang distortion can also be avoided by creating contact-free support structures (Ref 358).

There are other new developments for additive manufacturing that can potentially provide solutions to the current issues and lead to advancements for higher efficiency and better properties of materials. Blue diode laser with a wavelength of 450 nm has been developed to allow highly reflective metals such as copper and gold to have a much higher adsorption rate of the energy for melting, which conventional near-infrared lasers is not capable of achieving. Without post-treatment for densification, the copper specimen printed with blue laser by SLM can reach a density of 99% after optimization of process parameters (Ref 359). The commercial brand of MELD machine, working as AFSD, can print metallic structure with a size up to 3 m and requires no post-processing like HIP or other heat treatment. For example, the MELD machine produces 7075 Al alloy with wrought-like mechanical properties (Ref 360). Alloy designing strategies have also been explored and applied to combine several manufacturing steps together and avoid post-treatment. Thermodynamic simulation has been used to predict the potential chemical partitioning to mitigate the hot cracking defect in Ni-based superalloy IN738LC fabricated by L-PBF (Ref 361). Hierarchical heterogeneous microstructure, which combines one or more of the following features such as subgrain cellular structures, low-

angle grain boundaries, dislocations, nanolamellae, microscale eutectic colonies, nanoprecipitate, and interstitial solute has been investigated and demonstrated in LPBF-built AlCoCrFe-Ni2.1HEAs, HK30Nb steel, and Ti6Al4V (Ref 362-364). These metallic structures exhibit high strength and high ductility, which has no necessity for further thermal treatment.

6. Conclusions and Limitations

This review summarizes the recent research and development progress on the post-processing techniques that are used to improve the physical, chemical, mechanical and tribological properties of as-built AM metallic structures. It describes the common post-processing methods in detail as well as their mechanisms involved in treating the metal structure. Below are some specific conclusions drawn from this review work:

(1) Internal porosity can only be eliminated through few post-processes like HIP, hot compression, sintering, infiltration, SPS, etc. HIP is most widely applied and studied for various types of metals, which is attributed to its versatility and efficiency in reducing the porosity ($< 0.1\%$) and homogenizing the structure with improved modulus, ductility, and fatigue behavior.

(2) Corresponding heat treatments for the specific metal, such as SR, annealing, or STA should be appropriately chosen to follow HIP to satisfy the requirements on bulk properties like tensile strength, elongation to failure, fatigue, corrosion resistance, etc.

(3) Surface peening through physical shot blast (SP), laser shock (LSP), or high-pressure water jet (cavitation) simply applies plastic deformation and compressive stress to significantly improve the fatigue properties of the specimen. The impact-type treatments such as SP, LSP, and UNSM, which delivers higher level of energy on the surface through either plastic deformation, strain hardening, compressive stress, or work hardening, result in higher microhardness, fatigue performance, and other mechanical properties, while abrasive-type treatments lead to better surface finish but less impact on the mechanical behavior.

(4) Coating techniques (ESD, MS, and ALD) are cost-sensitive and may demand subsequent peening or polishing; however, deposition of a secondary material not only provides positive impact on surface roughness reduction but also is capable to achieve higher hardness, fatigue response, oxidation resistance or wear resistance.

(5) Other advanced treatments (UNSM, EPP, FSP, and SPS) are applicable when specific properties or performance of the metallic structure are expected and are similar to coating techniques in sequence of the complete post-processing solution.

(6) At last, polishing (LP, FL, CP, CHE, ECP, ECM) can be adopted to meet the tightened tolerance on surface finish as the final step. ECP demonstrates the lowest R_a (~ 0.01 μm) that achieved in literature, while LP is capable of reducing the R_a to ~ 0.1 μm with more adaptiveness.

(7) In summary, an optimal post-processing solution of the as-built metallic part can be suggested in the sequence of HIP, heat treatment, surface modification and/or plus any specific treatment required for the application.

One major issue in post-processing of AM metallic structures is that the process is high-cost and time-consuming. Full post-processing solution is currently a costly means to control the anisotropic and heterogeneous microstructure within the article and minimize undesirable features like defects. Therefore, further optimization of a series of post-treatments in sequence is required to reduce the processing time and achieve higher efficiency. The future of additive manufacturing of metallic structures relies on many advanced techniques, such as integration of AI/machine learning to the in situ controlling of the printing at multi-scale of the processed material for optimizing the process-property-performance relationship to minimize post-treatments.

As discussed above, it is difficult for each treatment method to improve or maintain several major properties simultaneously. For example, recrystallization annealing commonly improves ductility but undesirably mitigates the modulus of the structure. Future optimizations are needed to minimize the side-effects of the post-treatment. Furthermore, there is much less work in chemical treatments than that in heat treatments. Their effects in modifying the roughness, dislocation density, grain and crystalline structures are far from sufficient understanding. The synergistic effects of multiple types of post-treatments are also grossly understudied. Therefore, there lacks general guidance on how to select a proper type of post-treatment method.

Lastly, most post-treatments are focused on the survivability and structural applications of metallic structures like mechanical, fatigue and corrosion properties. Studies related to the surface functionalization are still scarce. It is expected that there will be more development of such efforts as AM metallic structures find more and broader applications.

References

1. A. Reichardt et al., Advances in Additive Manufacturing of Metal-Based Functionally Graded Materials, *Int. Mater. Rev.*, 2021, **66**(1), p 1–29. https://doi.org/10.1080/09506608.2019.1709354

2. B. Gadagi and R. Lekurwale, A Review on Advances in 3D Metal Printing, *Mater. Today: Proc.*, 2021, **45**, p 277–283

3. ASTM ISO/ASTM52900-21, *Additive manufacturing — General principles — Fundamentals and vocabulary*, 2021. https://doi.org/10.1520/F3177-21

4. W.E. Frazier, Metal Additive Manufacturing: A Review, *J. Mater. Eng. Perform.*, 2014, **23**(6), p 1917–1928. https://doi.org/10.1007/s11665-014-0958-z

5. L.E. Murr et al., Metal Fabrication by Additive Manufacturing Using Laser and Electron Beam Melting Technologies, *J. Mater. Sci. Technol.*, 2012, **28**(1), p 1–14. https://doi.org/10.1016/S1005-0302(12)60016-4

6. D.D. Gu et al., Laser Additive Manufacturing of Metallic Components: Materials Processes and Mechanisms, *Int. Mater. Rev.*, 2013, **57**(3), p 133–164. https://doi.org/10.1179/1743280411y.0000000014

7. A. du Plessis, I. Yadroitsava, and I. Yadroitsev, Effects of Defects on Mechanical Properties in Metal Additive Manufacturing: A Review Focusing on X-ray Tomography Insights, *Mater. Des.*, 2020 https://doi.org/10.1016/j.matdes.2019.108385

8. S. Mirzababaei and S. Pasebani, A Review on Binder Jet Additive Manufacturing of 316L Stainless Steel, *J. Manuf. Mater. Process.*, 2019 https://doi.org/10.3390/jmmp3030082

9. I. Rishmawi, M. Salarian, and M. Vlasea, Tailoring Green and Sintered Density of Pure Iron Parts Using Binder Jetting Additive Manufacturing, *Addit. Manuf.*, 2018, **24**, p 508–520. https://doi.org/10.1016/j.addma.2018.10.015

10. M. Ziaee and N.B. Crane, Binder Jetting: A Review of Process, Materials, and Methods, *Addit. Manuf.*, 2019, **28**, p 781–801. https://doi.org/10.1016/j.addma.2019.05.031

11. J. Gardan, Additive Manufacturing Technologies: State of the Art and Trends, *Int. J. Prod. Res.*, 2015, **54**(10), p 3118–3132. https://doi.org/10.1080/00207543.2015.1115909

12. Z.C. Cordero et al., Strengthening of Ferrous Binder Jet 3D Printed Components Through Bronze Infiltration, *Addit. Manuf.*, 2017, **15**, p 87–92. https://doi.org/10.1016/j.addma.2017.03.011

13. C. Kenel, N.P.M. Casati, and D.C. Dunand, 3D Ink-Extrusion Additive Manufacturing of CoCrFeNi High-Entropy Alloy Micro-Lattices, *Nat Commun*, 2019, **10**(1), p 904. https://doi.org/10.1038/s41467-019-08763-4

14. B. Barroqueiro et al., Metal Additive Manufacturing Cycle in Aerospace Industry: A Comprehensive Review, *J. Manuf. Mater. Process.*, 2019 https://doi.org/10.3390/jmmp3030052

15. T. He et al., Forming and Mechanical Properties of Wire Arc Additive Manufacture for Marine Propeller Bracket, *J. Manuf. Process.*, 2020, **52**, p 96–105. https://doi.org/10.1016/j.jmapro.2020.01.053

16. S. Yin et al., Cold Spray Additive Manufacturing and Repair: Fundamentals and Applications, *Addit. Manuf.*, 2018, **21**, p 628–650. https://doi.org/10.1016/j.addma.2018.04.017

17. C.R. Cunningham et al., Invited Review Article: Strategies and Processes for High Quality Wire Arc Additive Manufacturing, *Addit. Manuf.*, 2018, **22**, p 672–686. https://doi.org/10.1016/j.addma.2018.06.020

18. T.A. Rodrigues et al., Current Status and Perspectives on Wire and Arc Additive Manufacturing (WAAM), *Materials (Basel)*, 2019 https://doi.org/10.3390/ma12071121

19. W. Li et al., 'Cold Spray +' as a New Hybrid Additive Manufacturing Technology: A Literature Review, *Sci. Technol. Weld. Joining*, 2019, **24**(5), p 420–445. https://doi.org/10.1080/13621718.2019.1603851

20. D. MacDonald et al., Cold Spraying of Armstrong Process Titanium Powder for Additive Manufacturing, *J. Therm. Spray Technol.*, 2016, **26**(4), p 598–609. https://doi.org/10.1007/s11666-016-0489-2

21. A. Miriyev, et al., Ultrasonic Additive Manufacturing of Dissimilar Material Systems: Method, Post-processing and Properties, in *Fraunhofer Direct Digital Manufacturing Conference.* (2016)

22. A. Levy et al., Ultrasonic Additive Manufacturing of Steel: Method, Post-Processing Treatments and Properties, *J. Mater. Process. Technol.*, 2018, **256**, p 183–189. https://doi.org/10.1016/j.jmatprotec.2018.02.001

23. H.Z. Yu et al., Non-Beam-Based Metal Additive Manufacturing Enabled by Additive Friction Stir Deposition, *Scripta Mater.*, 2018, **153**, p 122–130. https://doi.org/10.1016/j.scriptamat.2018.03.025

24. H.Z. Yu and R.S. Mishra, Additive Friction Stir Deposition: A Deformation Processing Route to Metal Additive Manufacturing, *Mater. Res. Lett.*, 2020, **9**(2), p 71–83. https://doi.org/10.1080/21663831.2020.1847211

25. M.A. Gibson et al., 3D Printing Metals Like Thermoplastics: Fused Filament Fabrication of Metallic Glasses, *Mater. Today*, 2018, **21**(7), p 697–702. https://doi.org/10.1016/j.mattod.2018.07.001

26. B. Eberl, et al. Effects of Post-Manufacturing Process on Material Properties of 3D Printed Vessels. in *ASME 2020 Pressure Vessels & Piping Conference.* (2020). https://doi.org/10.1115/pvp2020-21785

27. N. Tuncer and A. Bose, Solid-State Metal Additive Manufacturing: A Review, *JOM*, 2020, **72**(9), p 3090–3111. https://doi.org/10.1007/s11837-020-04260-y

28. G.M. Karthik and H.S. Kim, Heterogeneous Aspects of Additive Manufactured Metallic Parts: A Review, *Metals Mater. Int.*, 2021, **27**(1), p 1–39. https://doi.org/10.1007/s12540-020-00931-2

29. R.I. Revilla et al., Corrosion and Corrosion Protection of Additively Manufactured Aluminium Alloys—A Critical Review, *Materials*, 2020 https://doi.org/10.3390/ma13214804

30. L. Yang, Y. Yang, and W. Di, A Study on the Residual Stress During Selective Laser Melting (SLM) of Metallic Powder, *Int. J. Adv. Manuf. Technol.*, 2016, **87**(1–4), p 1–10

31. A. Fogliatto et al., Correlation Between Porosity and Permeability of Stainless Steel Filters with Gradient Porosity Produced by SLS/SLM, *Rapid Prototyp. J.*, 2020, **26**(1), p 73–81

32. W. Zhang, P. Qin, Z. Wang, C. Yang, L. Kollo, D. Grzesiak, and K.G. Prashanth, Superior Wear Resistance in EBM-Processed TC4 Alloy Compared with SLM and Forged Samples, *Materials*, 2019, **12**(5), p 782

33. P. Edwards and M. Ramulu, Fatigue Performance Evaluation of Selective Laser Melted Ti-6Al-4V, *Mater. Sci. Eng. A*, 2014, **598**, p 327–337. https://doi.org/10.1016/j.msea.2014.01.041

34. M.F. Zäh and S. Lutzmann, Modelling and Simulation of Electron Beam Melting, *Prod. Eng.*, 2010, **4**(1), p 15–23. https://doi.org/10.1007/s11740-009-0197-6

35. A. Dass and A. Moridi, State of the Art in Directed Energy Deposition: From Additive Manufacturing to Materials Design, *Coatings*, 2019 https://doi.org/10.3390/coatings9070418

36. A. Yadollahi and N. Shamsaei, Additive Manufacturing of Fatigue Resistant Materials: Challenges and Opportunities, *Int. J. Fatigue*, 2017, **98**, p 14–31. https://doi.org/10.1016/j.ijfatigue.2017.01.001

37. A. Triantaphyllou et al., Surface Texture Measurement for Additive Manufacturing, *Surf. Topogr. Metrol. Prop.*, 2015 https://doi.org/10.1088/2051-672x/3/2/024002

38. N.N. Kumbhar and A.V. Mulay, Post Processing Methods used to Improve Surface Finish of Products which are Manufactured by Additive Manufacturing Technologies: A Review, *J. Inst. Eng. (India): Series C*, 2016, **99**(4), p 481–487

39. J. Ning et al., Analytical Modeling of Part Distortion in Metal Additive Manufacturing, *Int. J. Adv. Manuf. Technol.*, 2020, **107**(1–2), p 49–57. https://doi.org/10.1007/s00170-020-05065-8

40. R. Molaei, A. Fatemi, and N. Phan, Significance of Hot Isostatic Pressing (HIP) on Multiaxial Deformation and Fatigue Behaviors of Additive Manufactured Ti-6Al-4V Including Build Orientation and Surface Roughness Effects, *Int. J. Fatigue*, 2018, **117**, p 352–370. https://doi.org/10.1016/j.ijfatigue.2018.07.035

41. C. Ye et al., Effects of Post-Processing on the Surface Finish, Porosity, Residual Stresses, and Fatigue Performance of Additive Manufactured Metals: A Review, *J. Mater. Eng. Perform.*, 2021, **30**(9), p 6407–6425. https://doi.org/10.1007/s11665-021-06021-7

42. T. DebRoy et al., Additive Manufacturing of Metallic Components – Process, Structure and Properties, *Prog. Mater. Sci.*, 2018, **92**, p 112–224. https://doi.org/10.1016/j.pmatsci.2017.10.001

43. J.A. Cherry et al., Investigation Into the Effect of Process Parameters on Microstructural and Physical Properties of 316L Stainless Steel Parts by Selective Laser Melting, *Int. J. Adv. Manuf. Technol.*, 2015, **76**(5), p 869–879. https://doi.org/10.1007/s00170-014-6297-2

44. L.E. Murr, Metallurgy Principles Applied to Powder Bed Fusion 3D Printing/Additive Manufacturing of Personalized and Optimized Metal and Alloy Biomedical Implants: An Overview, *J. Market. Res.*, 2020, **9**(1), p 1087–1103. https://doi.org/10.1016/j.jmrt.2019.12.015

45. B. Chalmers, Principles of solidification, *Applied Solid State Physics*. Springer, 1970, p 161–170

46. M.C. Flemings, Solidification Processing, *Metall. Mater. Trans. B*, 1974, **5**(10), p 2121–2134

47. W. Kurz and D.J. Fisher, *Fundamentals of Solidification*, 4th ed. Trans Tech Publications, Zurich, 1998. ISBN: 9783035732399

48. M.A. Meyers and K.K. Chawla, *Mechanical Behavior of Materials*, Cambridge University Press, Cambridge, 2008

49. Y.M. Wang et al., Additively Manufactured Hierarchical Stainless Steels with High Strength and Ductility, *Nat. Mater.*, 2018, **17**(1), p 63–71. https://doi.org/10.1038/nmat5021

50. M.R. Staker and D.L. Holt, The Dislocation Cell Size and Dislocation Density in Copper Deformed at Temperatures Between 25 and 700°C, *Acta Metall.*, 1972, **20**(4), p 569–579. https://doi.org/10.1016/0001-6160(72)90012-0

51. U.F. Kocks and H. Mecking, Physics and Phenomenology of Strain Hardening: The FCC Case, *Prog. Mater Sci.*, 2003, **48**(3), p 171–273. https://doi.org/10.1016/S0079-6425(02)00003-8

52. M. Fisk, J.C. Ion, and L.E. Lindgren, Flow Stress Model for IN718 Accounting for Evolution of Strengthening Precipitates During Thermal Treatment, *Comput. Mater. Sci.*, 2014, **82**, p 531–539. https://doi.org/10.1016/j.commatsci.2013.10.007

53. Z.G. Zhu et al., Hierarchical Microstructure and Strengthening Mechanisms of a CoCrFeNiMn High Entropy Alloy Additively Manufactured by Selective Laser Melting, *Scripta Mater.*, 2018, **154**, p 20–24. https://doi.org/10.1016/j.scriptamat.2018.05.015

54. R.W. Kozar et al., Strengthening Mechanisms in Polycrystalline Multimodal Nickel-Base Superalloys, *Metall. Mater. Trans. A*, 2009, **40**(7), p 1588–1603. https://doi.org/10.1007/s11661-009-9858-5

55. Y.I. Ganor et al., Tailoring Microstructure and Mechanical Properties of Additively-Manufactured Ti6Al4V Using Post Processing, *Materials*, 2021 https://doi.org/10.3390/ma14030658

56. M.-W. Wu et al., Improved Fatigue Endurance Ratio of Additive Manufactured Ti-6Al-4V Lattice by Hot Isostatic Pressing, *Mater.*

Des., 2017, **134**, p 163–170. https://doi.org/10.1016/j.matdes.2017.08.048

57. X. Yan et al., Effect of Heat Treatment on the Phase Transformation and Mechanical Properties of Ti6Al4V Fabricated by Selective Laser Melting, *J. Alloys Compd.*, 2018, **764**, p 1056–1071. https://doi.org/10.1016/j.jallcom.2018.06.076

58. R. Jiang et al., Varied Heat Treatments and Properties of Laser Powder Bed Printed Inconel 718, *Mater. Sci. Eng. A*, 2019, **755**, p 170–180. https://doi.org/10.1016/j.msea.2019.03.103

59. M. Benedetti et al., The Effect of Post-Sintering Treatments on the Fatigue and Biological Behavior of Ti-6Al-4V ELI Parts Made by Selective Laser Melting, *J. Mech. Behav. Biomed. Mater.*, 2017, **71**, p 295–306. https://doi.org/10.1016/j.jmbbm.2017.03.024

60. K. Chadha et al., Effect of Annealing Heat Treatment on the Microstructural Evolution and Mechanical Properties of Hot Isostatic Pressed 316L Stainless Steel Fabricated by Laser Powder Bed Fusion, *Metals*, 2020 https://doi.org/10.3390/met10060753

61. M. Alaña et al., Influence of Relative Density on Quasi-Static and Fatigue Failure of Lattice Structures in Ti6Al4V Produced by Laser Powder Bed Fusion, *Sci. Rep.*, 2021, **11**(1), p 19314. https://doi.org/10.1038/s41598-021-98631-3

62. T. Raza et al., Influence of Heat Treatments on Heat Affected Zone Cracking of Gas Tungsten Arc Welded Additive Manufactured Alloy 718, *Metals*, 2019 https://doi.org/10.3390/met9080881

63. J.-U. Lee et al., Effects of Hot Isostatic Pressing Treatment on the Microstructure and Tensile Properties of Ni-Based Superalloy CM247LC Manufactured by Selective Laser Melting, *Mater. Sci. Eng. A*, 2022, **841**, p 143083. https://doi.org/10.1016/j.msea.2022.143083

64. F. Li et al., Effects of Heat Treatments on Microstructures and Mechanical Properties of Ti6Al4V Alloy Produced by Laser Solid Forming, *Metals*, 2021 https://doi.org/10.3390/met11020346

65. Y. Xu et al., Effect of Annealing Treatments on the Microstructure, Mechanical Properties and Corrosion Behavior of Direct Metal Laser Sintered Ti-6Al-4V, *J. Mater. Eng. Perform.*, 2017, **26**(6), p 2572–2582. https://doi.org/10.1007/s11665-017-2710-y

66. Y. Chen et al., Effects of Heat Treatment on Microstructure and Mechanical Properties of SLMed Sc-Modified AlSi10Mg Alloy, *Prog. Natural Sci. Mater. Int.*, 2021, **31**(5), p 714–721. https://doi.org/10.1016/j.pnsc.2021.08.003

67. H. Bai et al., Effect of Heat Treatment on the Microstructure and Mechanical Properties of Selective Laser-Melted Ti64 and Ti-5Al-5Mo-5V-1Cr-1Fe, *Metals*, 2021 https://doi.org/10.3390/met11040534

68. J. Nguejio et al., Comparison of Microstructure Features and Mechanical Properties for Additive Manufactured and Wrought Nickel Alloys 625, *Mater. Sci. Eng. A*, 2019, **764**, p 138214. https://doi.org/10.1016/j.msea.2019.138214

69. Z. Zhao et al., Microstructural Evolutions and Mechanical Characteristics of Ti/Steel Clad Plates Fabricated Through Cold Spray Additive Manufacturing Followed by Hot-Rolling and Annealing, *Mater. Des.*, 2020, **185**, p 108249. https://doi.org/10.1016/j.matdes.2019.108249

70. A. Yadollahi et al., Effects of Process Time Interval and Heat Treatment on the Mechanical and Microstructural Properties of Direct Laser Deposited 316L Stainless Steel, *Mater. Sci. Eng. A*, 2015, **644**, p 171–183. https://doi.org/10.1016/j.msea.2015.07.056

71. X. Chen et al., Effect of Heat Treatment on Microstructure, Mechanical and Corrosion Properties of Austenitic Stainless Steel 316L Using Arc Additive Manufacturing, *Mater. Sci. Eng. A*, 2018, **715**, p 307–314. https://doi.org/10.1016/j.msea.2017.10.002

72. Z. Tong et al., Laser Additive Manufacturing of FeCrCoMnNi High-Entropy Alloy: Effect of Heat Treatment on Microstructure, Residual Stress and Mechanical Property, *J. Alloys Compd.*, 2019, **785**, p 1144–1159. https://doi.org/10.1016/j.jallcom.2019.01.213

73. X. Wang and K. Chou, The Effects of Stress Relieving Heat Treatment on the Microstructure and Residual Stress of Inconel 718 Fabricated by Laser Metal Powder Bed Fusion Additive Manufacturing Process, *J. Manuf. Process.*, 2019, **48**, p 154–163. https://doi.org/10.1016/j.jmapro.2019.10.027

74. J. Lei et al., Effects of Heat Treatment on the Microstructure and Mechanical Properties of Selective Laser Melting 316L Stainless Steel, *Shock. Vib.*, 2021 https://doi.org/10.1155/2021/6547213

75. Y. Zhao and C. Ding, Effect of Heat Treatment on Microstructure and Properties of 24CrNiMo Alloy Steel Formed by Selective Laser Melting (SLM), *Materials*, 2021 https://doi.org/10.3390/ma14030631

76. S. Santa-aho et al., Additive Manufactured 316L Stainless-Steel Samples: Microstructure, Residual Stress and Corrosion Characteristics after Post-Processing, *Metals*, 2021 https://doi.org/10.3390/met11020182

77. V.D. Divya et al., Microstructure of Selective Laser Melted CM247LC Nickel-Based Superalloy and Its Evolution Through Heat Treatment, *Mater. Charact.*, 2016, **114**, p 62–74. https://doi.org/10.1016/j.matchar.2016.02.004

78. K.-Y. Feng et al., Microstructure and Phase Transformation on the Surface of Inconel 718 Alloys Fabricated by SLM Under 1050°C Solid Solution + Double Ageing, *Vacuum*, 2017, **145**, p 112–115. https://doi.org/10.1016/j.vacuum.2017.08.044

79. T.G. Gallmeyer et al., Knowledge of Process-Structure-Property Relationships to Engineer Better Heat Treatments for Laser Powder Bed Fusion Additive Manufactured Inconel 718, *Addit. Manuf.*, 2020, **31**, p 100977. https://doi.org/10.1016/j.addma.2019.100977

80. W. Huang et al., Heat Treatment of Inconel 718 Produced by Selective Laser Melting: Microstructure and Mechanical Properties, *Mater. Sci. Eng. A*, 2019, **750**, p 98–107. https://doi.org/10.1016/j.msea.2019.02.046

81. K. Żaba et al., Effect of Multi-Variant Thermal Treatment on Microstructure Evolution and Mechanical Properties of AlSi10Mg Processed by Direct Metal Laser Sintering and Casting, *Materials*, 2022 https://doi.org/10.3390/ma15030974

82. D. Zhang et al., Effect of Standard Heat Treatment on the Microstructure and Mechanical Properties of Selective Laser Melting Manufactured Inconel 718 Superalloy, *Mater. Sci. Eng. A*, 2015, **644**, p 32–40. https://doi.org/10.1016/j.msea.2015.06.021

83. A.R. Balachandramurthi et al., Additive Manufacturing of Alloy 718 via Electron Beam Melting: Effect of Post-Treatment on the Microstructure and the Mechanical Properties, *Materials (Basel)*, 2018 https://doi.org/10.3390/ma12010068

84. A. Mostafaei et al., Microstructural Evolution and Mechanical Properties of Differently Heat-Treated Binder Jet Printed Samples from Gas- and water-Atomized Alloy 625 Powders, *Acta Mater.*, 2017, **124**, p 280–289. https://doi.org/10.1016/j.actamat.2016.11.021

85. S. Bagherifard et al., On the Fatigue Strength Enhancement of Additive Manufactured AlSi10Mg Parts by Mechanical and Thermal Post-Processing, *Mater. Des.*, 2018, **145**, p 28–41. https://doi.org/10.1016/j.matdes.2018.02.055

86. Q. Han and Y. Jiao, Effect of Heat Treatment and Laser Surface Remelting on AlSi10Mg Alloy Fabricated by Selective Laser Melting, *Int. J. Adv. Manuf. Technol.*, 2019, **102**(9), p 3315–3324. https://doi.org/10.1007/s00170-018-03272-y

87. Q. Deng et al., Influence of Friction Stir Processing and Aging Heat Treatment on Microstructure and Mechanical Properties of Selective Laser Melted Mg-Gd-Zr Alloy, *Addit. Manuf.*, 2021, **44**, p 102036. https://doi.org/10.1016/j.addma.2021.102036

88. C. He et al., Enhancing the Mechanical Performance of Al-Zn-Mg Alloy Builds Fabricated Via Underwater Friction Stir Additive Manufacturing and Post-Processing Aging, *J. Mater. Sci. Technol.*, 2022, **108**, p 26–36. https://doi.org/10.1016/j.jmst.2021.08.050

89. Y.-J. Kang et al., Effect of Post-Treatment on the Microstructure and High-Temperature Oxidation Behaviour of Additively Manufactured Inconel 718 Alloy, *Corros. Sci.*, 2019 https://doi.org/10.1016/j.corsci.2019.06.030

90. M.M. Kirka et al., Mechanical Behavior of Post-Processed Inconel 718 Manufactured Through the Electron Beam Melting Process, *Mater. Sci. Eng. A*, 2017, **680**, p 338–346. https://doi.org/10.1016/j.msea.2016.10.069

91. B. Shassere et al., Correlation of Microstructure to Creep Response of Hot Isostatically Pressed and Aged Electron Beam Melted Inconel 718, *Metall. Mater. Trans. A*, 2018, **49**(10), p 5107–5117. https://doi.org/10.1007/s11661-018-4812-z

92. B. Sutton et al., Heat Treatment of Alloy 718 Made by Additive Manufacturing for Oil and Gas Applications, *JOM*, 2019, **71**(3), p 1134–1143. https://doi.org/10.1007/s11837-018-03321-7

93. G. Marchese et al., Microstructural Evolution of Post-Processed Hastelloy X Alloy Fabricated by Laser Powder Bed Fusion, *Materials (Basel)*, 2019 https://doi.org/10.3390/ma12030486

94. H. Peng et al., Microstructure, Mechanical Properties and Cracking Behaviour in a γ′-Precipitation Strengthened Nickel-Base Superalloy Fabricated by Electron Beam Melting, *Mater. Des.*, 2018, **159**, p 155–169. https://doi.org/10.1016/j.matdes.2018.08.054

95. Zhou, N., et al., Development of a New Alumina-Forming Crack-Resistant High-γ′ Fraction Ni-Base Superalloy for Additive Manufacturing, in *Superalloys 2020*. p. 1046–1054 (2020)

96. T. Do, P. Kwon, and C.S. Shin, Process Development Toward Full-Density Stainless Steel Parts with Binder Jetting Printing, *Int. J. Mach. Tools Manuf.*, 2017, **121**, p 50–60. https://doi.org/10.1016/j.ijmachtools.2017.04.006

97. D. Huber, L. Vogel, and A. Fischer, The Effects of Sintering Temperature and Hold Time on Densification, Mechanical Properties and Microstructural Characteristics of Binder Jet 3D Printed 17–4 PH Stainless Steel, *Addit. Manuf.*, 2021, **46**, p 102114. https://doi.org/10.1016/j.addma.2021.102114

98. S.L. Lu et al., The Combined Influence of Elevated Pre-Sintering and Subsequent Bronze Infiltration on the Microstructures and Mechanical Properties of 420 Stainless Steel Additively Manufactured Via Binder Jet Printing, *Addit. Manuf.*, 2020, **34**, p 101266. https://doi.org/10.1016/j.addma.2020.101266

99. C. Xu et al., Solvent-Cast Based Metal 3D Printing and Secondary Metallic Infiltration, *J. Mater. Chem. C*, 2017, **5**(40), p 10448–10455. https://doi.org/10.1039/C7TC02884A

100. S. Cui et al., Detailed Assessments of Tribological Properties of Binder Jetting Printed Stainless Steel and Tungsten Carbide Infiltrated with Bronze, *Wear*, 2021, **477**, p 203788. https://doi.org/10.1016/j.wear.2021.203788

101. X.Y. Liu et al., Microstructural Evolution of Al-Cu-Mg-Ag Alloy During Homogenization, *J. Alloys Compd.*, 2009, **484**(1), p 790–794. https://doi.org/10.1016/j.jallcom.2009.05.046

102. S. Liu and H. Guo, A Review of SLMed Magnesium Alloys: Processing, Properties Alloying Elements and Postprocessing, *Metals*, 2020 https://doi.org/10.3390/met10081073

103. A. Uriondo, M. Esperon-Miguez, and S. Perinpanayagam, The Present and Future of Additive Manufacturing in the Aerospace Sector: A Review of Important Aspects, *Proc. Inst. Mech. Eng. Part G J. Aerospa. Eng.*, 2015, **229**(11), p 2132–2147. https://doi.org/10.1177/0954410014568797

104. G.A. Ravi et al., Direct Laser Fabrication of Three Dimensional Components Using SC420 Stainless Steel, *Mater. Des.*, 2013, **47**, p 731–736. https://doi.org/10.1016/j.matdes.2012.12.062

105. M.T. Tran et al., Effect of Hot Isostatic Pressing on the Cryogenic Mechanical Properties of CrCoNi Medium Entropy Alloy Processed by Direct Energy Deposition, *Mater. Sci. Eng. A*, 2021, **828**, p 142110. https://doi.org/10.1016/j.msea.2021.142110

106. A. Deshpande et al., Effect of Post Processing Heat Treatment Routes on Microstructure and Mechanical Property Evolution of Haynes 282 Ni-Based Superalloy Fabricated with Selective Laser Melting (SLM), *Metals*, 2020 https://doi.org/10.3390/met10050629

107. Y.Y. Kaplanskii et al., Influence of Aging and HIP Treatment on the Structure and Properties of NiAl-Based Turbine Blades Manufactured by Laser Powder Bed Fusion, *Addit. Manuf.*, 2020 https://doi.org/10.1016/j.addma.2019.100999

108. J. Joseph et al., Effect of Hot Isostatic Pressing on the Microstructure and Mechanical Properties of Additive Manufactured AlxCoCrFeNi High Entropy Alloys, *Mater. Sci. Eng. A*, 2018, **733**, p 59–70. https://doi.org/10.1016/j.msea.2018.07.036

109. H. Wang et al., Oxidation Behavior of Hastelloy X Alloy Fabricated by Selective Laser Melting and Subsequent Hot Isostatic Pressing Treatment, *Adv. Eng. Mater.*, 2022, **24**(11), p 2200369. https://doi.org/10.1002/adem.202200369

110. T. Han et al., Effect of Preheat Temperature and Post-Process Treatment on the Microstructure and Mechanical Properties of Stainless Steel 410 Made Via Ultrasonic Additive Manufacturing, *Mater. Sci. Eng. A*, 2020 https://doi.org/10.1016/j.msea.2019.138457

111. R. Cunningham et al., Analyzing the Effects of Powder and Post-Processing on Porosity and Properties of Electron Beam Melted Ti-6Al-4V, *Mater. Res. Lett.*, 2017, **5**(7), p 516–525. https://doi.org/10.1080/21663831.2017.1340911

112. K. Karami et al., Continuous and Pulsed Selective Laser Melting of Ti6Al4V Lattice Structures: Effect of Post-Processing on Microstructural Anisotropy and Fatigue Behaviour, *Addit. Manuf.*, 2020 https://doi.org/10.1016/j.addma.2020.101433

113. R. Molaei and A. Fatemi, Crack Paths in Additive Manufactured Metallic Materials Subjected to Multiaxial Cyclic Loads Including Surface Roughness, HIP, and Notch Effects, *Int. J. Fatigue*, 2019, **124**, p 558–570. https://doi.org/10.1016/j.ijfatigue.2019.03.007

114. A. Leon et al., The Effect of Hot Isostatic Pressure on the Corrosion Performance of Ti-6Al-4 V Produced by An Electron-Beam Melting Additive Manufacturing Process, *Addit. Manuf.*, 2020 https://doi.org/10.1016/j.addma.2020.101039

115. V. Popov et al., Effect of Hot Isostatic Pressure Treatment on the Electron-Beam Melted Ti-6Al-4V specimens, *Procedia Manuf.*, 2018, **21**, p 125–132. https://doi.org/10.1016/j.promfg.2018.02.102

116. N. Eshawish et al., Microstructure and Mechanical Properties of Ti-6Al-4V Manufactured by Selective Laser Melting after Stress Relieving, Hot Isostatic Pressing Treatment, and Post-Heat Treatment, *J. Mater. Eng. Perform.*, 2021, **30**(7), p 5290–5296. https://doi.org/10.1007/s11665-021-05753-w

117. P. Nandwana, et al. *Optimizing Parameters for Post-Processing of Ti-6Al-4V Components Fabricated by Additive Manufacturing for Superior Performance*. Oak Ridge National Lab. (ORNL), Oak Ridge, TN (United States). p. Medium: ED; Size: 17 p. (2018)

118. M.J. Bermingham et al., Optimising the Mechanical Properties of Ti-6Al-4V Components Produced by Wire + Arc Additive Manufacturing with Post-Process Heat Treatments, *J. Alloys Compd.*, 2018, **753**, p 247–255. https://doi.org/10.1016/j.jallcom.2018.04.158

119. A. Travyanov et al., Manufacturing of Ti6Al4V Alloy Part Reinforced by Silicon Carbide Fibers by Laser Powder Bed Fusion with Following Hot Isostatic Pressing, *Int. J. Adv. Manuf. Technol.*, 2022, **119**(1), p 1331–1341. https://doi.org/10.1007/s00170-021-08307-5

120. M. Seifi et al., Effects of HIP on Microstructural Heterogeneity, Defect Distribution and Mechanical Properties of Additively Manufactured EBM Ti-48Al-2Cr-2Nb, *J. Alloys Compd.*, 2017, **729**, p 1118–1135. https://doi.org/10.1016/j.jallcom.2017.09.163

121. I. Sizova et al., A Study on Hot-Working as Alternative Post-Processing Method for Titanium Aluminides Built by Laser Powder Bed Fusion and Electron Beam Melting, *J. Mater. Process. Technol.*, 2021 https://doi.org/10.1016/j.jmatprotec.2020.117024

122. A. Cutolo et al., Influence of Layer Thickness and Post-Process Treatments on the Fatigue Properties of CoCr Scaffolds Produced by Laser Powder Bed Fusion, *Addit. Manuf.*, 2018, **23**, p 498–504. https://doi.org/10.1016/j.addma.2018.07.008

123. L.E. Murr, Metallurgy of Additive Manufacturing: Examples from Electron Beam Melting, *Addit. Manuf.*, 2015, **5**, p 40–53. https://doi.org/10.1016/j.addma.2014.12.002

124. S. Liu and H. Guo, Influence of Hot Isostatic Pressing (HIP) on Mechanical Properties of Magnesium Alloy Produced by Selective Laser Melting (SLM), *Mater. Lett.*, 2020, **265**, p 127463. https://doi.org/10.1016/j.matlet.2020.127463

125. W. Schneller et al., Effect of HIP Treatment on Microstructure and Fatigue Strength of Selectively Laser Melted AlSi10Mg, *J. Manuf. Mater. Process.*, 2019 https://doi.org/10.3390/jmmp3010016

126. T. Hirata, T. Kimura, and T. Nakamoto, Effects of Hot Isostatic Pressing and Internal Porosity on the Performance of Selective Laser Melted AlSi10Mg Alloys, *Mater. Sci. Eng. A*, 2020 https://doi.org/10.1016/j.msea.2019.138713

127. W.H. Kan et al., Factors that Affect the Properties of Additively-Manufactured AlSi10Mg: Porosity Versus Microstructure, *Addit. Manuf.*, 2019 https://doi.org/10.1016/j.addma.2019.100805

128. I. Rosenthal, R. Shneck, and A. Stern, Heat Treatment Effect on the Mechanical Properties and Fracture Mechanism in AlSi10Mg Fabricated by Additive Manufacturing Selective Laser Melting Process, *Mater. Sci. Eng. A*, 2018, **729**, p 310–322. https://doi.org/10.1016/j.msea.2018.05.074

129. N.O. Larrosa et al., Linking Microstructure and Processing Defects to Mechanical Properties of Selectively Laser Melted AlSi10Mg Alloy, *Theoret. Appl. Fract. Mech.*, 2018, **98**, p 123–133. https://doi.org/10.1016/j.tafmec.2018.09.011

130. A.B. Spierings et al., Microstructure Characterization of SLM-Processed Al-Mg-Sc-Zr Alloy in the Heat Treated and HIPed

Condition, *Addit. Manuf.*, 2018, **20**, p 173–181. https://doi.org/10.1016/j.addma.2017.12.011

131. M.N. Gussev et al., Influence of Hot Isostatic Pressing on the Performance of Aluminum Alloy Fabricated by Ultrasonic Additive Manufacturing, *Scripta Mater.*, 2018, **145**, p 33–36. https://doi.org/10.1016/j.scriptamat.2017.10.004

132. M.L. Montero-Sistiaga et al., Microstructure and Mechanical Properties of Hastelloy X produced by HP-SLM (High Power Selective Laser Melting), *Mater. Des.*, 2019 https://doi.org/10.1016/j.matdes.2019.107598

133. S. He, S. Guo, and Y. Xu, Anisotropic Stress Rupture Properties-Microstructure Relationships in SLM Inconel 718 Alloy, *Metall. Mater. Trans. A*, 2022 https://doi.org/10.1007/s11661-022-06872-2

134. J. Schneider, Comparison of Microstructural Response to Heat Treatment of Inconel 718 Prepared by Three Different Metal Additive Manufacturing Processes, *JOM*, 2020, **72**(3), p 1085–1091. https://doi.org/10.1007/s11837-020-04021-x

135. W. Tillmann et al., Functional Encapsulation of Laser Melted Inconel 718 by Arc-PVD and HVOF for Post Compacting by Hot Isostatic Pressing, *Powder Metall.*, 2015, **58**(4), p 259–264. https://doi.org/10.1179/0032589915Z.000000000250

136. Z. Xu et al., Effect of Post Processing on the Creep Performance of Laser Powder Bed Fused Inconel 718, *Addit. Manuf.*, 2018, **24**, p 486–497. https://doi.org/10.1016/j.addma.2018.10.027

137. S. Goel et al., Effect of Post-Treatments Under Hot Isostatic Pressure on Microstructural Characteristics of EBM-Built Alloy 718, *Addit. Manuf.*, 2019, **28**, p 727–737. https://doi.org/10.1016/j.addma.2019.06.002

138. J.R. Poulin, V. Brailovski, and P. Terriault, Long Fatigue Crack Propagation Behavior of Inconel 625 Processed by Laser Powder Bed Fusion: Influence of Build Orientation and Post-Processing Conditions, *Int. J. Fatigue*, 2018, **116**, p 634–647. https://doi.org/10.1016/j.ijfatigue.2018.07.008

139. Z. Zhang et al., Influence of Heat Treatment on Microstructures and Mechanical Properties of K447A Cladding Layers Obtained by Laser Solid Forming, *J. Alloys Compd.*, 2019, **790**, p 703–715. https://doi.org/10.1016/j.jallcom.2019.03.136

140. X. Zhao et al., The Effect of Hot Isostatic Pressing on Crack Healing, Microstructure, Mechanical Properties of Rene88DT Superalloy Prepared by Laser Solid Forming, *Mater. Sci. Eng. A*, 2009, **504**(1), p 129–134. https://doi.org/10.1016/j.msea.2008.12.024

141. A.E.-M.A. Mohamed et al., Magnetic Shielding Promotion Via the Control of Magnetic Anisotropy and Thermal Post Processing in Laser Powder Bed Fusion Processed NiFeMo-Based Soft Magnet, *Addit. Manuf.*, 2020 https://doi.org/10.1016/j.addma.2020.101079

142. I. Konyashin et al., Additive Manufacturing of WC-13%Co by Selective Electron Beam Melting: Achievements and Challenges, *Int. J. Refract Metal Hard Mater.*, 2019 https://doi.org/10.1016/j.ijrmhm.2019.105028

143. N. Ku et al., Additive Manufacturing of Cemented Tungsten Carbide with a Cobalt-Free Alloy Binder by Selective Laser Melting for High-Hardness Applications, *JOM*, 2019, **71**(4), p 1535–1542. https://doi.org/10.1007/s11837-019-03366-2

144. B. Almangour and J. Yang, Effect of post-processing on the microstructure and mechanical properties of ultra-low carbon steel fabricated by selective laser melting. in *Solid Freeform Fabrication Symposium*. (2015)

145. M. Åsberg et al., Influence of Post Treatment on Microstructure, Porosity and Mechanical Properties of Additive Manufactured H13 Tool Steel, *Mater. Sci. Eng. A*, 2019, **742**, p 584–589. https://doi.org/10.1016/j.msea.2018.08.046

146. B. AlMangour, D. Grzesiak, and J.-M. Yang, Selective Laser Melting of TiB2/316L Stainless Steel Composites: The Roles of Powder Preparation and Hot Isostatic Pressing Post-Treatment, *Powder Technol.*, 2017, **309**, p 37–48. https://doi.org/10.1016/j.powtec.2016.12.073

147. S. Dadbakhsh and L. Hao, Effect of Hot Isostatic Pressing (HIP) on Al Composite Parts Made from Laser Consolidated Al/Fe2O3 Powder Mixtures, *J. Mater. Process. Technol.*, 2012, **212**(11), p 2474–2483. https://doi.org/10.1016/j.jmatprotec.2012.06.016

148. A. Kumar et al., Effects of Hot Isostatic Pressing on Copper Parts Fabricated via Binder Jetting, *Procedia Manuf.*, 2017, **10**, p 935–944. https://doi.org/10.1016/j.promfg.2017.07.084

149. H.V. Atkinson and S. Davies, Fundamental Aspects of Hot Isostatic Pressing: An Overview, *Metall. Mater. Trans. A*, 2000, **31**(12), p 2981–3000. https://doi.org/10.1007/s11661-000-0078-2

150. K. Osakada and M. Shiomi, Flexible manufacturing of metallic products by selective laser melting of powder, *Int. J. Mach. Tools Manuf.*, 2006, **46**(11), p 1188–1193. https://doi.org/10.1016/j.ijmachtools.2006.01.024

151. F. Memu et al., Effect of Machining and Hot Isostatic Pressing on Mechanical Properties of Ti-6Al-4V Manufactured by Electron Beam Melting, in *1st International Conference on Advances in Mechanical and Mechatronics Engineering*, 2018

152. Y. Holovenko, L. Kollo, M. Jõeleht, M. Pohlak and R. Veinthal, Effect of Hot Isostatic Pressing on Cellular Lattice Structures Obtained by Selective Laser Melting. in *European Congress and Exhibition on Powder Metallurgy. European PM Conference Proceedings*. The European Powder Metallurgy Association, 2016, p 1–6

153. H. Chen, D. Zhang, and Q. Ye, Large-Scale and Industrialized HIP Equipment for the Densification of Additive Manufactured Parts, *Mater. Res. Proc.*, 2019 https://doi.org/10.21741/9781644900031-7

154. W. Tillmann et al., Hot Isostatic Pressing of IN718 Components Manufactured by Selective Laser Melting, *Addit. Manuf.*, 2017, **13**, p 93–102. https://doi.org/10.1016/j.addma.2016.11.006

155. T. Persenot et al., Enhancing the Tensile Properties of EBM as-Built Thin Parts: Effect of HIP and Chemical Etching, *Mater. Charact.*, 2018, **143**, p 82–93. https://doi.org/10.1016/j.matchar.2018.01.035

156. X. Shui et al., Effects of Post-Processing on Cyclic Fatigue Response of A Titanium Alloy Additively Manufactured by Electron Beam Melting, *Mater. Sci. Eng. A*, 2017, **680**, p 239–248. https://doi.org/10.1016/j.msea.2016.10.059

157. A. Sola and A. Nouri, Microstructural Porosity in Additive Manufacturing: The Formation and Detection of Pores in Metal Parts Fabricated by Powder Bed Fusion, *J. Adv. Manuf. Process.*, 2019 https://doi.org/10.1002/amp2.10021

158. R.W. Fonda et al., The Effects of Post-processing in Additively Manufactured 316L Stainless Steels, *Metall. Mater. Trans. A*, 2020, **51**(12), p 6560–6573. https://doi.org/10.1007/s11661-020-06039-x

159. L.-C. Zhang et al., Additive Manufacturing of Titanium Alloys by Electron Beam Melting: A Review, *Adv. Eng. Mater.*, 2018 https://doi.org/10.1002/adem.201700842

160. W. Sames, *Additive Manufacturing of Inconel 718 Using Electron Beam Melting: Processing, Post-Processing, & Mechanical Properties*, Texas A&M University, Texas, 2015

161. P. Nandwana et al., Electron Beam Melting of Inconel 718: Effects of Processing and Post-Processing, *Mater. Sci. Technol.*, 2018, **34**(5), p 612–619. https://doi.org/10.1080/02670836.2018.1424379

162. P. Stoyanov et al., Microstructural and Mechanical Characterization of Mo-containing Stellite Alloys Produced by three Dimensional Printing, *Procedia CIRP*, 2016, **45**, p 167–170. https://doi.org/10.1016/j.procir.2016.02.358

163. A. Yegyan Kumar et al., Impacts of Process-Induced Porosity on Material Properties of Copper Made by Binder Jetting Additive Manufacturing, *Mater. Des.*, 2019 https://doi.org/10.1016/j.matdes.2019.108001

164. K. Mertova, J. Dzugan, and M. Roudnicka, Fatigue Properties of SLM-Produced Ti6Al4V with Various Post-Processing Processes. in *IOP Conference Series: Materials Science and Engineering*, (2018). https://doi.org/10.1088/1757-899x/461/1/012052

165. A.H. Chern et al., A Review on the Fatigue Behavior of Ti-6Al-4V Fabricated by Electron Beam Melting Additive Manufacturing, *Int. J. Fatigue*, 2019, **119**, p 173–184. https://doi.org/10.1016/j.ijfatigue.2018.09.022

166. M. Nakatani et al., Effect of Surface Roughness on Fatigue Strength of Ti-6Al-4V Alloy Manufactured by Additive Manufacturing, *Procedia Struct. Integrity*, 2019, **19**, p 294–301. https://doi.org/10.1016/j.prostr.2019.12.032

167. B. Vayssette et al., Numerical Modelling of Surface Roughness Effect on the Fatigue Behavior of Ti-6Al-4V Obtained by Additive Manufacturing, *Int. J. Fatigue*, 2019, **123**, p 180–195. https://doi.org/10.1016/j.ijfatigue.2019.02.014

168. D.T. Ardi et al., Effects of Post-Processing Route on Fatigue Performance of Laser Powder Bed Fusion Inconel 718, *Addit. Manuf.*, 2020 https://doi.org/10.1016/j.addma.2020.101442

169. R. Molaei, A. Fatemi, and N. Phan, Multiaxial Fatigue of LB-PBF Additive Manufactured 17–4 PH stainless Steel Including the Effects

169. ... of Surface Roughness and HIP Treatment and Comparisons with the Wrought Alloy, *Int. J. Fatigue*, 2020, **137**, p 105646. https://doi.org/10.1016/j.ijfatigue.2020.105646

170. W.A. Grell et al., Effect of Powder Oxidation on the Impact Toughness of Electron Beam Melting Ti-6Al-4V, *Addit. Manuf.*, 2017, **17**, p 123–134. https://doi.org/10.1016/j.addma.2017.08.002

171. Y. Zhong et al., Additive Manufacturing of 316L Stainless Steel by Electron Beam Melting for Nuclear Fusion Applications, *J. Nucl. Mater.*, 2017, **486**, p 234–245. https://doi.org/10.1016/j.jnucmat.2016.12.042

172. T.B. Sercombe and G.B. Schaffer, On the Role of Magnesium and Nitrogen in the Infiltration of Aluminium by Aluminium for Rapid Prototyping Applications, *Acta Mater.*, 2004, **52**(10), p 3019–3025. https://doi.org/10.1016/j.actamat.2004.03.004

173. C.L. Cramer et al., Infiltration Studies of Additive Manufacture of WC with Co Using Binder Jetting and Pressureless Melt Method, *Addit. Manuf.*, 2019, **28**, p 333–343. https://doi.org/10.1016/j.addma.2019.04.009

174. R. Berger et al., Numerical Modelling of Infiltration of Al Into Additive Manufactured Fe Preforms in Order to Obtain Fe-Al Intermetallics. in *IOP Conference Series: Materials Science and Engineering*, (2019). https://doi.org/10.1088/1757-899x/529/1/012014

175. D. Wang et al., W-ZrC Composites Prepared by Reactive Melt Infiltration of Zr2Cu Alloy into Partially Carburized W Preforms, *Int. J. Refract Metal Hard Mater.*, 2017, **67**, p 125–128. https://doi.org/10.1016/j.ijrmhm.2017.05.005

176. R.M. German, Sintering Trajectories: Description on How Density, Surface Area, and Grain Size Change, *JOM*, 2016, **68**(3), p 878–884. https://doi.org/10.1007/s11837-015-1795-8

177. R.M. German, *Powder metallurgy science.* Metal Powder Industries Federation, 105 College Rd. E, Princeton, N. J. 08540, U. S. A, 1984. 279, (1984)

178. R. Haynes, A Study of the Effect of Porosity Content on the Ductility of Sintered Metals, *Powder Metall.*, 1977, **20**(1), p 17–20. https://doi.org/10.1179/pom.1977.20.1.17

179. G.P. Martins, D.L. Olson, and G.R. Edwards, Modeling of Infiltration Kinetics for Liquid Metal Processing of Composites, *Metall. Trans. B*, 1988, **19**(1), p 95–101. https://doi.org/10.1007/BF02666495

180. F. Xie et al., Structural and Mechanical Characteristics of Porous 316L Stainless Steel Fabricated by Indirect Selective Laser Sintering, *J. Mater. Process. Technol.*, 2013, **213**(6), p 838–843. https://doi.org/10.1016/j.jmatprotec.2012.12.014

181. D.B. Vennilaa, G. Karuppusami, and P. Senthil, Analysis of Different Infiltration Effect for Selective Laser Sintering Process Through Taguchi Method, *Aust. J. Mech. Eng.*, 2016, **14**(3), p 217–223. https://doi.org/10.1080/14484846.2015.1093255

182. S. Kumar and J.P. Kruth, Effect of Bronze Infiltration Into Laser Sintered Metallic Parts, *Mater. Des.*, 2007, **28**(2), p 400–407. https://doi.org/10.1016/j.matdes.2005.09.016

183. S. Yin et al., Annealing Strategies for Enhancing Mechanical Properties of Additively Manufactured 316L Stainless Steel Deposited by Cold Spray, *Surf. Coat. Technol.*, 2019, **370**, p 353–361. https://doi.org/10.1016/j.surfcoat.2019.04.012

184. D. Junker et al., Investigation of Heat Treatment Strategies for Additively-Manufactured Tools of X37CrMoV5-1, *Metals*, 2018 https://doi.org/10.3390/met8100854

185. X. Wang et al., Microstructure and Mechanical Behavior of Additive Manufactured Cr-Ni-V Low Alloy Steel in Different Heat Treatment, *Vacuum*, 2020, **175**, p 109216. https://doi.org/10.1016/j.vacuum.2020.109216

186. Y. Kok et al., Anisotropy and Heterogeneity of Microstructure and Mechanical Properties in Metal Additive Manufacturing: A Critical Review, *Mater. Des.*, 2018, **139**, p 565–586. https://doi.org/10.1016/j.matdes.2017.11.021

187. L. Dowling et al., A Review of Critical Repeatability and Reproducibility Issues in Powder Bed Fusion, *Mater. Des.*, 2020 https://doi.org/10.1016/j.matdes.2019.108346

188. S. Kang et al., Effects of Recrystallization Annealing Temperature on Carbide Precipitation, Microstructure, and Mechanical Properties in Fe–18Mn–0.6C–1.5Al TWIP Steel, *Mater. Sci. Eng. A*, 2010, **527**(3), p 745–751. https://doi.org/10.1016/j.msea.2009.08.048

189. L. Dong et al., Dynamic Recrystallization and Grain Growth Behavior of 20SiMn Low Carbon Alloy Steel, *Tsinghua Sci. Technol.*, 2008, **13**(5), p 609–613. https://doi.org/10.1016/S1007-0214(08)70097-X

190. A.H. Chokshi et al., On the Validity of the Hall-Petch Relationship in Nanocrystalline Materials, *Scr. Metall.*, 1989, **23**(10), p 1679–1683. https://doi.org/10.1016/0036-9748(89)90342-6

191. C.S. Pande and K.P. Cooper, Nanomechanics of Hall-Petch Relationship in Nanocrystalline Materials, *Prog. Mater. Sci.*, 2009, **54**(6), p 689–706. https://doi.org/10.1016/j.pmatsci.2009.03.008

192. R.E. Laureijs et al., Metal Additive Manufacturing: Cost Competitive Beyond Low Volumes, *J. Manuf. Sci. Eng.*, 2017 https://doi.org/10.1115/1.4035420

193. R.J. Hebert, Viewpoint: Metallurgical Aspects of Powder Bed Metal Additive Manufacturing, *J. Mater. Sci.*, 2015, **51**(3), p 1165–1175. https://doi.org/10.1007/s10853-015-9479-x

194. M. Qiang Chu, et al., Research on Post-Processing Microstructure and Property of Titanium Components with Selective Laser Melting (SLM). in *IOP Conference Series: Materials Science and Engineering*, (2020) https://doi.org/10.1088/1757-899x/751/1/012079

195. J. Pegues et al., Surface Roughness Effects on the Fatigue Strength of Additively Manufactured Ti-6Al-4V, *Int. J. Fatigue*, 2018, **116**, p 543–552. https://doi.org/10.1016/j.ijfatigue.2018.07.013

196. C. de Formanoir et al., Micromechanical Behavior and Thermal Stability of A Dual-Phase α+α' Titanium Alloy Produced by Additive Manufacturing, *Acta Mater.*, 2019, **162**, p 149–162. https://doi.org/10.1016/j.actamat.2018.09.050

197. S. Leuders et al., On the Mechanical Behaviour of Titanium Alloy TiAl6V4 Manufactured by Selective Laser Melting: Fatigue Resistance and Crack Growth Performance, *Int. J. Fatigue*, 2013, **48**, p 300–307. https://doi.org/10.1016/j.ijfatigue.2012.11.011

198. L. Draelos, P. Nandwana, and A. Srivastava, Implications of Post-Processing Induced Microstructural Changes on the Deformation and Fracture Response of Additively Manufactured Ti-6Al-4V, *Mater. Sci. Eng. A*, 2020 https://doi.org/10.1016/j.msea.2020.139986

199. M.D. Sangid et al., Role of Heat Treatment and Build Orientation in the Microstructure Sensitive Deformation Characteristics of IN718 Produced Via SLM Additive Manufacturing, *Addit. Manuf.*, 2018, **22**, p 479–496. https://doi.org/10.1016/j.addma.2018.04.032

200. M.M. Kirka et al., Strategy for Texture Management in Metals Additive Manufacturing, *JOM*, 2017, **69**(3), p 523–531. https://doi.org/10.1007/s11837-017-2264-3

201. I. Lopez-Galilea et al., Additive Manufacturing of CMSX-4 Ni-Base Superalloy by Selective Laser Melting: Influence of Processing Parameters and Heat Treatment, *Addit. Manuf.*, 2019 https://doi.org/10.1016/j.addma.2019.100874

202. P.D. Enrique et al., Enhancing Fatigue Life of Additive Manufactured Parts with Electrospark Deposition Post-Processing, *Addit. Manuf.*, 2020 https://doi.org/10.1016/j.addma.2020.101526

203. V.V. Popov et al., Selective Electron Beam Melting of Al0.5Cr-MoNbTa0.5 High Entropy Alloys Using Elemental Powder Blend, *Heliyon*, 2019, **5**(2), p e01188. https://doi.org/10.1016/j.heliyon.2019.e01188

204. Y. Lu et al., Microstructure, Mechanical Property and Metal Release of As-SLM CoCrW Alloy Under Different Solution Treatment Conditions, *J. Mech. Behav. Biomed. Mater.*, 2015, **55**, p 179–190. https://doi.org/10.1016/j.jmbbm.2015.10.019

205. E. Santecchia et al., Precipitates Formation and Evolution in A Co-Based Alloy Produced by Powder Bed Fusion, *J. Alloys Compd.*, 2019, **797**, p 652–658. https://doi.org/10.1016/j.jallcom.2019.05.169

206. C. Zhou et al., Improvement of Corrosion Resistance of SS316L Manufactured by Selective Laser Melting Through Subcritical Annealing, *Corros. Sci.*, 2020 https://doi.org/10.1016/j.corsci.2019.108353

207. M. Laleh et al., Unanticipated Drastic Decline in Pitting Corrosion Resistance of Additively Manufactured 316L Stainless Steel After High-Temperature Post-Processing, *Corros. Sci.*, 2020 https://doi.org/10.1016/j.corsci.2019.108412

208. J.H. Martin et al., Additive Manufacturing of Metal Matrix Composites Via Nanofunctionalization, *MRS Commun.*, 2018, **8**(02), p 297–302. https://doi.org/10.1557/mrc.2018.95

209. A.H. Maamoun et al., Thermal Post-Processing of AlSi10Mg Parts Produced by Selective Laser Melting Using Recycled Powder, *Addit.*

Manuf., 2018, **21**, p 234–247. https://doi.org/10.1016/j.addma.2018.03.014

210. C. Shen et al., Neutron Diffraction Residual Stress Determinations in Fe3Al Based Iron Aluminide Components Fabricated Using Wire-Arc Additive Manufacturing (WAAM), *Addit. Manuf.*, 2019 https://doi.org/10.1016/j.addma.2019.06.025

211. C. Meier et al., Thermophysical Phenomena in Metal Additive Manufacturing by Selective Laser Melting: Fundamentals, Modeling, Simulation, and Experimentation, *Ann. Rev. Heat Transfer*, 2017, **20**(1), p 241–316. https://doi.org/10.1615/AnnualRevHeatTransfer.2018019042

212. M. Benedetti et al., Low- and High-Cycle Fatigue Resistance of Ti-6Al-4V ELI Additively Manufactured Via Selective Laser Melting: Mean Stress and Defect Sensitivity, *Int. J. Fatigue*, 2018, **107**, p 96–109. https://doi.org/10.1016/j.ijfatigue.2017.10.021

213. W. Xu et al., In Situ Tailoring Microstructure in Additively Manufactured Ti-6Al-4V for Superior Mechanical Performance, *Acta Mater.*, 2017, **125**, p 390–400. https://doi.org/10.1016/j.actamat.2016.12.027

214. M.M. Attallah et al., Additive Manufacturing of Ni-Based Superalloys: The Outstanding Issues, *MRS Bull.*, 2016, **41**(10), p 758–764. https://doi.org/10.1557/mrs.2016.211

215. J.H. Boswell et al., Cracking During Thermal Post-Processing of Laser Powder Bed Fabricated CM247LC Ni-Superalloy, *Mater. Des.*, 2019 https://doi.org/10.1016/j.matdes.2019.107793

216. S. Kumar, Process Chain Development for Additive Manufacturing of Cemented Carbide, *J. Manuf. Process.*, 2018, **34**, p 121–130. https://doi.org/10.1016/j.jmapro.2018.05.036

217. S. Gorsse et al., Additive Manufacturing of Metals: A Brief Review of the Characteristic Microstructures and Properties of Steels, Ti-6Al-4V and High-Entropy Alloys, *Sci. Technol. Adv. Mater.*, 2017, **18**(1), p 584–610. https://doi.org/10.1080/14686996.2017.1361305

218. C.-H. Kuo et al., Ultrasonic Additive Manufacturing of 4130 Steel Using Ni Interlayers, *Sci. Technol. Weld. Joining*, 2019, **24**(5), p 382–390. https://doi.org/10.1080/13621718.2019.1607486

219. Y. Shi et al., Microstructure and Tensile Properties of Laser Engineered Net Shaped Reduced Activation Ferritic/Martensitic Steel, *Mater. Charact.*, 2018, **144**, p 554–562. https://doi.org/10.1016/j.matchar.2018.08.010

220. M.J. Juhasz, *In and Ex-Situ Process Development in Laser-Based Additive Manufacturing*, Youngstown State University, Youngstown, 2020

221. P. Ginestra et al., Post Processing of 3D Printed Metal Scaffolds: A Preliminary Study of Antimicrobial Efficiency, *Procedia Manuf.*, 2020, **47**, p 1106–1112. https://doi.org/10.1016/j.promfg.2020.04.126

222. G. Strano et al., Surface Roughness Analysis, Modelling and Prediction in Selective Laser Melting, *J. Mater. Process. Technol.*, 2013, **213**(4), p 589–597. https://doi.org/10.1016/j.jmatprotec.2012.11.011

223. S. Rahmati and E. Vahabli, Evaluation of Analytical Modeling for Improvement of Surface Roughness of FDM Test Part Using Measurement Results, *Int. J. Adv. Manuf. Technol.*, 2015, **79**(5), p 823–829. https://doi.org/10.1007/s00170-015-6879-7

224. J. Solis Romero, A. Anguiano García, and A. García Macedo, Surface Roughness and Residual Stresses on the Fatigue Life of Shot Peened Components: Theoretical Determination, *Ingeniería Mecánica, Tecnología Y Desarrollo.*, 2008, **3**(1), p 17–20

225. C. Vallellano, A. Navarro, and J. Dominguez, Fatigue Crack Growth Threshold Conditions at Notches. Part I: Theory, *Fatigue Fract. Eng. Mater. Struct. (Print)*, 2000, **23**(2), p 113–121. https://doi.org/10.1046/j.1460-2695.2000.00257.x

226. R.A. Smith and K.J. Miller, Prediction of Fatigue Regimes in Notched Components, *Int. J. Mech. Sci.*, 1978, **20**(4), p 201–206. https://doi.org/10.1016/0020-7403(78)90082-6

227. N. Sunay, M. Kaya, and Y. Kaynak, Chemical Post-Processing Methods For Enhancing Surface Properties of Parts Fabricated by Additive Manufacturing: A Review, *Sigma J. Eng. Nat. Sci.*, 2020, **38**, p 2027–2042

228. E. Atzeni et al., Surface Finishing of Additive Manufactured Ti-6Al-4V Alloy: A Comparison between Abrasive Fluidized Bed and Laser Finishing, *Materials*, 2021 https://doi.org/10.3390/ma14185366

229. M. Kahlin et al., Improved Fatigue Strength of Additively Manufactured Ti6Al4V by Surface Post Processing, *Int. J. Fatigue*, 2020 https://doi.org/10.1016/j.ijfatigue.2020.105497

230. L. Denti et al., Fatigue Life and Microstructure of Additive Manufactured Ti6Al4V After Different Finishing Processes, *Mater. Sci. Eng. A*, 2019, **755**, p 1–9. https://doi.org/10.1016/j.msea.2019.03.119

231. M.A. Melia et al., How Build Angle and Post-Processing Impact Roughness and Corrosion of Additively Manufactured 316L Stainless Steel, *Npj Mater. Degrad.*, 2020 https://doi.org/10.1038/s41529-020-00126-5

232. K.L. Tan and S.H. Yeo, Surface Finishing on IN625 Additively Manufactured Surfaces by Combined Ultrasonic Cavitation and Abrasion, *Addit. Manuf.*, 2020, **31**, p 100938. https://doi.org/10.1016/j.addma.2019.100938

233. A.Q. Teo et al., Post-Processing and Surface Characterization of Additively Manufactured Stainless Steel 316L Lattice: Implications for BioMedical Use, *Materials*, 2021 https://doi.org/10.3390/ma14061376

234. B. Sagbas, Post-Processing Effects on Surface Properties of Direct Metal Laser Sintered AlSi10Mg Parts, *Metals Mater. Int.*, 2019, **26**(1), p 143–153. https://doi.org/10.1007/s12540-019-00375-3

235. G.A. Longhitano et al., Surface Finishes for Ti-6Al-4V Alloy Produced by Direct Metal Laser Sintering, *Mater. Res.*, 2015, **18**, p 838–842

236. Y. Kaynak and E. Tascioglu, Post-Processing Effects on the Surface Characteristics of Inconel 718 Alloy Fabricated by Selective Laser Melting Additive Manufacturing, *Prog. Addit. Manuf.*, 2019, **5**(2), p 221–234. https://doi.org/10.1007/s40964-019-00099-1

237. D.A. Lesyk et al., Post-Processing of the Inconel 718 Alloy Parts Fabricated by Selective Laser Melting: Effects of Mechanical Surface Treatments on Surface Topography, Porosity, Hardness and Residual Stress, *Surf. Coat. Technol.*, 2020 https://doi.org/10.1016/j.surfcoat.2019.125136

238. H. Soyama and F. Takeo, Effect of Various Peening Methods on the Fatigue Properties of Titanium Alloy Ti6Al4V Manufactured by Direct Metal Laser Sintering and Electron Beam Melting, *Materials*, 2020 https://doi.org/10.3390/ma13102216

239. S. Bagehorn, J. Wehr, and H.J. Maier, Application of Mechanical Surface Finishing Processes for Roughness Reduction and Fatigue Improvement of Additively Manufactured Ti-6Al-4V Parts, *Int. J. Fatigue*, 2017, **102**, p 135–142. https://doi.org/10.1016/j.ijfatigue.2017.05.008

240. N.E. Uzan et al., On the Effect of Shot-Peening on Fatigue Resistance of AlSi10Mg Specimens Fabricated by Additive Manufacturing Using Selective Laser Melting (AM-SLM), *Addit. Manuf.*, 2018, **21**, p 458–464. https://doi.org/10.1016/j.addma.2018.03.030

241. J. Sawicki et al., Influence of Single-Stage and Duplex Shot Peening on Surface Roughness and Residual Stresses in Al Mg5 Mn1 Sc0,8 Zr0,4 Alloy, *Arch. Metall. Mater.*, 2018 https://doi.org/10.24425/118968

242. A.H. Maamoun, M.A. Elbestawi, and S.C. Veldhuis, Influence of Shot Peening on AlSi10Mg Parts Fabricated by Additive Manufacturing, *J. Manuf. Mater. Process.*, 2018 https://doi.org/10.3390/jmmp2030040

243. J. Damon et al., Process Dependent Porosity and the Influence of Shot Peening on Porosity Morphology Regarding Selective Laser Melted AlSi10Mg Parts, *Addit. Manuf.*, 2018, **20**, p 77–89. https://doi.org/10.1016/j.addma.2018.01.001

244. L. Hackel et al., Laser Peening: A tool for Additive Manufacturing Post-Processing, *Addit. Manuf.*, 2018, **24**, p 67–75. https://doi.org/10.1016/j.addma.2018.09.013

245. L. Chen et al., Improvement of High Temperature Oxidation Resistance of Additively Manufactured TiC/Inconel 625 Nanocomposites by Laser Shock Peening Treatment, *Addit. Manuf.*, 2020, **34**, p 101276. https://doi.org/10.1016/j.addma.2020.101276

246. J. Chi et al., Effects of Heat Treatment Combined with Laser Shock Peening on Wire and Arc Additive Manufactured Ti17 Titanium Alloy: Microstructures, Residual Stress and Mechanical Properties, *Surf. Coat. Technol.*, 2020, **396**, p 125908. https://doi.org/10.1016/j.surfcoat.2020.125908

247. X. Jin et al., Effects of Laser Shock Peening on Microstructure and Fatigue Behavior of Ti-6Al-4V Alloy Fabricated Via Electron Beam Melting, *Mater. Sci. Eng. A*, 2020, **780**, p 139199. https://doi.org/10.1016/j.msea.2020.139199

248. N. Kalentics et al., 3D Laser Shock Peening as A Way to Improve Geometrical Accuracy in Selective Laser Melting, *Int. J. Adv. Manuf.*

Technol., 2019, **101**(5), p 1247–1254. https://doi.org/10.1007/s00170-018-3033-3

249. N. Kalentics et al., Laser Shock Peening: A Promising Tool for Tailoring Metallic Microstructures in Selective Laser Melting, *J. Mater. Process. Technol.*, 2019, **266**, p 612–618. https://doi.org/10.1016/j.jmatprotec.2018.11.024

250. L. Lan et al., Microstructural Evolution and Stress State Related to Mechanical Properties of Electron Beam Melted Ti-6Al-4V Alloy Modified by Laser Shock Peening, *J. Mater. Sci. Technol.*, 2020, **50**, p 153–161. https://doi.org/10.1016/j.jmst.2019.11.039

251. A.N. Jinoop et al., Post-Processing of Laser Additive Manufactured Inconel 718 Using Laser Shock Peening, *Int. J. Precis. Eng. Manuf.*, 2019, **20**(9), p 1621–1628. https://doi.org/10.1007/s12541-019-00147-4

252. A. Lamikiz et al., Laser Polishing of Parts Built Up by Selective Laser Sintering, *Int. J. Mach. Tools Manuf*, 2007, **47**(12), p 2040–2050. https://doi.org/10.1016/j.ijmachtools.2007.01.013

253. K.C. Yung et al., Laser Polishing of Additive Manufactured CoCr Alloy Components with Complex Surface Geometry, *J. Mater. Process. Technol.*, 2018, **262**, p 53–64. https://doi.org/10.1016/j.jmatprotec.2018.06.019

254. K. Alrbaey et al., On Optimization of Surface Roughness of Selective Laser Melted Stainless Steel Parts: A Statistical Study, *J. Mater. Eng. Perform.*, 2014, **23**(6), p 2139–2148. https://doi.org/10.1007/s11665-014-0993-9

255. E.V. Bordatchev, A.M.K. Hafiz, and O.R. Tutunea-Fatan, Performance of Laser Polishing in Finishing of Metallic Surfaces, *Int. J. Adv. Manuf. Technol.*, 2014, **73**(1), p 35–52. https://doi.org/10.1007/s00170-014-5761-3

256. E. Ukar et al., Roughness Prediction on Laser Polished Surfaces, *J. Mater. Process. Technol.*, 2012, **212**(6), p 1305–1313. https://doi.org/10.1016/j.jmatprotec.2012.01.007

257. M. Hofele et al., Laser Polishing of Additive Manufactured Aluminium Parts by Modulated Laser Power, *Micromachines*, 2021 https://doi.org/10.3390/mi12111332

258. M. Hofele et al., Laser Polishing of Laser Powder Bed Fusion AlSi10Mg Parts—Influence of Initial Surface Roughness on Achievable Surface Quality, *Mater. Sci. Appl.*, 2021, **12**(1), p 15–41. https://doi.org/10.4236/msa.2021.121002

259. M.A. Obeidi et al., Laser Polishing of Additive Manufactured 316L Stainless Steel Synthesized by Selective Laser Melting, *Materials*, 2019 https://doi.org/10.3390/ma12060991

260. F. Scherillo et al., Chemical Surface Finishing of Electron Beam Melted Ti6Al4V Using HF-HNO3 Solutions, *J. Manuf. Process.*, 2020, **60**, p 400–409. https://doi.org/10.1016/j.jmapro.2020.10.033

261. B. Wysocki et al., The Influence of Chemical Polishing of Titanium Scaffolds on Their Mechanical Strength and In-Vitro Cell Response, *Mater. Sci. Eng. C*, 2019, **95**, p 428–439. https://doi.org/10.1016/j.msec.2018.04.019

262. P. Tyagi et al., Reducing the Roughness of Internal Surface of An Additive Manufacturing Produced 316 Steel Component by Chempolishing and Electropolishing, *Addit. Manuf.*, 2019, **25**, p 32–38. https://doi.org/10.1016/j.addma.2018.11.001

263. C. de Formanoir et al., Improving the Mechanical Efficiency of Electron Beam Melted Titanium Lattice Structures by Chemical Etching, *Addit. Manuf.*, 2016, **11**, p 71–76. https://doi.org/10.1016/j.addma.2016.05.001

264. G. Dong, J. Marleau-Finley, and Y.F. Zhao, Investigation of Electrochemical Post-Processing Procedure for Ti-6Al-4V Lattice Structure Manufactured by Direct Metal Laser Sintering (DMLS), *Int. J. Adv. Manuf. Technol.*, 2019, **104**(9), p 3401–3417. https://doi.org/10.1007/s00170-019-03996-5

265. B.V. Hooreweder et al., CoCr F75 scaffolds Produced by Additive Manufacturing: Influence of Chemical Etching on Powder Removal and Mechanical Performance, *J. Mech. Behav. Biomed. Mater.*, 2017, **70**, p 60–67. https://doi.org/10.1016/j.jmbbm.2017.03.017

266. G. Pyka et al., Surface Modification of Ti6Al4V Open Porous Structures Produced by Additive Manufacturing, *Adv. Eng. Mater.*, 2012, **14**(6), p 363–370. https://doi.org/10.1002/adem.201100344

267. W. Han and F. Fang, Fundamental Aspects and Recent Developments in Electropolishing, *Int. J. Mach. Tools Manuf.*, 2019, **139**, p 1–23. https://doi.org/10.1016/j.ijmachtools.2019.01.001

268. U.S. Kim and J.W. Park, High-Quality Surface Finishing of Industrial Three-Dimensional Metal Additive Manufacturing Using Electro-chemical Polishing, *Int. J. Precis. Eng. Manuf. Green Technol.*, 2019, **6**(1), p 11–21. https://doi.org/10.1007/s40684-019-00019-2

269. Z. Baicheng et al., Study of Selective Laser Melting (SLM) Inconel 718 part Surface Improvement by Electrochemical Polishing, *Mater. Des.*, 2017, **116**, p 531–537. https://doi.org/10.1016/j.matdes.2016.11.103

270. Y. Zhang et al., Electrochemical Polishing of Additively Manufactured Ti-6Al-4V Alloy, *Metals Mater. Int.*, 2020, **26**(6), p 783–792. https://doi.org/10.1007/s12540-019-00556-0

271. A. Acquesta and T. Monetta, The Electropolishing of Additively Manufactured Parts in Titanium: State of the Art, *Adv. Eng. Mater.*, 2021 https://doi.org/10.1002/adem.202100545

272. S. Chang et al., Highly Effective Smoothening of 3D-Printed Metal Structures Via Overpotential Electrochemical Polishing, *Mater. Res. Lett.*, 2019, **7**(7), p 282–289. https://doi.org/10.1080/21663831.2019.1601645

273. P. Tyagi et al., Roughness Reduction of Additively Manufactured Steel by Electropolishing, *Int. J. Adv. Manuf. Technol.*, 2020, **106**(3), p 1337–1344. https://doi.org/10.1007/s00170-019-04720-z

274. C. Rotty et al., Electropolishing Behavior of Additive Layer Manufacturing 316L Stainless Steel in Deep Eutectic Solvents, *ECS Trans.*, 2017, **77**(11), p 1199–1207. https://doi.org/10.1149/07711.1199ecst

275. V. Urlea and V. Brailovski, Electropolishing and Electropolishing-Related Allowances for IN625 Alloy Components Fabricated by Laser Powder-Bed Fusion, *Int. J. Adv. Manuf. Technol.*, 2017, **92**(9), p 4487–4499. https://doi.org/10.1007/s00170-017-0546-0

276. V. Urlea and V. Brailovski, Electropolishing and Electropolishing-Related Allowances for Powder Bed Selectively Laser-Melted Ti-6Al-4V Alloy components, *J. Mater. Process. Technol.*, 2017, **242**, p 1–11. https://doi.org/10.1016/j.jmatprotec.2016.11.014

277. A.G. Demir and B. Previtali, Additive Manufacturing of Cardiovascular CoCr Stents by Selective Laser Melting, *Mater. Des.*, 2017, **119**, p 338–350. https://doi.org/10.1016/j.matdes.2017.01.091

278. V. Finazzi et al., Design and Functional Testing of a Novel Balloon-Expandable Cardiovascular Stent in CoCr Alloy Produced by Selective Laser Melting, *J. Manuf. Process.*, 2020, **55**, p 161–173. https://doi.org/10.1016/j.jmapro.2020.03.060

279. P.D. Enrique et al., Surface Modification of Binder-Jet Additive Manufactured Inconel 625 Via Electrospark Deposition, *Surf. Coat. Technol.*, 2019, **362**, p 141–149. https://doi.org/10.1016/j.surfcoat.2019.01.108

280. W. Tillmann et al., Tribo-Mechanical Properties and Adhesion Behavior of DLC Coatings Sputtered Onto 36NiCrMo16 Produced by Selective Laser Melting, *Surf. Coat. Technol.*, 2020, **394**, p 125748. https://doi.org/10.1016/j.surfcoat.2020.125748

281. W. Tillmann et al., Coatability of Diamond-Like Carbon on 316L Stainless Steel Printed by Binder Jetting, *Addit. Manuf.*, 2021, **44**, p 102064. https://doi.org/10.1016/j.addma.2021.102064

282. J.R. Hönnige et al., Residual Stress and Texture Control in Ti-6Al-4V Wire + Arc Additively Manufactured Intersections by Stress Relief and Rolling, *Mater. Des.*, 2018, **150**, p 193–205. https://doi.org/10.1016/j.matdes.2018.03.065

283. M.-S. Kim et al., Ultrasonic Nanocrystal Surface Modification of High-Speed Tool Steel (AISI M4) Layered Via Direct Energy Deposition, *J. Mater. Process. Technol.*, 2020, **277**, p 116420. https://doi.org/10.1016/j.jmatprotec.2019.116420

284. C. Ma, Y. Dong, and C. Ye, Improving Surface Finish of 3D-printed Metals by Ultrasonic Nanocrystal Surface Modification, *Procedia CIRP*, 2016, **45**, p 319–322. https://doi.org/10.1016/j.procir.2016.02.339

285. C. Ma et al., Improving Surface Finish and Wear Resistance of Additive Manufactured Nickel-Titanium by ultRasonic Nano-Crystal Surface Modification, *J. Mater. Process. Technol.*, 2017, **249**, p 433–440. https://doi.org/10.1016/j.jmatprotec.2017.06.038

286. A. Amanov et al., Micro-Dimpled Surface by Ultrasonic Nanocrystal Surface Modification and Its Tribological Effects, *Wear*, 2012, **286–287**, p 136–144. https://doi.org/10.1016/j.wear.2011.06.001

287. A.H. Maamoun, S.C. Veldhuis, and M. Elbestawi, Friction Stir Processing of AlSi10Mg Parts Produced by Selective Laser Melting, *J. Mater. Process. Technol.*, 2019, **263**, p 308–320. https://doi.org/10.1016/j.jmatprotec.2018.08.030

288. C. Huang et al., Ductilization of Selective Laser Melted Ti6Al4V Alloy by Friction Stir Processing, *Mater. Sci. Eng. A*, 2019, **755**, p 85–96. https://doi.org/10.1016/j.msea.2019.03.133

289. W. Li et al., A Comparative Study on the Employment of Heat Treatment, Electric Pulse Processing and Friction Stir Processing to Enhance Mechanical Properties of Cold-Spray-Additive-Manufactured Copper, *Surf. Coat. Technol.*, 2021, **409**, p 126887. https://doi.org/10.1016/j.surfcoat.2021.126887

290. J.G. Santos Macías et al., Ductilisation and Fatigue Life Enhancement of Selective Laser Melted AlSi10Mg by Friction Stir Processing, *Scripta Mater.*, 2019, **170**, p 124–128. https://doi.org/10.1016/j.scriptamat.2019.05.044

291. X. Xie et al., Achieving Simultaneously Improved Tensile Strength and Ductility of A Nano-TiB2/AlSi10Mg Composite Produced by Cold Spray Additive Manufacturing, *Compos. Part B Eng.*, 2020, **202**, p 108404. https://doi.org/10.1016/j.compositesb.2020.108404

292. L. Zhao et al., Comparison of Residual Stresses Obtained by the Crack Compliance Method for Parts Produced by Different Metal Additive Manufacturing Techniques and After Friction Stir Processing, *Addit. Manuf.*, 2020, **36**, p 101499. https://doi.org/10.1016/j.addma.2020.101499

293. A. Zykova et al., Evolution of Microstructure and Properties of Fe-Cu, Manufactured by Electron Beam Additive Manufacturing with Subsequent Friction Stir Processing, *Mater. Lett.*, 2022, **307**, p 131023. https://doi.org/10.1016/j.matlet.2021.131023

294. Y. Lu et al., The Effects of Laser Peening on Laser Additive Manufactured 316L Steel, *Int. J. Adv. Manuf. Technol.*, 2020, **107**(5), p 2239–2249. https://doi.org/10.1007/s00170-020-05167-3

295. M. McGaffey et al., Manual Polishing of 3D Printed Metals Produced by Laser Powder Bed Fusion Reduces Biofilm Formation, *PLoS ONE*, 2019, **14**(2), p e0212995. https://doi.org/10.1371/journal.pone.0212995

296. R. Molaei, A. Fatemi, and N. Phan, Notched Fatigue of Additive Manufactured Metals Under Axial and Multiaxial Loadings, Part I: Effects of Surface Roughness and HIP and Comparisons with Their Wrought Alloys, *Int. J. Fatigue*, 2021 https://doi.org/10.1016/j.ijfatigue.2020.106003

297. Z. Qiu et al., Cryogenic Deformation Mechanism of CrMnFeCoNi High-Entropy Alloy Fabricated by Laser Additive Manufacturing Process, *Int. J. Lightweight Mater. Manuf.*, 2018, **1**(1), p 33–39. https://doi.org/10.1016/j.ijlmm.2018.02.001

298. X. Yang et al., Additively Manufactured Fine Grained Ni6Cr4WFe9Ti High Entropy Alloys with High Strength and Ductility, *Mater. Sci. Eng. A*, 2019 https://doi.org/10.1016/j.msea.2019.138394

299. A.S. Iquebal, S. Shrestha, Z. Wang, G.P. Manogharan, S. Bukkapatnam and O. Youngstown, Influence of Milling and Non-Traditional Machining on Surface Properties of Ti6Al4V EBM Components. in *Proceedings of the 2016 Industrial and Systems Engineering Research Conference*, 2016

300. E. Tascioglu et al., The Effect of Finish-Milling Operation on Surface Quality and Wear Resistance of Inconel 625 Produced by Selective Laser Melting Additive Manufacturing, in *Advanced Surface Enhancement*. p. 263–272. (2020)

301. A. Vinoth Jebaraj and M. Sugavaneswaran, Influence of Shot Peening on Residual Stress Distribution and Corrosion Resistance of Additive Manufactured Stainless Steel AISI 316L, *Trans. Indian Inst. Metals*, 2019, **72**, p 1651–1653. https://doi.org/10.1007/s12666-019-01601-7

302. M. Qian et al., Additive Manufacturing and Postprocessing of Ti-6Al-4V for Superior Mechanical Properties, *MRS Bull.*, 2016, **41**(10), p 775–784. https://doi.org/10.1557/mrs.2016.215

303. Q. Portella, M. Chemkhi, and D. Retraint, Influence of Surface Mechanical Attrition Treatment (SMAT) Post-Treatment on Microstructural, Mechanical and Tensile Behaviour of Additive Manufactured AISI 316L, *Mater. Charact.*, 2020, **167**, p 110463. https://doi.org/10.1016/j.matchar.2020.110463

304. B. AlMangour and J.-M. Yang, Improving the Surface Quality and Mechanical Properties by Shot-Peening of 17-4 Stainless Steel Fabricated by Additive Manufacturing, *Mater. Des.*, 2016, **110**, p 914–924. https://doi.org/10.1016/j.matdes.2016.08.037

305. D. Karthik and S. Swaroop, Laser Peening Without Coating—an Advanced Surface Treatment: A Review, *Mater. Manuf. Process.*, 2017, **32**(14), p 1565–1572. https://doi.org/10.1080/10426914.2016.1221095

306. C. Zhang, Y. Dong, and C. Ye, Recent Developments and Novel Applications of Laser Shock Peening: A Review, *Adv. Eng. Mater.*, 2021, **23**(7), p 2001216. https://doi.org/10.1002/adem.202001216

307. R. Fabbro et al., Physical Study of Laser-Produced Plasma in Confined Geometry, *J. Appl. Phys.*, 1990, **68**(2), p 775–784. https://doi.org/10.1063/1.346783

308. U.S. Dixit, S.N. Joshi, and J.P. Davim, *Application of Lasers in Manufacturing: Select Papers from AIMTDR 2016*, Springer, Singapore, 2018

309. N. Kalentics et al., 3D Laser Shock Peening – A New Method for the 3D Control of Residual Stresses in Selective Laser Melting, *Mater. Des.*, 2017, **130**, p 350–356. https://doi.org/10.1016/j.matdes.2017.05.083

310. E. Toyserkani, A. Khajepour, and S. Corbin, 3-D Finite Element Modeling of Laser Cladding by Powder Injection: Effects of Laser Pulse Shaping on the Process, *Opt. Lasers Eng.*, 2004, **41**(6), p 849–867. https://doi.org/10.1016/S0143-8166(03)00063-0

311. L. Wang, *Foundations of Stress Waves*, Elsevier, Heidelberg, 2011

312. B.P. Fairand et al., Laser Shock-Induced Microstructural and Mechanical Property Changes in 7075 Aluminum, *J. Appl. Phys.*, 1972, **43**(9), p 3893–3895. https://doi.org/10.1063/1.1661837

313. R.K. Nalla et al., On the Influence of Mechanical Surface Treatments—Deep Rolling and Laser Shock Peening—on the Fatigue Behavior of Ti-6Al-4V at Ambient and Elevated Temperatures, *Mater. Sci. Eng. A*, 2003, **355**(1), p 216–230. https://doi.org/10.1016/S0921-5093(03)00069-8

314. L.E. Rännar et al., Water Jet Polishing of Materials Manufactured with Electron Beam Melting Technology, in *World Powder Metallurgy Congress, Hamburg, Germany, 9–13 October, 2016*, European Powder Metallurgy Association (2016)

315. Hashish, M., The potential of UHP and waterjets for additive manufacturing, in *3rd International Conference on Progress in Additive Manufacturing*. p. 690–695. (2018)

316. M. Salmi, J. Huuki, and I.F. Ituarte, The Ultrasonic Burnishing of Cobalt-Chrome and Stainless Steel Surface Made by Additive Manufacturing, *Prog. Addit. Manuf.*, 2017, **2**(1–2), p 31–41. https://doi.org/10.1007/s40964-017-0017-z

317. H. Zhang et al., The Effects of Electrically-Assisted Ultrasonic Nanocrystal Surface Modification on 3D-Printed Ti-6Al-4V Alloy, *Addit. Manuf.*, 2018, **22**, p 60–68. https://doi.org/10.1016/j.addma.2018.04.035

318. H. Zhang et al., The Effects of Ultrasonic Nanocrystal Surface Modification on the Fatigue Performance of 3D-Printed Ti64, *Int. J. Fatigue*, 2017, **103**, p 136–146. https://doi.org/10.1016/j.ijfatigue.2017.05.019

319. V. Alfieri et al., Reduction of Surface Roughness by Means of Laser Processing over Additive Manufacturing Metal Parts, *Materials (Basel)*, 2016 https://doi.org/10.3390/ma10010030

320. A. Temmler et al., Influence of Laser Polishing on Surface Roughness and Microstructural Properties of the Remelted Surface Boundary Layer of Tool Steel H11, *Mater. Des.*, 2020, **192**, p 108689. https://doi.org/10.1016/j.matdes.2020.108689

321. T.L. Perry et al., The Effect of Laser Pulse Duration and Feed Rate on Pulsed Laser Polishing of Microfabricated Nickel Samples, *J. Manuf. Sci. Eng.*, 2009 https://doi.org/10.1115/1.3106033

322. Y. Tian et al., Material Interactions in Laser Polishing Powder Bed Additive Manufactured Ti6Al4V Components, *Addit. Manuf.*, 2018, **20**, p 11–22. https://doi.org/10.1016/j.addma.2017.12.010

323. F. Zhihao et al., Laser Polishing of Additive Manufactured Superalloy, *Procedia CIRP*, 2018, **71**, p 150–154. https://doi.org/10.1016/j.procir.2018.05.088

324. H. Xiao, Y. Zhou, M. Liu, and X. Xu, Laser Polishing of Tool Steel Using A Continuous-Wave Laser Assisted by a Steady Magnetic Field, *AIP Adv.*, 2020, **10**(2), p 025319. https://doi.org/10.1063/1.5116686

325. I. Mingareev, T. Bonhoff, A.F. El-Sherif, W. Meiners, I. Kelbassa, T. Biermann, and M. Richardson, Femtosecond Laser Post-Processing of Metal Parts Produced by Laser Additive Manufacturing, *J. Laser Appl.*, 2013, **25**(5), p 052009. https://doi.org/10.2351/1.4824146

326. N. Worts, J. Jones, and J. Squier, Surface Structure Modification of Additively Manufactured Titanium Components Via Femtosecond Laser Micromachining, *Opt. Commun.*, 2019, **430**, p 352–357. https://doi.org/10.1016/j.optcom.2018.08.055

327. C.-W. Lin et al., Femtosecond Laser Surface Roughening and Pulsed Plasma Polymerization Duplex Treatment on Medical-Grade Stainless Steel Substrates for Orthodontic Purpose, *Surf. Coat. Technol.*, 2021, **427**, p 127819. https://doi.org/10.1016/j.surfcoat.2021.127819

328. M. Bezuidenhout et al., The Effect of HF-HNO3 Chemical Polishing on the Surface Roughness and Fatigue Life of Laser Powder Bed Fusion Produced Ti6Al4V, *Mater. Today Commun.*, 2020 https://doi.org/10.1016/j.mtcomm.2020.101396

329. P. Tyagi et al., Reducing Surface Roughness by Chemical Polishing of Additively Manufactured 3D Printed 316 Stainless Steel Components, *Int. J. Adv. Manuf. Technol.*, 2019, **100**(9), p 2895–2900. https://doi.org/10.1007/s00170-018-2890-0

330. E. Pehlivan et al., Post-Processing Treatment Impact on Mechanical Properties of SLM Deposited Ti-6Al-4 V Porous Structure for Biomedical Application, *Materials (Basel)*, 2020 https://doi.org/10.3390/ma13225167

331. J. Kaspar et al., Integrated Additive Product Development for Multi-Material Parts, *Procedia Manuf.*, 2019, **33**, p 3–10. https://doi.org/10.1016/j.promfg.2019.04.002

332. U. Ali et al., Internal Surface Roughness Enhancement of Parts Made by Laser Powder-Bed Fusion Additive Manufacturing, *Vacuum*, 2020, **177**, p 109314. https://doi.org/10.1016/j.vacuum.2020.109314

333. K. Tajima et al., Electropolishing of CP Titanium and Its Alloys in an Alcoholic Solution-based Electrolyte, *Dent. Mater. J.*, 2008, **27**(2), p 258–265. https://doi.org/10.4012/dmj.27.258

334. J. Guo et al., On the Machining of Selective Laser Melting CoCrFeMnNi High-Entropy Alloy, *Mater. Des.*, 2018, **153**, p 211–220. https://doi.org/10.1016/j.matdes.2018.05.012

335. Y. Hu and W. Cong, A review on Laser Deposition-Additive Manufacturing of Ceramics and Ceramic Reinforced Metal Matrix Composites, *Ceram. Int.*, 2018, **44**(17), p 20599–20612. https://doi.org/10.1016/j.ceramint.2018.08.083

336. K. Salonitis et al., Additive Manufacturing and Post-Processing Simulation: Laser Cladding Followed by High Speed Machining, *Int. J. Adv. Manuf. Technol.*, 2015, **85**(9–12), p 2401–2411. https://doi.org/10.1007/s00170-015-7989-y

337. C. Deng et al., Mechanical and Chemical Properties of CoCrFeNi-Mo0.2 High Entropy Alloy Coating Fabricated on Ti6Al4V by Laser Cladding, *Intermetallics*, 2022, **144**, p 107504. https://doi.org/10.1016/j.intermet.2022.107504

338. I.N. Maliutina et al., Structure and Oxidation Behavior of γ-TiAl Coating Produced by Laser Cladding on Titanium Alloy, *Surf. Coat. Technol.*, 2017, **319**, p 136–144. https://doi.org/10.1016/j.surfcoat.2017.04.008

339. G. Bidron et al., Reduction of the Hot Cracking Sensitivity of CM-247LC Superalloy Processed by Laser Cladding Using Induction Preheating, *J. Mater. Process. Technol.*, 2020, **277**, p 116461. https://doi.org/10.1016/j.jmatprotec.2019.116461

340. A.J.M. Mackus, A.A. Bol, and W.M.M. Kessels, The Use of Atomic Layer Deposition in Advanced Nanopatterning, *Nanoscale*, 2014, **6**(19), p 10941–10960. https://doi.org/10.1039/C4NR01954G

341. A. Moll et al., Coupling Powder Bed Additive Manufacturing and Vapor Phase Deposition Methods for Elaboration of Coated 3D Ti-6Al-4V Architectures with Enhanced Surface Properties, *Surf. Coat. Technol.*, 2021, **415**, p 127130. https://doi.org/10.1016/j.surfcoat.2021.127130

342. V. Urbanová, J. Plutnar, and M. Pumera, Atomic Layer Deposition of Electrocatalytic Layer of MoS2 Onto Metal-Based 3D-Printed Electrode Toward Tailoring Hydrogen Evolution Efficiency, *Appl. Mater. Today*, 2021, **24**, p 101131. https://doi.org/10.1016/j.apmt.2021.101131

343. A. Gisario et al., Metal Additive Manufacturing in the Commercial Aviation Industry: A Review, *J. Manuf. Syst.*, 2019, **53**, p 124–149. https://doi.org/10.1016/j.jmsy.2019.08.005

344. P.J. Noell et al., Microstructural Modification of Additively Manufactured Metals by Electropulsing, *Addit. Manuf.*, 2020 https://doi.org/10.1016/j.addma.2020.101128

345. L. Shi et al., Effect of Electropulsing Treatment on Microstructure and Mechanical Properties of Cu–20Ni–20Mn Alloy, *Mater. Sci. Eng. A*, 2022, **855**, p 143847. https://doi.org/10.1016/j.msea.2022.143847

346. Y. Nakata, T. Abe, and J.I. Kaneko, Suppression of Anisotropy by Wire and Arc Additive Manufacturing with Finishing Process, *J. Adv. Mech. Des. Syst. Manuf.*, 2021 https://doi.org/10.1299/jamdsm2021jamdsm0066

347. W.F. Mitchell et al. Dimensional Accuracy of Titanium Direct Metal Laser Sintered Parts. in *27th Annual International Solid Freeform Fabrication Symposium - An Additive Manufacturing Conference, SFF 2016.* (2016)

348. J. Gordon et al., Enhancement in Fatigue Performance of Metastable Austenitic Stainless Steel Through Directed Energy Deposition Additive Manufacturing, *Mater. Des.*, 2019 https://doi.org/10.1016/j.matdes.2019.107630

349. S.L. Sing et al., Laser and Electron-Beam Powder-Bed Additive Manufacturing of Metallic Implants: A Review on Processes, *Mater. Des. J Orthop Res*, 2016, **34**(3), p 369–385. https://doi.org/10.1002/jor.23075

350. S. Nelaturi et al., Automatic Support Removal for Additive Manufacturing Post Processing, *Comput. Aided Des.*, 2019, **115**, p 135–146. https://doi.org/10.1016/j.cad.2019.05.030

351. M.-H. Hong, B. Min, and T.-Y. Kwon, The Influence of Process Parameters on the Surface Roughness of a 3D-Printed Co–Cr Dental Alloy Produced via Selective Laser Melting, *Appl. Sci.*, 2016 https://doi.org/10.3390/app6120401

352. Q. Han et al., Additive Manufacturing of High-Strength Crack-Free Ni-Based Hastelloy X Superalloy, *Addit. Manuf.*, 2019 https://doi.org/10.1016/j.addma.2019.100919

353. D. Meyer and N. Wielki, Internal Reinforced Domains by Intermediate Deep Rolling in Additive Manufacturing, *CIRP Ann.*, 2019, **68**(1), p 579–582. https://doi.org/10.1016/j.cirp.2019.04.012

354. M.C. Frank et al. Direct Additive Subtractive Hybrid Manufacturing (DASH)—an Out of Envelope Method. in *28th Annual International Solid Freeform Fabrication Symposium.* (2017)

355. T.A. Book and M.D. Sangid, Evaluation of Select Surface Processing Techniques for In Situ Application During the Additive Manufacturing Build Process, *JOM*, 2016, **68**(7), p 1780–1792. https://doi.org/10.1007/s11837-016-1897-y

356. W.J. Sames et al., Feasibility of in Situ Controlled Heat Treatment (ISHT) of Inconel 718 During Electron Beam Melting Additive Manufacturing, *Addit. Manuf.*, 2017, **13**, p 156–165. https://doi.org/10.1016/j.addma.2016.09.001

357. S. Chowdhury, K. Mhpsekar and S. Anand, Part Build Orientation Optimization and Neural Network-Based Geometry Compensation for Additive Manufacturing Process, *J. Manuf. Sci. Eng.*, 2018 https://doi.org/10.1115/1.4038293

358. K. Cooper et al., Contact-Free Support Structures for Part Overhangs in Powder-Bed Metal Additive Manufacturing, *Inventions*, 2017 https://doi.org/10.3390/inventions3010002

359. E. Hori et al., Development of SLM Process Using 200 W Blue Diode Laser for Pure Copper Additive Manufacturing of High Density Structure, *J. Laser Appl.*, 2020, **33**(1), p 012008. https://doi.org/10.2351/7.0000311

360. J.K. Yoder, R.J. Griffiths, and H.Z. Yu, Deformation-Based Additive Manufacturing of 7075 Aluminum with Wrought-Like Mechanical Properties, *Mater. Des.*, 2021, **198**, p 109288. https://doi.org/10.1016/j.matdes.2020.109288

361. Z. Sun et al., Thermodynamics-Guided Alloy and Process Design for Additive Manufacturing, *Nat. Commun.*, 2022, **13**(1), p 4361. https://doi.org/10.1038/s41467-022-31969-y

362. J. Ren et al., Strong Yet Ductile Nanolamellar High-Entropy Alloys by Additive Manufacturing, *Nature*, 2022, **608**(7921), p 62–68. https://doi.org/10.1038/s41586-022-04914-8

363. S. Dryepondt et al., High Temperature High Strength Austenitic Steel Fabricated by Laser Powder-Bed Fusion, *Acta Mater.*, 2022, **231**, p 117876. https://doi.org/10.1016/j.actamat.2022.117876

364. J. Zhang et al., Designing Against Phase and Property Heterogeneities in Additively Manufactured Titanium Alloys, *Nat. Commun.*, 2022, **13**(1), p 4660. https://doi.org/10.1038/s41467-022-32446-2